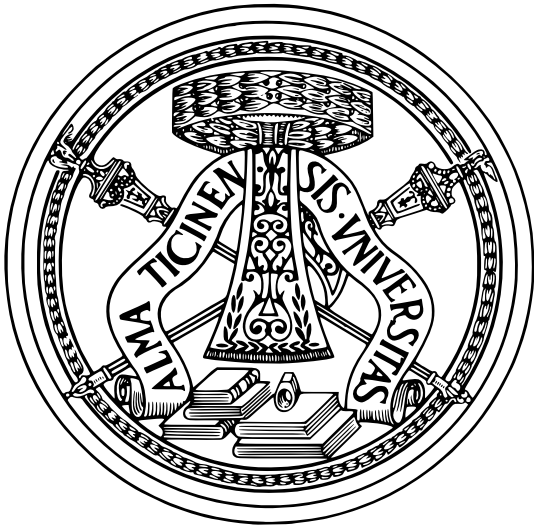


**UNIVERSITÀ DEGLI STUDI DI PAVIA**

FACOLTÀ DI SCIENZE MATEMATICHE, FISICHE E NATURALI

CORSO DI LAUREA MAGISTRALE IN SCIENZE FISICHE

# HOMOMETALLIC AND HETEROMETALLIC ANTIFERROMAGNETIC RINGS: MAGNETIC PROPERTIES STUDIED BY NUCLEAR MAGNETIC RESONANCE

Tesi di Laurea di

**Cecilia Maria Casadei**

Relatore:

**Prof. Ferdinando Borsa**

Dipartimento di Fisica A.Volta

Università degli Studi di Pavia

**Anno Accademico 2010/2011**

# Contents

# Introduction

Molecular magnetic materials have become a prominent part of the physics of magnetic materials in recent years thanks to the synergy between chemists and physicists. Among the many types of molecular magnetic materials a special role is played by the single-molecule magnets. These are systems whereby the magnetic ions, usually $3d$ elements, are embedded in a cluster of organic material. The magnetic ions do interact strongly within each molecule but the intermolecular magnetic interactions are vanishingly small due to the shielding effect of the organic shell. Therefore single molecule magnets are ideal systems to investigate magnetism at a nanoscale.

Nuclear Magnetic Resonance (NMR) is a spectroscopic technique particularly suitable to investigate local magnetic properties. The use of NMR to study molecular nanomagnets is extremely appealing since one can investigate a macroscopic sample and yet obtain information about an individual magnetic molecule since an Avogadro's number of nanomagnets is a replica of $N_A$ identical *non-interacting* entities.

A particular subclass of molecular nanomagnets is constituted of highly symmetric rings of $3d$ ions (e. g. $Cr^{3+}$, $Fe^{2+}$, $V^{3+}$...) interacting among themselves via strong antiferromagnetic interactions. The homometallic rings with an even number of magnetic ions have a total $S = 0$ singlet ground state (e. g. $Cr_8$, $Fe_6$, $Fe_{10}$...). By replacing one magnetic ion with a non-magnetic ion or a magnetic ion of different species one obtains an heterometallic ring where the ground state and the local magnetic moments are modified.

The aim of the present thesis is to investigate the local magnetic properties of homometallic $Cr_8$ AFM ring and the changes occurring by replacing one $Cr^{3+}$ ion with diamagnetic $Cd^{2+}$ ($Cr_7Cd$) and with $Ni^{2+}$ ($Cr_7Ni$). In the heterometallic ring a redistribution of the local magnetic moment is expected in the low temperature ground state.

We have investigated those changes by both $^{53}$Cr-NMR and $^{19}$F-NMR. Most of the experiments have been performed at Ames Laboratory (Iowa State University, Ames, IA) [1] by using advanced high field and low temperature facilities. The samples were prepared by the School of Chemistry group of the University of Manchester (UK) [2]. We could establish the consistency of our results with the calculated results regarding the redistribution of local moments in $Cr_7Ni$ by the Theoretical Matter Physics group of the University of Parma (Italy) [3] and we have determined the order of magnitude of the transferred hyperfine coupling constant $^{19}$F - $M^{n+}$ where $M^{n+} = Cr^{3+}$, $Ni^{2+}$ in the different rings. This latter result gives useful information about the overlapping of the electronic wavefunctions involved in the coordinative bond.

[1] Department of Physics and Astronomy / Ames Laboratory, Iowa State University, 50011 Ames, Iowa (USA).
[2] The Lewis Magnetism Laboratory, The University of Manchester, M13 9PL Manchester, United Kingdom.
[3] Department of Physics, Università degli Studi di Parma, I-43124 Parma (Italy).

# Chapter 1

# Molecular nanomagnets

The first section of the present chapter illustrates the general features of single molecule magnets: the class of compounds to which the cyclic metal structures studied in the present thesis belong. The second section describes the properties of antiferromagnetic molecular rings focusing on the compounds studied in the present work: $Cr_8$ homometallic ring and $Cr_7M$ heterometallic rings, where M = Cd, Ni. The chemical structure and synthesis of these macrocycles are briefly described together with the main experimental and theoretical determinations obtained in the past.

The present work experimental study on $Cr_8$, $Cr_7Cd$ and $Cr_7Ni$ molecular nanomagnets is presented in Chapter 3, Chapter 4 and Chapter 5 respectively.

## 1.1 Why single molecule magnets

The field of magnetism of molecular systems has rapidly developed at the end of the $20^{\text{th}}$ century thanks to the synergic work of chemists and physicists. Molecular magnetism is an interdisciplinary field where the chemists design materials of increasing complexity and develop sophisticated strategies of synthesis while the physicists devise ingenious experimental techniques and develop accurate theoretical models for the study of the novel magnetic properties associated with the molecular materials.

Single molecule magnets are the practical realization of zero dimensional model magnetic systems. These magnetic systems are formed by a cluster of transition metal ions bonded by means of superexchange bridges and embedded in a large organic molecule. The steric effect of the organic shell results in vanishingly small intermolecular, usually dipolar, magnetic interactions. The strong intramolecular exchange interaction among the magnetic metal ions is dominant over the the weak intercluster coupling: each molecule can therefore be considered magnetically independent. The experimental study of a macroscopic sample consisting of $\sim 10^{20}$ molecules provides information on the single non interacting magnetic entity.

Most molecular nanomagnets can be classified as coordination complexes. In chemistry, a coordination complex or metal complex essentially consists of a metallic cation sorrounded by $N$ ligands or complexing agents. Common values of $N$ are 4, 6. The ligands can be anionic species e. g. the fluoride anion $F^-$ or neutral molecules such as $H_2O$ and $NH_3$ where the electronic lone pair provides the electronic density required for the coordinative bond. The coordinative bond can be described as

the interaction between a Lewis acid in this case the metal cation, and a Lewis base in this case the ligand, where the IUPAC definition [1] of a Lewis acid (and base) is the following: *"a Lewis acid is a molecular entity that is an electron-pair acceptor and therefore able to react with a Lewis base to form a Lewis adduct, by sharing the electron pair furnished by the Lewis base"*.

In order to study the properties of the coordination complexes different complementary approaches have been adopted in the last century. The Crystal Field Theory (CFT) introduced by Hans Bethe in 1929, treats all metal-ligand interactions in a complex as ionic (i.e. purely electrostatic) and assumes that the ligands can be approximated by negative point charges. More sophisticated models embrace covalency, and this approach is described by Ligand Field Theory (LFT) and Molecular Orbital Theory (MO). Ligand Field Theory, introduced in 1935 and built from Molecular Orbital Theory, can handle a broader range of complexes and can explain complexes in which the interactions are covalent. Also, group theory has been widely used in order to establish the bonding characteristics of the metal complexes.

Many molecular nanomagnets are polymetallic complexes where the magnetic metal ions are connected by means of bridging ligands. The overall molecule can organize in a cyclic structure therefore forming a macrocycle, the class of compounds to which the molecules studied in the present work belong. A brief description of the coordinative bond in the metal wheels studied in this thesis is given in the first part of the next section.

## 1.2 Antiferromagnetic (AFM) rings

The present thesis work focuses on the study of antiferromagnetic molecular rings namely a class a wheel-shaped coordination complexes where transition metal ions are organized in a macrocyclic structure and connected by means of bridging ligands. The compounds studied in this work namely $Cr_8$, $Cr_7Cd$ and $Cr_7Ni$ are macrocyclic complexes essentially composed by eight almost coplanar transition metal cations connected by means of fluoride $F^-$ bridging ligands and pivalate $(CH_3)_3CCOO^-$ bridging ligands.

Figure 1.1 shows the ring shaped structure of $Cr_8$, $Cr_7Cd$ and $Cr_7Ni$, where the heterometallic center is not indicated in the figure since it occupies a random position. The bond between adjacent $Cr^{3+}$ ions mediated by a fluoride ion bridging ligand and by two pivalate bridging ligands has been zoomed in and is shown in the insert. The pivalate is a bidentate ligand, namely it has two donor atoms (oxygen atoms) due to the electronic charge delocalized on the carboxylate group -$COO^-$. The pivalate ligand can therefore coordinate to two metal ions, as shown in the insert.

### 1.2.1 Homometallic $Cr_8$ AFM ring

Extensive studies have been performed in the last decade on $Cr_8$ homometallic ring but still there are some open questions in particular concerning the local spin density distribution in the ring at temperatures and magnetic fields for which the excited states are populated. A brief description of this compound and of its synthesis, together with the main results obtained in the past, is reported

[1] http://goldbook.iupac.org/L03508.html

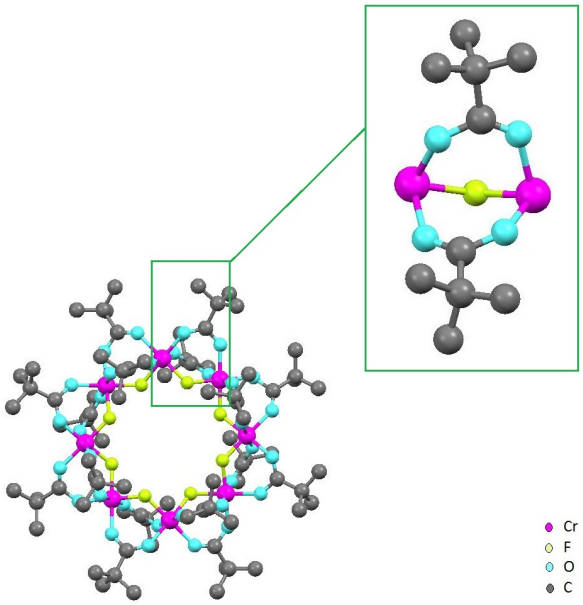


Figure 1.1: $Cr^{3+}$ - $F^-$ and $Cr^{3+}$ - $(CH_3)_3CCOO^-$ coordinative bonds. The pivalate $(CH_3)_3CCOO^-$ ligands are bridging bidentate ligands in these molecules.The hydrogen atoms are not shown for simplicity.

in the present section while the NMR measurements performed in this thesis' experimental work are illustrated in Chapter 3.

$Cr_8F_8Piv_{16}$ [$Piv^-$= Pivalate, trimethylacetate: $(CH_3)_3CCOO^-$], $Cr_8$ in short, is a widely studied homometallic antiferromagnetic molecular ring. The molecule is composed essentially by eight almost coplanar $Cr^{3+}$ magnetic ions whose electronic configuration is: $[Cr^{3+}] = [Ar]3d^3$, $s = \frac{3}{2}$. Adjacent $Cr^{3+}$ ions are connected by one $F^-$ bridging ion and two Pivalate bridging ligands. Figure 1.2 shows the crystal's unit cell: only the $Cr^{3+}$ and $F^-$ atoms relevant to the present discussion are displayed. The picture shows that in this compound the $a$-axis is directed approximatively perpendicular to the molecular ring. Figure 1.3 represents a single molecular ring including the Pivalate ligands and two Toluene molecules from the solvent of crystallization [2].

$Cr_8F_8Piv_{16}$ crystals are synthesized by heating up to 413 K and stirring a mixture of hydrated chromium(III) fluoride $CrF_3 \cdot 4\,H_2O$ and an excess of Pivalic acid $(CH_3)_3CCOOH$ in a suitable solvent. Further details about the synthesis and purification procedure can be found in the article by J. Van Slageren *et al.* [1].

As mentioned at the beginning of this paragraph, $Cr_8$ is one of the best characterized antiferromagnetic molecular rings. The spin Hamiltonian describing the magnetic system is [3]:

$$\mathcal{H} = J\sum_i \boldsymbol{s}_i \cdot \boldsymbol{s}_{i+1} + \sum_i \boldsymbol{s}_i \cdot \boldsymbol{D}_i \cdot \boldsymbol{s}_i + \sum_{i>j} \boldsymbol{s}_i \cdot \boldsymbol{D}_{ij} \cdot \boldsymbol{s}_j + \mu_B \sum_i g_i \boldsymbol{H} \cdot \boldsymbol{s}_i. \tag{1.1}$$

The first term of the Hamiltonian 1.1 describes the antiferromagnetic ($J > 0$) nearest-neighbors isotropic exchange interaction. The second term accounts for the anisotropic local crystal field and

[2]The lattice parameters for $Cr_8F_8Piv_{16}$ crystals are largely affected by the choice of the solvent.

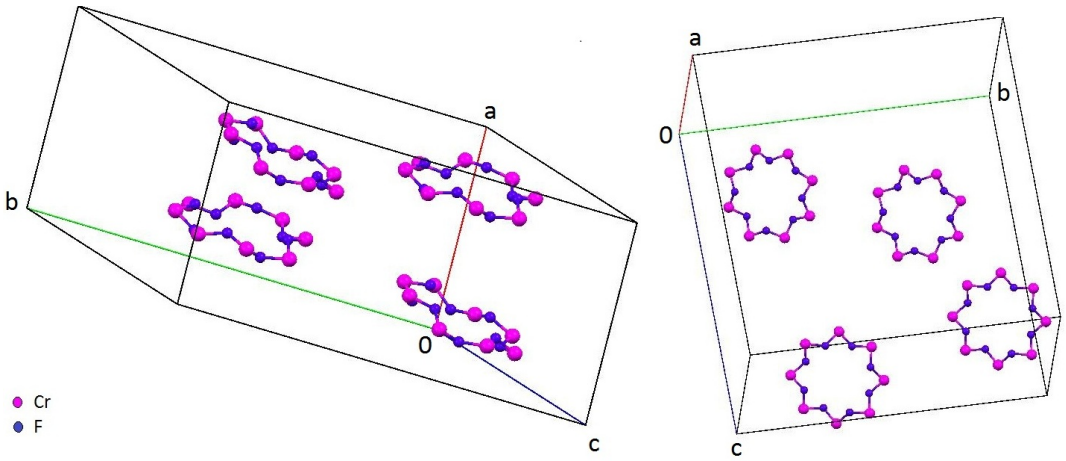


Figure 1.2: $Cr_8$ unit cell: only $Cr^{3+}$ and $F^-$ atoms are displayed. The axis perpendicular to the molecular ring is labelled with $a$. It is observed that this labelling is unusual since the axis perpendicular to the ring is usually indicated as $c$-axis.

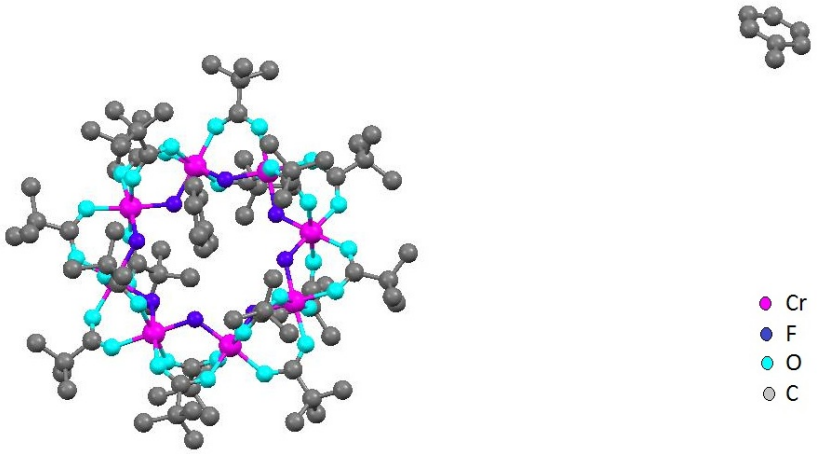


Figure 1.3: $Cr_8$ molecular ring displaying the 16 Pivalate bridging ligands and two Toluene molecules from the solvent of crystallization. The molecule is wieved along the $a$ crystallographic axis.

can be written as follows:

$$\sum_i \boldsymbol{s}_i \cdot \boldsymbol{D}_i \cdot \boldsymbol{s}_i \sim D \sum_i [s_{z,i}^2 - \frac{1}{3} s_i(s_i+1)].$$

where $z$ is the axis perpendicular to the molecular ring. The third term on the right handside is the dipole-dipole coupling between the electronic magnetic moments within the same molecule and can be evaluated by means of the point-dipole approximation. The last term is the Zeeman Hamiltonian describing the interaction between the applied field $\boldsymbol{H}$ and the electronic magnetic moments $-g_i \mu_B \boldsymbol{s}_i$ where $\mu_B$ is the Bohr magneton and $g_i$ is the Landé factor of the $i^{th}$ spin.

The energy levels obtained by the spin Hamiltonian 1.1 with parameters determined by means of Inelastic Neutron Scattering experiments [5] are shown in figure 1.4 as a function of the external magnetic field. In zero applied field the ground state is $|S, M_S\rangle = |0, 0\rangle$. As an external field is applied the ground state progressively switches from $|0, 0\rangle$ to $|1, -1\rangle$, $|2, -2\rangle$,... at corresponding critical field

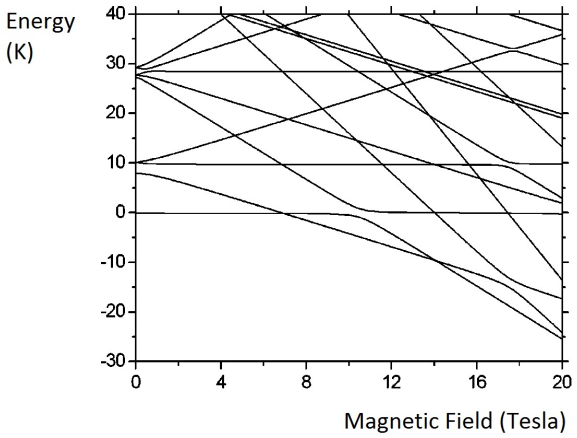


Figure 1.4: $Cr_8$ energy levels corresponding to the spin Hamiltonian 1.1 with parameters determined by means of INS [5] as a function of an applied magnetic field. The external field's direction is $\theta = 65$ degrees, where $\theta$ is the angle between the applied field and the $a$-axis perpendicular to the molecular ring.

values $H_{c1}$, $H_{c2}$, ...

$Cr_8$ ground state $|0,0\rangle$ is characterized by a molecular-type singlet magnetic configuration. This means that each *local* spin value is $\langle s\rangle^j = 0$ yielding a tolal spin $S = 0$. By contrast, Néel antiferromagnets are characterized by non-zero antiparallel local moments in the total $S = 0$ ground state. Examples of this latter situation are the antiferromagnetic compounds $KMnF_3$ [16] and $MnF_2$ [18]. Direct evidence of the local spin configuration $\langle s\rangle^j = 0$ in $Cr_8$ ground state is given in section 3.1 by means of $^{19}$F-NMR measurements [3].

Figure 1.4 shows that the energy separation between the ground state $|0,0\rangle$ and the first excited state $|1,-1\rangle$ decreases as the applied field approaches the first level crossing field $H_{c1}$. At finite temperature the thermal population of the excited level therefore increases with increasing magnetic field yielding non-zero local spin expectation values $\langle s\rangle^j$ even below the first critical field threshold $H_{c1}$.

Figure 1.5 shows the calculated values of the thermal averages of the local spin moments $\langle s\rangle^j$ as a function of the applied magnetic field at $T = 1,5$ K [4]. The expectation values $\langle s\rangle^j$ progressively [5] increase from zero at zero field and at low applied magnetic fields to 1/8 above the first level crossing value $H_{c1}$ [6]. The calculation has been performed by assuming two different orientations of the external field with respect to the molecular ring. The solid line in figure 1.5 represents the orientation $\theta = 0$ while the dashed line refers to $\theta = \pi/2$, where $\theta$ is the angle between the applied magnetic field and the $a$-axis perpendicular to the molecular ring. When the applied magnetic field orientation is $\theta = 0$ or $\theta = \pi/2$ the electronic spin vectors are aligned along the field. Figure 1.5 therefore shows

[3] The present work's $^{19}$F-NMR measurements of $Cr_8$ ground state reproduce the results obtained by E. Micotti *et al.* in 2006 [7].

[4] The values in figure 1.5 are consistent with a Zeeman Hamiltonian $-\mu_B \sum_i g_i \boldsymbol{H}\cdot\boldsymbol{s}_i$ instead of the term $+\mu_B \sum_i g_i \boldsymbol{H}\cdot\boldsymbol{s}_i$ in equation 1.1. These values therefore represent the electronic magnetic moments expressed in units of $g\mu_B$. This is consistent with the analysis carried on in the experimental section in Chapter 3.

[5] This curve has a stepwise shape at very low temperatures (i. e. 0,5 K [6]) while figure 1.5 refers to $T = 1,5$ K. As the temperature increases the stepwise discontinuities are smoothed out.

the expectation value of the spin component parallel to the magnetic field. It is worthwhile observing that in this model the eight local electronic spins are parallel to each other and have the same value.

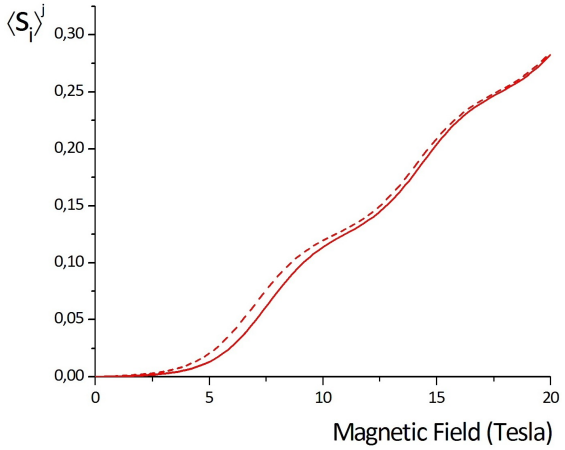


Figure 1.5: Expectation value of the component along the applied field of the $j^{\text{th}}$ local electronic magnetic moment expressed in Bohr magnetons at $T = 1,5$ K in $Cr_8$. Solid line: $\theta = 0$. Dashed line: $\theta = \pi/2$. $\theta$ is the angle between the applied magnetic field and the $a$-axis perpendicular to the molecular ring.

The values $H_{c1} = 6,9$ Tesla and $H_{c2} = 14,0$ Tesla have been determined by means of torque magnetometry measurements [3]. Magnetization measurements have been performed on polycrystalline $Cr_8$ by using a pulsed magnet and a dilution $^3$He - $^4$He cryostat at $T = 0,15$ K at the ISSP of the University of Tokyo [6]. The magnetization curve as a function of the external field $H$ is shown in figure 1.6. The value $H_{c1} = 7,3$ Tesla has been determined [6] by means of the first peak position in $\frac{dM}{dH}$ shown by the upper curve in figure 1.6.

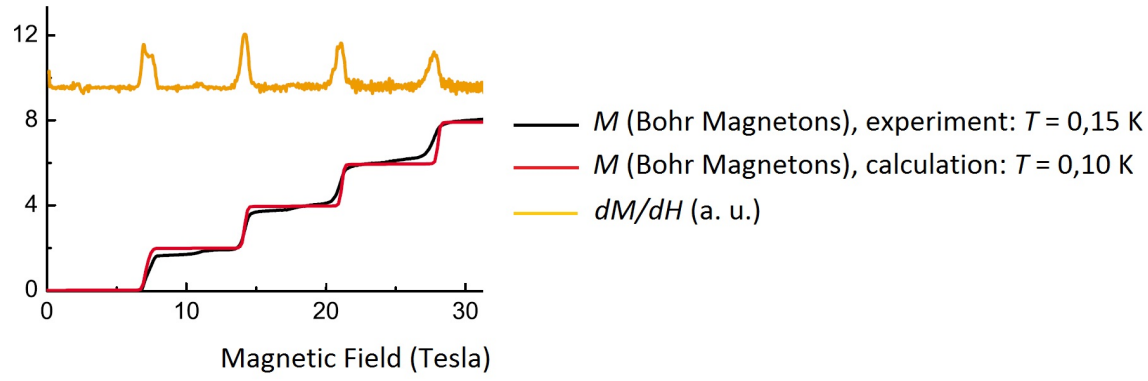


Figure 1.6: Polycrystalline $Cr_8$ magnetization curves as a function of the applied magnetic field $H$. The black line shows the experimental results at $T = 0,15$ K while the red line is the theoretical calculation at $T = 0,10$ K. The upper orange line shows the derivative $dM/dH$.

Polycrystalline $Cr_8$ magnetic susceptibility $\chi$ has been measured in the temperature range 1,8 - 300 K by means of a Superconducting QUantum Interference Device (SQUID) magnetometer. Figure 1.7 (left) shows the temperature dependence of $Cr_8$ magnetic susceptibility characterized by a broad maximum around 40 K due to the antiferromagnetic interaction between the $Cr^{3+}$ spins [6]. It is

worthwhile observing that $\chi$ approaches zero at low temperatures reflecting the singlet ground state.

Figure 1.7 (right) shows the $\chi T$ behaviour in polycrystalline $Cr_8$ as a function of the temperature $T$ at two external magnetic fields [26]. This plot essentially shows the temperature dependence of the effective Curie constant $C \sim \chi T$ where:

$$C = \frac{Ng^2\mu_B^2[S(S+1)]}{3k_B}. \tag{1.2}$$

The lower dashed line corresponds to the low temperature limit, given by equation 1.2 with $N = 1$, $g = 2$ and $S = 0$, namely the Curie constant for a single spin $S = 0$. This indicates that at low temperature the eight spins system occupies a collective ground state characterized by the total spin value $S = 0$. Viceversa, the upper dashed line represents the high temperature limit corresponding to an effective Curie constant given by $N = 8$, $g = 2$ and $S = 3/2$. The high temperature spin dynamics is determined by local spins of the magnetic ions fluctuating almost independently from each other.

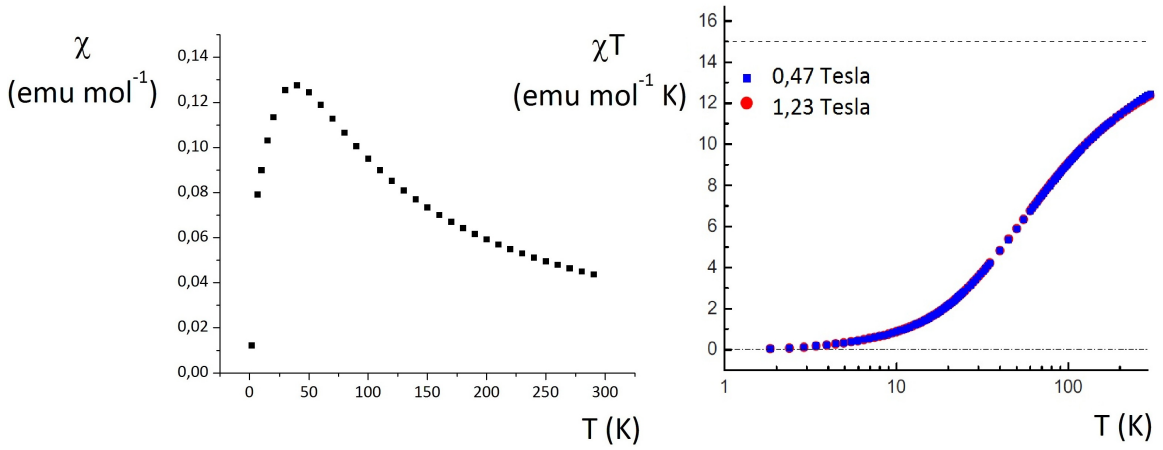


Figure 1.7: Polycrystalline $Cr_8$ magnetic susceptibility versus $T$ measured in the temperature range 1,8 - 300 K by means of a SQUID magnetometer (left). $\chi T$ behaviour as a function of $T$ at two external magnetic fields [26] (right).

Figure 1.8 represents the temperature dependence of the magnetic susceptibility $\chi$ at different values of the applied magnetic field. It is worthwhile stressing that a field dependence of $\chi$ is observed at low temperature. In particular, at low temperature $\chi$ increases with increasing magnetic field together with the $S = 1$ state population. By contrast, at high temperature $\chi$ shows a field independent paramagnetic behaviour.

### 1.2.2 Heterometallic $Cr_7Cd$ and $Cr_7Ni$ AFM rings

The present section illustrates the properties of the heterometallic rings studied in the experimental part of this work namely $Cr_7Cd$ and $Cr_7Ni$ antiferromagnetic rings. The substitution of one $Cr^{3+}$ ion ($s = 3/2$) by a dication $Cd^{2+}$ ($s = 0$) or $Ni^{2+}$ ($s = 1$) results in a magnetic ground state with total spin $S = 3/2$ and $S = 1/2$ in $Cr_7Cd$ and $Cr_7Ni$ respectively. While $Cr_8$ ground state is characterized by a molecular type singlet $S = 0$, with zero local spin expectation values; the heterometallic rings are characterized by a redistribution of the magnetic moment in the ground state as described in the

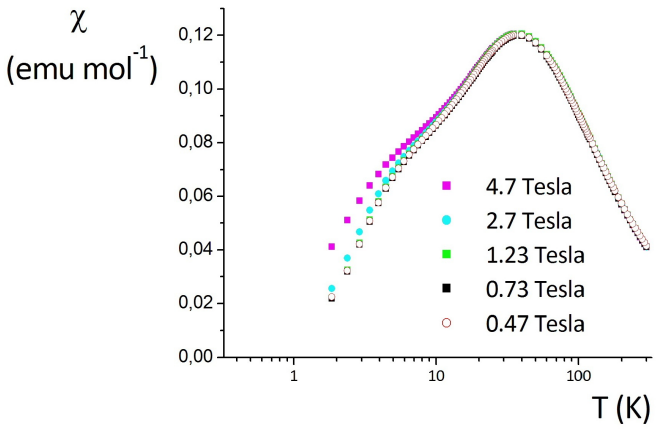


Figure 1.8: $Cr_8$ powders magnetic susceptibility versus $T$ at different applied magnetic fields.

following. This section briefly illustrates the structure and synthesis of these compounds together with the main results obtained in the past concerning their magnetic properties. This thesis' experimental study on $Cr_7Cd$ and $Cr_7Ni$ is illustrated in Chapter 4 and in Chapter 5 respectively.

Heterometallic analogues of the homometallic neutral wheel $Cr_8F_8Piv_{16}$, in short $Cr_8$ have been prepared by replacing a single $Cr^{3+}$ center by a dication $M^{2+}$. The monoanionic heterometallic species $[Cr_7MF_8Piv_{16}]^-$ is therefore formed and in the presence of a suitable cation it is possible to separate the heterometallic species from the homometallic compound based on the principle that a cation-anion pair has different crystallization properties than a neutral species. The syntheses of $(CH_3)_2NH_2[Cr_7NiF_8Piv_{16}]$ in short $Cr_7Ni$ and $(CH_3)_2NH_2[Cr_7CdF_8Piv_{16}]$ in short $Cr_7Cd$ are briefly reported in the following. The interested reader can find more details in reference [2].

$Cr_7Ni$ heterometallic wheel can be synthesized by means of two strategies. The first route consists in preparing a mixture of hydrated chromium(III) fluoride i. e. $CrF_3 \cdot 4\ H_2O$ and $Ni_2Piv_4HPiv_4{\cdot}H_2O$ in Pivalic acid HPiv = $(CH_3)_3CCOOH$ and dimethylformamide DMF. The mixture is stirred and heated up to 413 K. $(CH_3)_2NH_2[Cr_7NiF_8Piv_{16}]$ in short $Cr_7Ni$ is produced together with a smaller amount of $Cr_8F_8Piv_{16}$, $Cr_8$ in short. The amonium ion $[(CH_3)_2NH_2]^+$ formation is probably due to the acid hydrolysis of DMF i. e. $(CH_3)_2NCOH$. The product is purified by column cromatography on silica gel by using toluene as a eluent. First the less polar impurity $Cr_8$ is eluted, then the product $Cr_7Ni$. The product is recrystallized from $THF/CH_3CN$.

The second route involves the reaction of $CrF_3 \cdot 4\ H_2O$ and $Ni_2Piv_4HPiv_4{\cdot}H_2O$ in a mixture of secondary amine $(CH_3)_2NH$ and pivalic acid $(CH_3)_3CCOOH$. The mixture is stirred and heated up to 413 K. $(CH_3)_2NH_2[Cr_7NiF_8Piv_{16}]$ in short $Cr_7Ni$ is obtained with no trace of $Cr_8F_8Piv_{16}$, $Cr_8$ in short. $(CH_3)_2NH_2[Cr_7CdF_8Piv_{16}]$ in short $Cr_7Cd$ synthesis is performed by means of the same procedure by using cadmium carbonate $CdCO_3$ instead of $Ni_2Piv_4HPiv_4{\cdot}H_2O$.

Figure 1.9 shows the $Cr_7M$ (M = Cd, Ni) heterometallic ring unit cell viewed along the $c$ axis perpendicular to the molecular ring. It is worthwhile observing that the axis perpendicular to the molecular ring is labelled with $a$ in $Cr_8$ and with $c$ in heterometallic $Cr_7Cd$ and $Cr_7Ni$. The sample has been crystallized from THF/MeCN 1:10. A secondary amonium cation is found in the cavity of

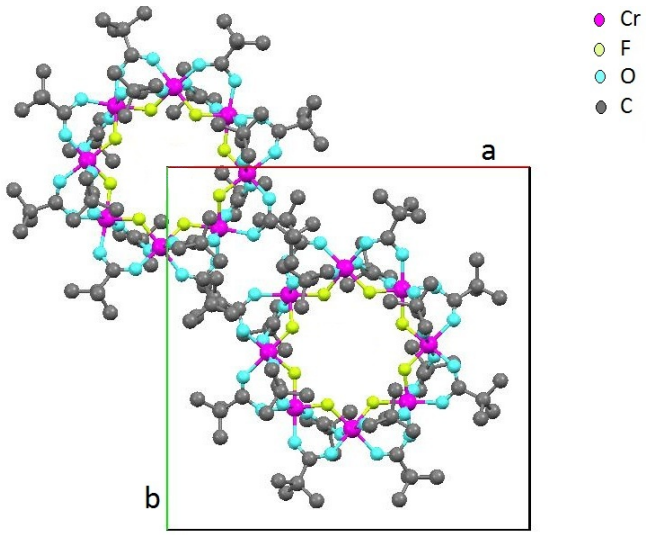


Figure 1.9: $Cr_7M$ (M = Cd, Ni) heterometallic ring unit cell viewed along the $c$ axis perpendicular to the molecular ring. The sample has been crystallized from THF/MeCN 1:10. Each molecular ring includes one amonium ion at its center, not shown in this figure. The heterometallic site occupies a random position on the ring and therefore has not been labelled.

the macrocycle forming three N - H $\cdots$ F bonds as shown in figure 1.10 [6]. The heterometallic site occupies a random position on the ring and therefore has not been labelled.

As in the case of $Cr_8$ the spin Hamiltonian describing the magnetic $Cr_7M$ ring is given by equation 1.1 here rewritten for convenience:

$$\mathcal{H} = J\sum_i \boldsymbol{s}_i \cdot \boldsymbol{s}_{i+1} + D\sum_i [s_{z,i}^2 - \frac{1}{3}s_i(s_i+1)] + \sum_{i>j} \boldsymbol{s}_i \cdot \boldsymbol{D}_{ij} \cdot \boldsymbol{s}_j - \mu_B \sum_i g_i \boldsymbol{H} \cdot \boldsymbol{s}_i. \qquad (1.3)$$

As stated above for the case of $Cr_8$ (see section 1.2.1), the first term describes the dominant isotropic nearest-neighbors Heisenberg exchange interaction. The coupling is antiferromagnetic ($J > 0$): in particular in $Cr_7Ni$ the nearest neighbours exchange constants are: $J_{Cr-Cr} = 16,9$ K and $J_{Cr-Ni} = 19,6$ K. The second term accounts for the uniaxial local crystal fields, where $z$ is the axis perpendicular to the molecular ring. The third term on the right handside of equation 1.3 is the dipolar anisotropic intracluster spin-spin interaction where $\boldsymbol{D}_{ij}$ can be evaluated by means of the point-dipole approximation. The last term is the Zeeman Hamiltonian describing the interaction between the applied field $\boldsymbol{H}$ and the electronic magnetic moments $g_i\mu_B\boldsymbol{s}_i$ where $\mu_B$ is the Bohr magneton and $g_i$ is the Landé factor of the $i^{th}$ spin [7].

The dimension of the spin Hilbert space is very large (49152 in the case of $Cr_7Ni$) and the magnetic Hamiltonian has been diagonalized by means of the two-steps procedure summarized in the following [21], [4]. The Heisenberg interaction represents the dominant contribution to the spin Hamiltonian. Its energy spectrum consists of a series of multiplets with an almost definite value of $|\boldsymbol{S}|$. In the

[6] The secondary amonium ion $[(CH_3CH_2)_2NH_2]^+$ is shown in figure 1.10 while in figure 1.9 the amonium ion is not displayed. The compounds studied in the present work include a $[(CH_3)_2NH_2]^+$ ion.

[7] The Zeeman term in equation 1.3 is written in the assumption that the $g_i\boldsymbol{s}_i$ values are the magnetic moments expressed in Bohr magnetons differently from equation 1.1. This is consistent with figures 1.14, 1.15 and 1.16 and with the analysis of the experimental results in Chaper 4 and in Chapter 5.

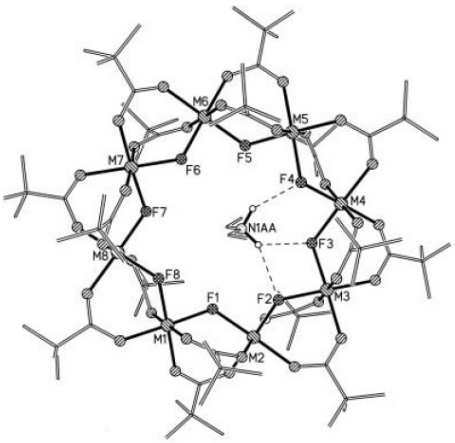


Figure 1.10: $Cr_7M$ (M = Cd, Ni) heterometallic ring. A secondary amonium cation is found in the cavity of the macrocycle forming three N - H $\cdots$ F bonds [2].

first step of the diagonalization procedure only the Heisenberg term is considered. By exploiting the rotational invariance of the Heisenberg term the matrix has been block factorized according to the total spin quantum number $S$ and the eigenstates and eigenvalues have been calculated. However the complete Hamiltonian does not commute with $S^2$ and the different spin multiplets can mix. Since the $S$-mixing is small a perturbative approach (see references [8] and [9]) could be employed in order to include the $S$-mixing in the results.

Figure 1.12 displays a plot of the energy levels in $Cr_7Ni$ calculated by means of the Hamiltonian 1.3 in the case of the magnetic field being applied perpendicular to the molecular ring (left) and in the case of the magnetic field being applied parallel to the molecular ring (right). It is worthwhile observing that the lowest level (i. e. the state $|1/2, 1/2\rangle$ at low fields) has been arbitrarily represented by an horizontal line.

The calculated eigenstates and eigenvalues of the spin Hamiltonian 1.3 have been used to evaluate the magnetic field dependence of the thermal averages of the local spin operators $\langle s\rangle_{\alpha,i}$ where $\alpha = x, y, z$ both in $Cr_7Cd$ and in $Cr_7Ni$ according to [4]:

$$\langle s\rangle_{\alpha,i} = \frac{1}{Z}\sum_j \langle j|s_{\alpha,i}|j\rangle e^{-\beta E_j(H)} \tag{1.4}$$

where $Z$ is the partition function and $\beta = \frac{1}{k_B T}$. The sum extends over the eigenstates $|j\rangle$ and the field dependent eigenvalues $E_j(H)$. It turns out that in the case of the magnetic field being applied along the $z$ axis perpendicular to the molecular ring i. e. $\theta = 0$, $\langle s\rangle_{z,i}$ is the only non zero component of the local spin vectors. Viceversa, when the magnetic field is parallel to the moecular ring i. e. $\theta = \pi/2$ we get $\langle s\rangle_{z,i} = 0$ and the local spin vectors are parallel to the applied field.

Figure 1.14 shows the local expectation values of the electronic spin moments in $Cr_7Cd$ calculated at $T = 1,5$ K in the case of the magnetic field being applied perpendicular to the molecular ring [21] (left) and in the case of the magnetic field being applied parallel to the molecular ring (see the $Cr^{3+}$ ions labelling in use for the heterometallic wheels in figure 1.13). The plot shows that the local spin expectation values $\langle s\rangle_{\alpha,i}$ have a staggered almost uniform distribution and the spin values turn out to be significantly lower than the $s = \frac{3}{2}$ value of the $Cr^{3+}$ ion. The calculated values shown in figure

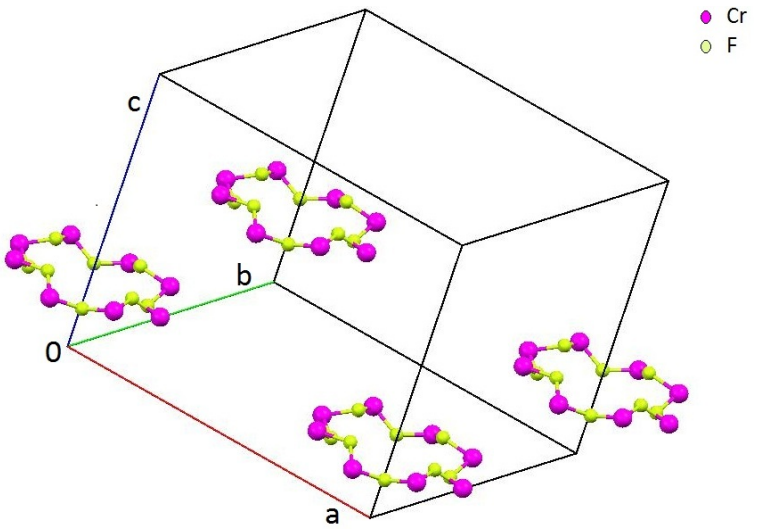


Figure 1.11: $Cr_7M$ (M = Cd, Ni) heterometallic ring unit cell showing that the $c$ axis is perpendicular to the molecular ring. The sample has been crystallized from THF/MeCN 1:10. Only $Cr^{3+}$, $M^{2+}$ and $F^-$ atoms are displayed. The heterometallic site occupies a random position on the ring and therefore has not been labelled.

1.14 are in very good agreement with the experimentally determined values [21] (see section 4.1).

Figure 1.15 and 1.16 show the theoretical $Cr^{3+}$ and $Ni^{2+}$ electronic magnetic moments local expectation values in $Cr_7Ni$ at $T = 0$ K and $T = 1,5$ K respectively. These results are expressed in Bohr magnetons. $g$ is the electronic Landé factor whose value is 1,98 for the $Cr^{3+}$ ions and 2,2 for the $Ni^{2+}$ ion. The theoretical values have been calculated at both temperatures in the cases of the magnetic field being applied both perpendicular to the molecular ring (see figure 1.15 left and 1.16 left) and parallel to the molecular ring (see figure 1.15 right and 1.16 right).

The Hamiltonian describing $Cr_7Ni$ has an axial simmetry and the simmetry axis is perpendicular to the molecular ring. Thus if the external magnetic field is applied along this simmetry axis or perpendicular to this axis the local spin moments are parallel to the external field, as pointed out above. Viceversa, if the magnetic field is randomly oriented, the local spin expectation values have two non-zero components. Due to the cylindrical simmetry of the magnetic Hamiltonian, the spin expectation values do not depend on the particular in-plane magnetic field direction when this is applied parallel to the molecular ring.

It is worthwhile observing that the local spin moments moduli at $T = 1,5$ K at low magnetic fields are substantially smaller than the 0 K values. This is due to the non-zero excited levels thermal population at $T = 1,5$ K at low fields. As shown in figure 1.12 the energy separation between the ground state and the first excited state increases with increasing magnetic field and is maximum around 6 Tesla. Due to the Boltzmann factor the excited level population therefore decreases with increasing field in the range 0 - 6 Tesla and the 1,5 K electronic spin moment local expectation values approach the 0 K values.

Because of the simmetry properties of $Cr_7Ni$ magnetic system, Cr 1 and Cr 7 are expected to have the same local spin expectation value, as well as the pairs Cr 2 - Cr 6 and Cr 3 - Cr 5 (see the labelling introduced in figure 1.13). Cr 4 is expected to have a different spin value. It actually turns out that

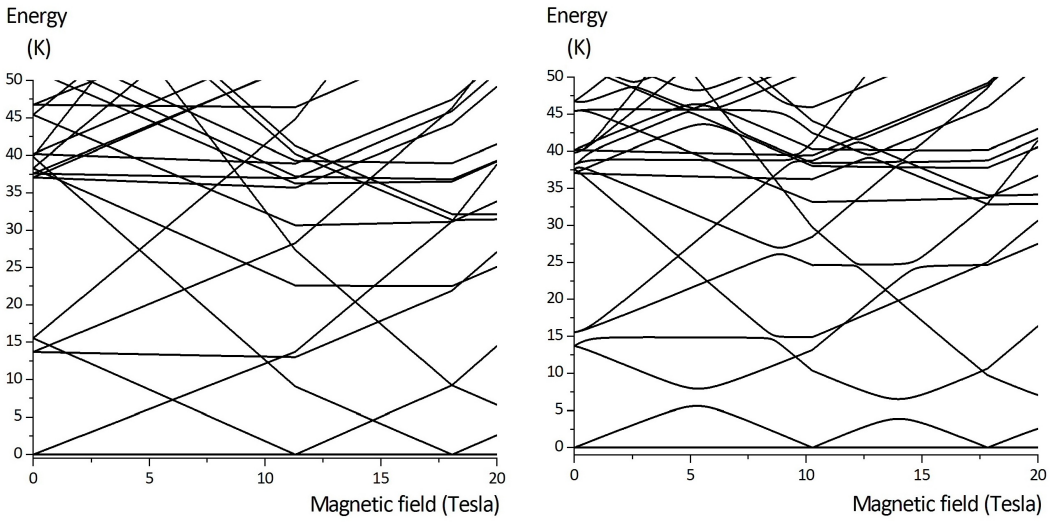


Figure 1.12: Energy levels expressed in K as a function of the magnetic field in $Cr_7Ni$. Left: $\theta = 0$. Right: $\theta = \pi/2$. $\theta$ represents the angle betwen the applied magnetic field and the $c$-axis perpendicular to the molecular ring. The lowest level has been arbitrarily represented by an horizontal line.

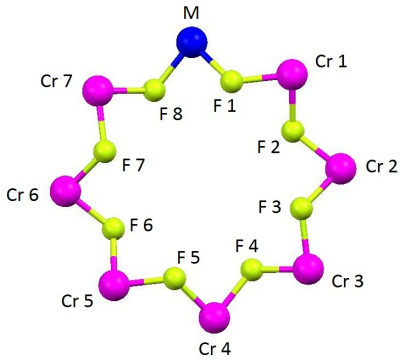


Figure 1.13: $Cr^{3+}$ and $F^-$ ions labelling in use for the $Cr_7M$ heterometallic rings, $M^{2+} = Cd^{2+}$, $Ni^{2+}$.

Cr 4 local spin expectation value is very close to the one of the Cr 2 - Cr 6 pair.

As for the case of $Cr_8$ in section 1.2.1 we give in the following a brief description of the macroscopic magnetization and suscebtibility measurements in the heterometallic rings. $Cr_7Ni$ magnetic susceptibility $\chi$ has been measured in the temperature range 2 - 300 K by means of a Superconducting QUantum Interference Device (SQUID) magnetometer. Figure 1.17 shows the temperature dependence of $Cr_7Ni$ magnetic susceptibility measured by applying a 0,47 Tesla magnetic field. The curve is characterized by a broad maximum around 40 K due to the antiferromagnetic interaction between the $Cr^{3+}$ spins [6].

Figure 1.18 shows the $\chi T$ behaviour in $Cr_7Cd$ (left) and in $Cr_7Ni$ (right) single crystals as a function of the temperature $T$ at two external magnetic fields [26]. This plot essentially shows the temperature dependence of the effective Curie constant $C \sim \chi T$ as observed in section 1.2.1 relating

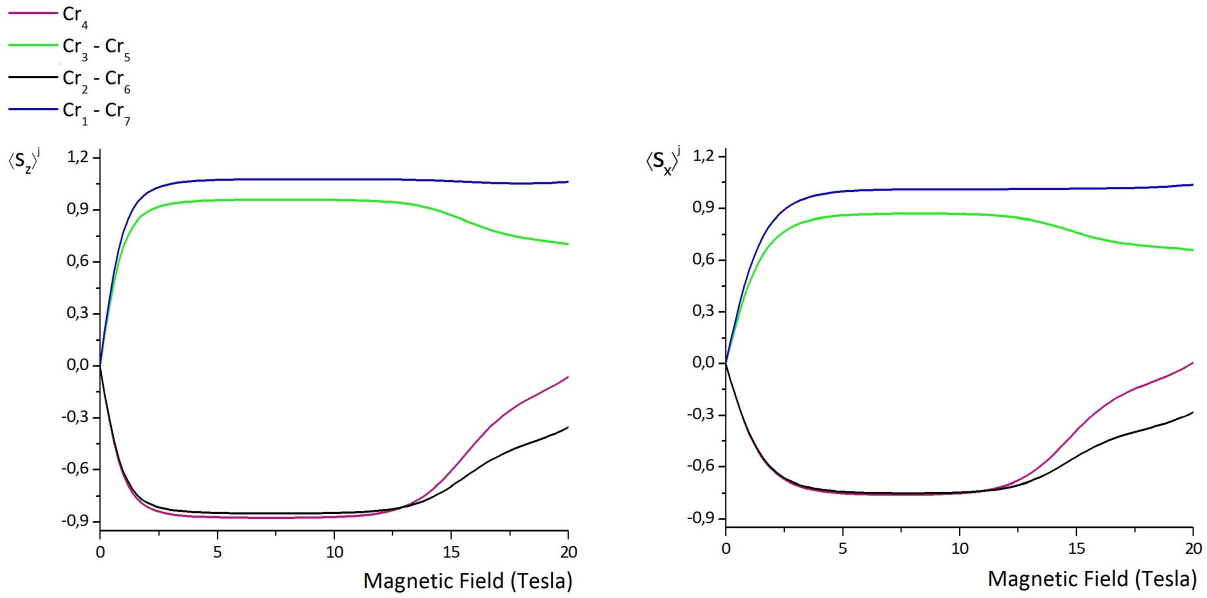


Figure 1.14: Local expectation values of the electronic spin moments in $Cr_7Cd$ calculated at $T = 1,5$ K. Left: $\theta = 0$ i. e. the magnetic field is applied perpendicular to the molecular ring [21]. Right: $\theta = \pi/2$ i. e. the magnetic field is applied parallel to the molecular ring.

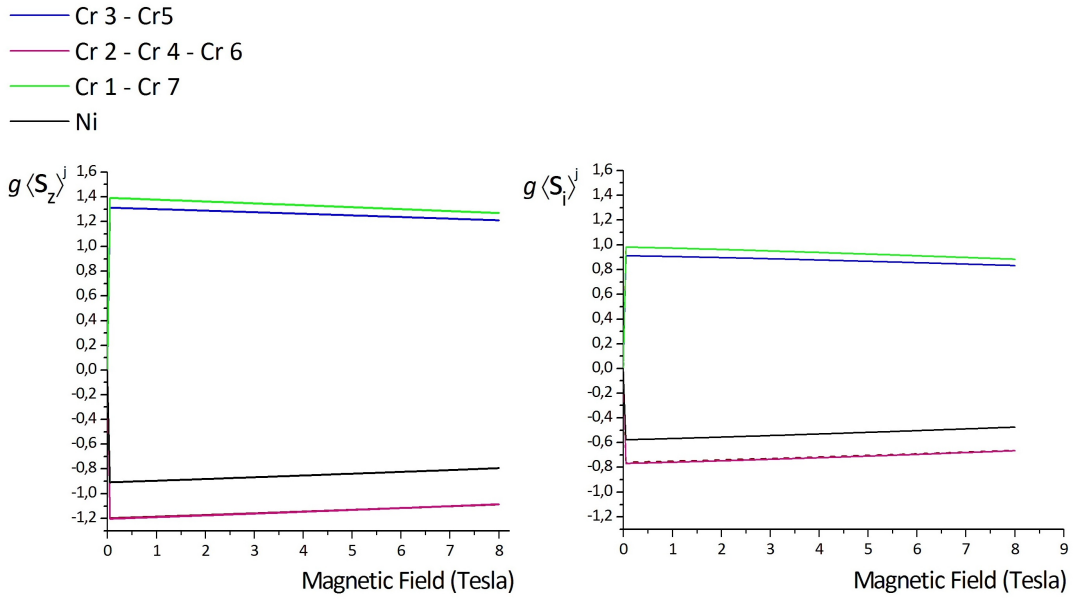


Figure 1.15: Local expectation values of the electronic spin moments in $Cr_7Ni$ calculated at $T = 0$ K. Left: $\theta = 0$ i. e. the magnetic field is applied perpendicular to the molecular ring. Right: $\theta = \pi/2$ i. e. the magnetic field is applied parallel to the molecular ring.

to $Cr_8$. Equation 1.2 holds and is here rewritten for convence:

$$C = \frac{Ng^2\mu_B^2[S(S+1)]}{3k_B}. \tag{1.5}$$

In figure 1.18 the lower dashed line corresponds to the low temperature limit, given by equation 1.5

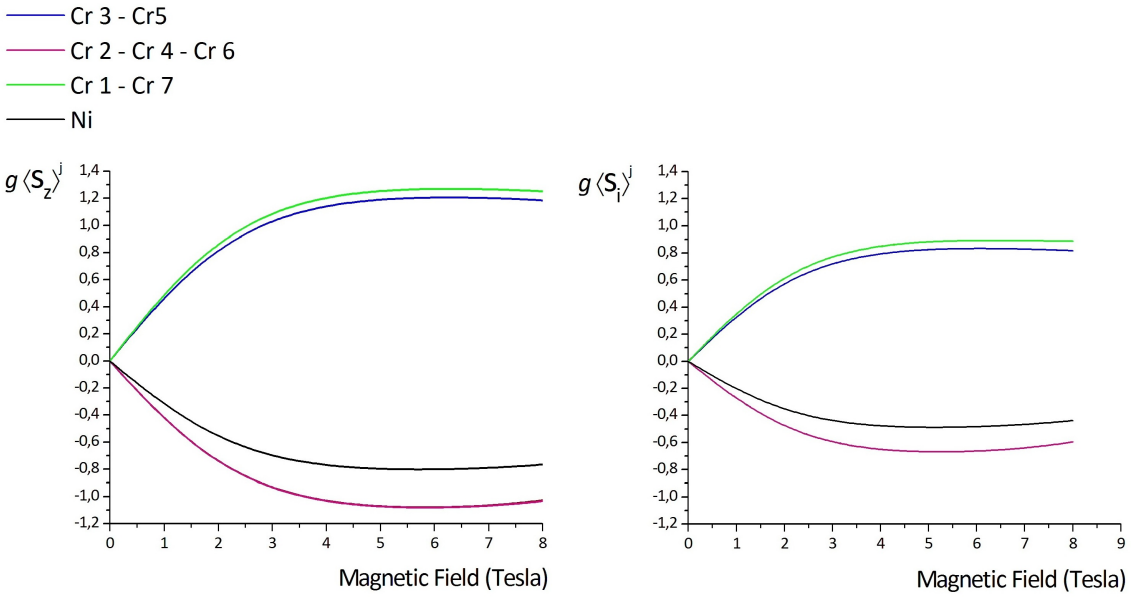


Figure 1.16: Local expectation values of the electronic spin moments in $Cr_7Ni$ calculated at $T = 1,5$ K. Left: $\theta = 0$ i. e. the magnetic field is applied perpendicular to the molecular ring. Right: $\theta = \pi/2$ i. e. the magnetic field is applied parallel to the molecular ring.

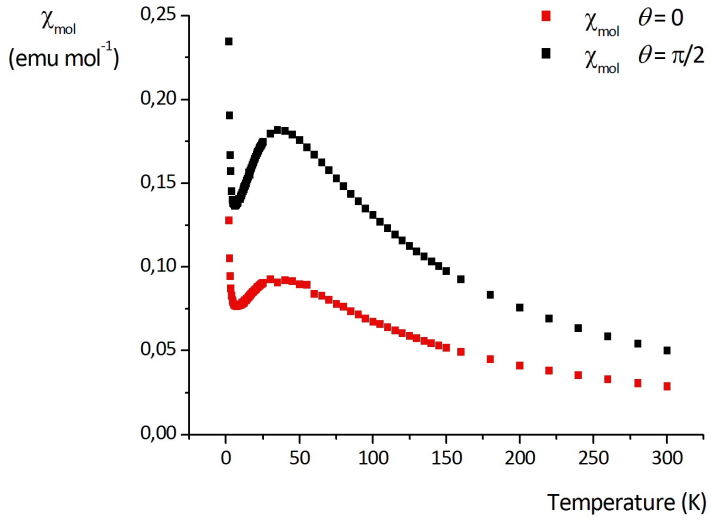


Figure 1.17: $Cr_7Ni$ magnetic susceptibility obtained by orienting the magnetic field parallel to the crystallographic $c$-axis i. e. $\theta = 0$ (red points) and by orienting the magnetic field perpendicular to the crystallographic $c$-axis i. e. $\theta = \pi/2$ (black points) The applied magnetic field equals 0,47 Tesla.

with $N = 1$, $g = 2$, $S = 3/2$ in $Cr_7Cd$ and $N = 1$, $g = 2$, $S = 1/2$ in $Cr_7Ni$, namely the Curie constant for a single spin $S$. In the low temperature limit the magnetic ring is therefore characterized by a collective grund state with total spin $S$. On the other hand, the upper dashed line represents the high temperature limit corresponding to an effective Curie constant given by the sum of two contributions. In the case of $Cr_7Cd$ the contribution given by equation 1.2 with $N = 7$, $g = 2$ and $s = 3/2$ adds

to the term obtained by means of equation 1.2 with $N = 1$, $g = 2$ and $S = 0$. Similarly, in the case of $Cr_7Ni$ the contribution given by equation 1.2 with $N = 7$, $g = 2$ and $S = 3/2$ adds to the term obtained by equation 1.2 with $N = 1$, $g = 2$ and $S = 1$. This result shows that the high temperature spin dynamics is determined by almost independent local electronic spins.

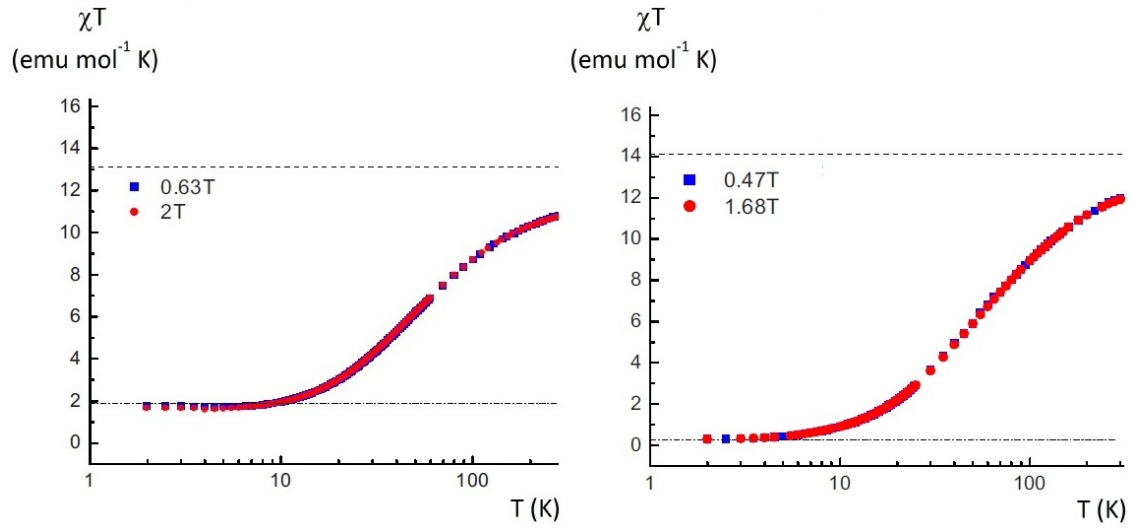


Figure 1.18: $Cr_7Cd$ (left) and $Cr_7Ni$ (right) single crystals temperature dependence of the effective Curie constant $\chi T$ at two different values of the magnetic field. The measurements have been performed by means of a SQUID magnetometer by orienting the applied field perperpendicular to the crystallographic $c$-axis.

Figure 1.19 shows the magnetization dependence on the magnetic field in $Cr_7Ni$. Both the theoretical and the experimental curves are displayed. This plot shows a step-wise behaviour due to the change of the system ground state as the magnetic field approaches the critical values corresponding to the level crossing fields in figure 1.12. It is worthwhile observing that the stepwise discontinuities are smoothed out as the temperature increases. Figure 1.20 shows the calculated magnetization dependence on the magnetic field in $Cr_7Ni$ at different temperatures and at different orientations of the applied field. It is worthwhile observing that the anisotropy shown by the total magnetization in figure 1.20 is significantly smaller than the anisotropy of the single magnetic moments in figure 1.16.

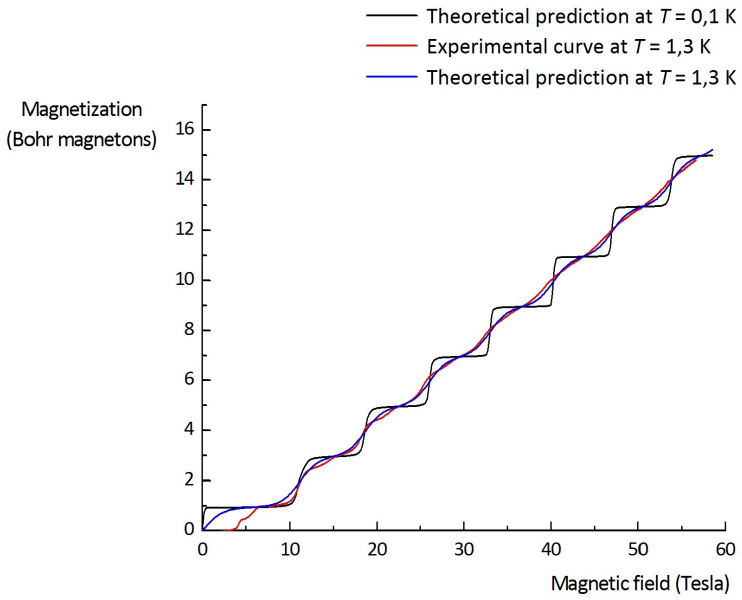


Figure 1.19: Magnetization dependence on the applied magnetic field in $Cr_7Ni$. The experimental curve at $T = 1,3$ K is shown together with the theoretical predictions at $T = 0,1$ K and $T = 1,3$ K.

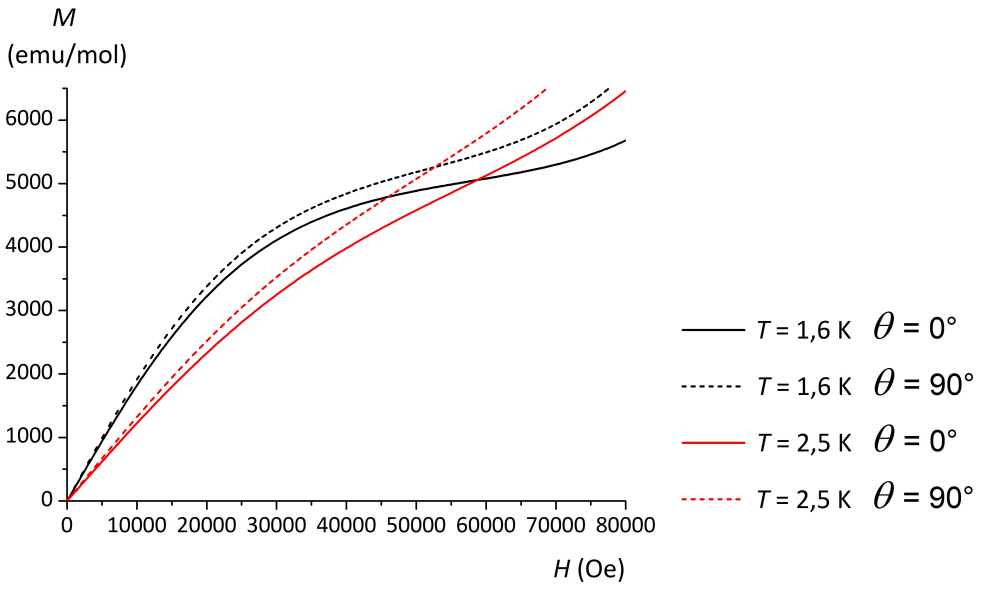


Figure 1.20: Magnetization dependence on the applied magnetic field in $Cr_7Ni$. The theoretical predictions at different temperatures and orientations of the applied field.

# Chapter 2

# Nuclear Magnetic Resonance, hyperfine interactions and experimental setup

The aim of this chapter is to recall the basic aspects of Nuclear Magnetic Resonance. The interested reader can find an elementary description of NMR in the book by T. C. Farrar and E. D. Becker [10]. A complete formal derivation of the theory of NMR can be found in the book by C. P. Slichter [11] and in the famous monograph by A. Abragam [12]. The experimental aspects of pulse NMR are described in great details in the book by E. Fukushima and S. B. W. Roeder [13].

We present in this chapter a detailed treatment of the hyperfine interactions that are relevant to the present work. We finally include a brief description of the experimental setup and of the experimental methods utilized.

## 2.1 Simple quantum mechanical treatment

Let us consider a nuclear magnetic moment:

$$\boldsymbol{\mu} = \gamma \hbar \boldsymbol{I} \tag{2.1}$$

where $\gamma$ is the gyromagnetic ratio and $\hbar \boldsymbol{I}$ is the nuclear angular momentum. The Zeeman interaction with a magnetic field $\boldsymbol{H}_0$ along the $z$ axis is described by the Hamiltonian:

$$\mathcal{H} = -\gamma \hbar \boldsymbol{I} \cdot \boldsymbol{H}_0. \tag{2.2}$$

The corresponding eigenvalues are:

$$E = -\gamma \hbar M_I H_0 \qquad M_I = -I, ..., I-1, I \tag{2.3}$$

as shown in figure 2.1 in the case $I = \frac{3}{2}$.

A time dependent perturbation of the Zeeman Hamiltonian 2.2 can induce a transition between those energy levels. A small alternating magnetic field applied perpendicular to the static field $\boldsymbol{H}_0$,

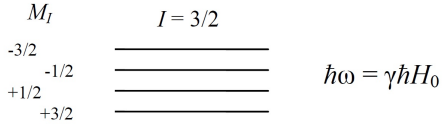


Figure 2.1: Energy eigenvalues of the Zeeman Hamiltonian 2.2 assuming $I = \frac{3}{2}$.

let's say along the $x$ axis, gives rise to the perturbing term:

$$\mathcal{H}_{\text{Pert}} = -\gamma\hbar I_x H_1 \cos(\omega t) \tag{2.4}$$

where the time dependent field is:

$$\boldsymbol{H}_1 = H_1 \cos(\omega t)\hat{\boldsymbol{x}}. \tag{2.5}$$

The matrix elements $\langle M_I'|I_x|M_I\rangle$ vanish unless $M_I' = M_I \pm 1$ [11]. Thus magnetic dipole transitions [15] occur between adjacent levels. The conservation of energy requires:

$$\hbar\omega = \gamma\hbar H_0. \tag{2.6}$$

## 2.2 Classical description and Bloch equations

A simple quantum mechanical treatment of the resonance phenomenum has been introduced in section 2.1. In addition to this, an elementary classical description can be considered. The classical picture turns out to be particularly helpful in discussing transient effects.

### 2.2.1 Precession of a magnetic moment in a magnetic field

The classical equation:

$$\hbar\dot{\boldsymbol{I}} = \boldsymbol{\mu} \times \boldsymbol{H}_0 \tag{2.7}$$

describes the motion of the magnetic moment $\boldsymbol{\mu}$ in the static field $\boldsymbol{H}_0$. By using equation 2.1 we get:

$$\dot{\boldsymbol{I}} = -\gamma \boldsymbol{H}_0 \times \boldsymbol{I}. \tag{2.8}$$

This equation describes the classical precession of $\boldsymbol{\mu}$ about the field $\boldsymbol{H}_0$ at the Larmor frequency:

$$\boldsymbol{\omega}_0 = \gamma \boldsymbol{H}_0 \tag{2.9}$$

as shown in figure 2.2. It is worthwhile stressing that the classical result 2.9 is identical to the quantum mechanical one in equation 2.6.

Let us consider a frame of reference $S'$ that rotates about the $z$ axis at an angular frequency $\omega$. The magnetic field is written $H_0\hat{\boldsymbol{z}}$ in the laboratory frame of reference $S$ and $(H_0 - \frac{\omega}{\gamma})\hat{\boldsymbol{z}}'$ in the rotating frame $S'$ [1]. We assume now that a magnetic field $\boldsymbol{H}_1 = 2H_1 \cos(\omega t)\hat{\boldsymbol{x}}$ is applied along the $x$ axis in the laboratory frame. This field may be written as the sum of a clockwise and a counterclockwise

[1] Notice that $\hat{\boldsymbol{z}} = \hat{\boldsymbol{z}}'$.

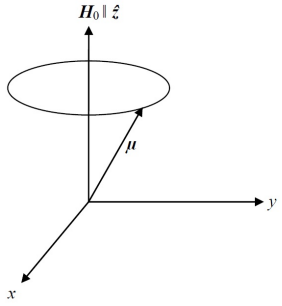


Figure 2.2: Precessional motion of a nuclear magnetic moment $\boldsymbol{\mu}$ about the static magnetic field $\boldsymbol{H}_0$.

rotating components [2]. One of those components therefore lies along the rotating frame $x'$ axis. It can be shown that only this component affects the motion of $\boldsymbol{\mu}$ [3]. In the rotating frame the magnetic moment $\boldsymbol{\mu}$ experiences an effective magnetic field:

$$\boldsymbol{H}_{\text{Eff}} = (H_0 - \frac{\omega}{\gamma})\hat{\boldsymbol{z}}' + H_1\hat{\boldsymbol{x}}'. \tag{2.10}$$

Resonance is achieved when:

$$\omega = \omega_0. \tag{2.11}$$

Equation 2.10 yields:

$$\boldsymbol{H}_{\text{Eff}} = H_1\hat{\boldsymbol{x}}'. \tag{2.12}$$

The discussion developed so far shows the following. Let us assume that the static field $H_0\hat{\boldsymbol{z}}$ is perturbed by the radiofrequency field $H_1\hat{\boldsymbol{x}}'$ lying along the $x'$ axis in the frame $S'$ rotating at $\omega$. As the resonance condition 2.11 is achieved equation 2.12 holds. The magnetic moment $\boldsymbol{\mu}$ precesses about the $x'$ axis in the rotating frame at a frequency $\omega_1 = \gamma H_1$.

### 2.2.2 Bloch equations and magnetic susceptibility

Within the classical approach, the time evolution of the nuclear magnetization $\boldsymbol{M}$ can be described by the Bloch equations:

$$\frac{dM_z}{dt} = \gamma(\boldsymbol{M} \times \boldsymbol{H})_z + \frac{M_0 - M_z}{T_1} \tag{2.13}$$

$$\frac{dM_{x,y}}{dt} = \gamma(\boldsymbol{M} \times \boldsymbol{H})_{x,y} - \frac{M_{x,y}}{T_2}. \tag{2.14}$$

The first term on the right handside of these equations describes how $\boldsymbol{H}_0$ and $\boldsymbol{H}_1$ affect the nuclear magnetization evolution in time. The second terms on the right handside of equations 2.13 and 2.14 account for a longitudinal relaxation mechanism and a transverse relaxation mechanism respectively. Both decays are assumed to be exponential in time. The time constant $T_1$ characterizes the spin-lattice longitudinal relaxation while the decay time $T_2$ describes the spin-spin transverse relaxation process.

[2] The perturbing field is:

$$\begin{aligned}\boldsymbol{H}_1 &= 2H_1\cos(\omega t)\hat{\boldsymbol{x}} \\ &= [H_1\cos(\omega t)\hat{\boldsymbol{x}} + H_1\sin(\omega t)\hat{\boldsymbol{y}}] + [H_1\cos(\omega t)\hat{\boldsymbol{x}} - H_1\sin(\omega t)\hat{\boldsymbol{y}}].\end{aligned}$$

.

[3] This holds when the rotating fame frequency $\omega$ is close to the resonance frequency $\omega_0$.

The in-plane components of the nuclear magnetization oscillating in phase and out of phase by $\frac{\pi}{2}$ with the radiofrequency field $\boldsymbol{H}_1$ yield the real and the imaginary part of the nuclear spin susceptibility:

$$\chi = \chi' - i\chi''. \tag{2.15}$$

The dispersion curve $\chi'(\omega)$ and the absorption curve $\chi''(\omega)$ are shown in figure 2.3, assuming $H_1 \ll H_0$.

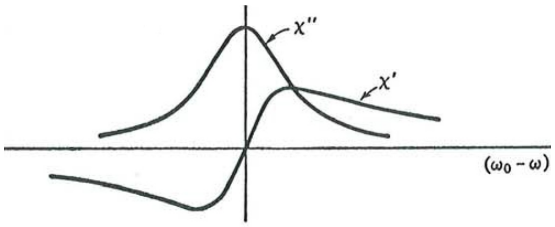


Figure 2.3: Real ($\chi'(\omega)$) and imaginary ($\chi''(\omega)$) part of the dynamical nuclear spin susceptibility [11] corresponding to the dispersion and absorption curves respectively. These results are obtained assuming $H_1 \ll H_0$.

## 2.3 Relaxation mechanisms

A simple classical explanation of the mechanisms producing the relaxation processes described by the time constants $T_1$ and $T_2$ in equations 2.13 and 2.14 can be derived as follows [10]. Let us assume that the nuclear magnetization $\boldsymbol{M}$ has been perturbed to a position far from equilibrium. $\boldsymbol{M}$ is still stationary in the rotating frame $S'$:

$$\boldsymbol{M} = M_{x'}\hat{\boldsymbol{x}}' + M_{y'}\hat{\boldsymbol{y}}' + M_{z'}\hat{\boldsymbol{z}}'.$$

Let us consider the effect of a microscopic field $\boldsymbol{h}$:

$$\boldsymbol{h} = h_{x'}\hat{\boldsymbol{x}}' + h_{y'}\hat{\boldsymbol{y}}' + h_{z'}\hat{\boldsymbol{z}}'. \tag{2.16}$$

Equation 2.16 describes the Fourier component of the microscopic field that is static in the rotating frame. The in-plane components of this field are therefore fluctuating at the resonance fequency in the laboratory frame.

The motion of $\boldsymbol{M}$ in the rotating is thus given by:

$$\begin{aligned}(-\frac{1}{\gamma}\frac{d\boldsymbol{M}}{dt})_{\text{Rot}} &= (\boldsymbol{h}\times\boldsymbol{M})_{\text{Rot}} \\ &= (h_{x'}\hat{\boldsymbol{x}}' + h_{y'}\hat{\boldsymbol{y}}' + h_{z'}\hat{\boldsymbol{z}}') \times (M_{x'}\hat{\boldsymbol{x}}' + M_{y'}\hat{\boldsymbol{y}}' + M_{z'}\hat{\boldsymbol{z}}') \\ &= (h_{y'}M_{z'} - h_{z'}M_{y'})\hat{\boldsymbol{x}}' + (h_{z'}M_{x'} - h_{x'}M_{z'})\hat{\boldsymbol{y}}' + (h_{x'}M_{y'} - h_{y'}M_{x'})\hat{\boldsymbol{z}}'.\end{aligned} \tag{2.17}$$

Equation 2.17 shows that transverse relaxation is driven by $h_{x'}$, $h_{y'}$ and $h_{z'}$. This means that $T_2$ relaxation processes are due to the in-plane microscopic field components oscillating at the resonance frequency in the laboratory frame and to a static microscopic field component along the $z$ axis. On the other hand only $h_{x'}$ and $h_{y'}$ affect the longitudinal relaxation. In other words $T_1$ relaxation processes are driven by the in-plane microscopic field components fluctuating at the resonance frequency in the laboratory frame.

From a quantum mechanical perspective, the recovery of the longitidinal magnetization to its equilibrium value modifies the population factors of the Zeeman levels depicted in figure 2.1. Thus $T_1$ relaxation processes involve an exchange of energy between the nuclear spin system and the lattice. By contrast, $T_2$ relaxation processes correspond to energy conserving mutual spin flips and do not involve any spin-lattice energy exchange.

## 2.4 Continuous wave and pulse techniques

### 2.4.1 CW NMR

In the continuous wave experiment, the radiofrequency $\omega$ is swept through the resonance value $\omega_0$. When the sample is placed in the transmitter coil, the inductance $L_0$ changes to the new value [11], [15]:

$$L_0 \rightarrow L_0[1 + 4\pi\chi(\omega)]. \tag{2.18}$$

Equation 2.15 and the well known expression of the coil impedance $Z = -i\omega L$ yield:

$$\Delta R = 4\pi L_0 \omega \chi''$$

where $\Delta R$ is the change of the coil resistance. The corresponding power absorbed by the nuclei $P(\omega)$ is thus proportional to $\chi''(\omega)$:

$$P(\omega) \propto \chi''(\omega). \tag{2.19}$$

It can be shown [15] that:

$$\chi''(\omega) \propto f(\omega) \tag{2.20}$$

where $f(\omega)d\omega$ is the fraction of nuclei with a resonance frequency between $\omega$ and $\omega + d\omega$ namely the NMR spectrum.

### 2.4.2 Pulse NMR

As discussed in section 2.2.1, equation 2.12 holds when the static field $H_0\hat{\boldsymbol{z}}$ is perturbed by a radiofrequency field $H_1\hat{\boldsymbol{x}}'$ satisfying the resonance condition 2.11. The nuclear magnetization $\boldsymbol{M}$ thus precesses about the $x'$ axis in the rotating frame at a frequency $\omega_1 = \gamma H_1$. It is therefore possible to rotate the magnetization $\boldsymbol{M}$ about the $x'$ axis by an angle $\theta$ by applying a resonance frequency pulse whose length $\tau_{\mathrm{P}}$ is given by the following equation:

$$\theta = \gamma H_1 \tau_{\mathrm{P}}. \tag{2.21}$$

If $H_1$ and $\tau_{\mathrm{P}}$ are chosen so that $\theta = \frac{\pi}{2}$, the pulse yields a nuclear magnetization lying in the $xy$ plane.

As the radiofrequency pulse is turned off a free induction decay (FID) of the transverse components of the magnetization is observed. According to the Bloch equation 2.14, exponential transverse relaxation occurs with a decay time $T_2$. Following the pulse the in-plane component of the nuclear magnetization precesses about the $z$ axis in the laboratory frame at the angular frequency $\gamma H_0$. This precessional motion produces an alternating magnetic flux through the coil and the induced e.m.f. is observed.

The signal detected by the coil in the laboratory frame $S$ can be transformed into the free induction decay (FID) observed in the rotating frame $S'$ by mixing it with a reference signal oscillating at $\omega_0$ [4]. By multiplying these two signals one obtains a high frequency signal that is not detected and a low frequency signal representing the FID.

**Hahn Echo**

As stated earlier in this section, a $\frac{\pi}{2}$-pulse is followed by the free induction decay of the transverse components of the nuclear magnetization characterized by a time constant $T_2$. Let us assume that the static magnetic field $\boldsymbol{H}_0$ is affected by a spatial inhomogeneity $\Delta H$. The in-plane components of the magnetization in different regions of the sample therefore precess at different frequencies as they experience slightly different magnetic fields. Thus the decay time of the transverse magnetization is affected by the spread of the precession frequency as follows:

$$\frac{1}{T_2^*} = \frac{1}{T_2} + \gamma \Delta H. \tag{2.22}$$

The decay time of the FID signal is therefore $T_2^*$.

It is possible to estimate the value of the time constant $T_2$ by resorting to the spin-echo technique. Figure 2.4 shows the sequence of pulses of a typical Hahn spin-echo experiment. The Hann sequence

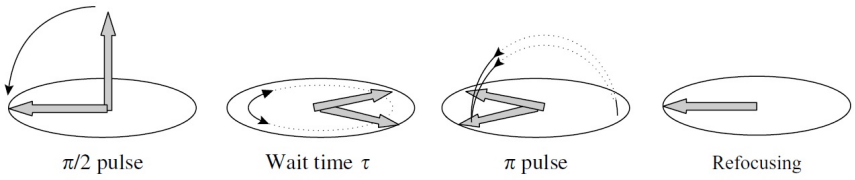


Figure 2.4: Sequence of pulses involved in the Hahn spin-echo technique [14].

can be schematized as follows:

$$\frac{\pi}{2} - \tau - \pi - \tau - \text{ECHO}.$$

This sequence is repeated changing the delay time $\tau$. The echo amplitude decays with increasing $\tau$ with a time constant $T_2$ [5].

### 2.4.3 Relationship between CW and pulse techniques

As discussed in section 2.4.1, the following proportionality relation holds:

$$\text{CW experiment} \;\rightarrow\; P(\omega) \;\propto\; \chi''(\omega) \;\propto\; f(\omega) \;\rightarrow\; \text{NMR spectrum}. \tag{2.23}$$

On the other hand, the fluctuation-dissipation theorem provides the following relationship [15]:

$$\chi''(\omega) \;\propto\; \int_0^\infty e^{i\omega t} \overline{\langle M_x(t) M_x(0) \rangle}\, dt. \tag{2.24}$$

[4] $M_{xy}(t)\cos(\omega t) \times \cos(\omega_0 t) \propto M_{xy}(0) e^{-t/T_2} \{\cos[(\omega_0 - \omega)t)] + \cos[(\omega_0 + \omega)t)]$.
When perfect resonance is achieved the free precession frequency $\omega$ equals the reference frequency $\omega_0$.

[5] It is actually possible to get rid of the field inhomogeneity effect and determine the $T_2$ value by using this simple method only when the motions of the molecules in the sample can be desregarded.

The NMR spectrum, directly proportional to the imaginary part of the susceptibility $\chi''(\omega)$, can therefore be derived by Fourier transforming the correlation function of the transverse components of the nuclear magnetization. This correlation function $\langle\overline{M_x(t)M_x(0)}\rangle$ is proportional to the FID signal measured in a pulse experiment.

## 2.5 Nuclear Hamiltonian and hyperfine interactions

The aim of this section is to provide a general expression of the Hamiltonian of a system of nuclear magnetic moments considering both the action of an external magnetic field and the most important sources of internal fields. Among these, we discuss in detail the hyperfine interaction term. In the present work we are particularly concerned with the hyperfine field produced by the $Cr^{3+}$ electronic magnetic moment at the ion's own nuclear site (direct interaction) and at the nearby $^{19}F$ nuclear sites (transferred interaction) in AFM rings.

### 2.5.1 General expression of the nuclear Hamiltonian

A rather general form of the nuclear Hamiltonian that accounts for all the interactions acting on the nuclei is [15]:

$$\mathcal{H} = \mathcal{H}_{\mathrm{Z}} + \mathcal{H}_{\mathrm{n-n}} + \mathcal{H}_{\mathrm{n-e}} + \mathcal{H}_{\mathrm{EFG}}. \tag{2.25}$$

In this formula the first term is the Zeeman coupling between the nuclei and the applied magnetic field $\boldsymbol{H}_0$.

The second term describes the classical nucleus-nucleus dipolar interaction. The formal expression of the dipolar coupling between the nuclear magnetic moments is:

$$\mathcal{H}_{\mathrm{D}} = \frac{1}{2}\sum_j\sum_k\Big[\frac{\boldsymbol{\mu}_j\cdot\boldsymbol{\mu}_k}{r_{jk}^3} - \frac{3(\boldsymbol{\mu}_j\cdot\boldsymbol{r}_{jk})(\boldsymbol{\mu}_k\cdot\boldsymbol{r}_{jk})}{r_{jk}^5}\Big] \tag{2.26}$$

where the nuclear moments are $\boldsymbol{\mu}_j = \gamma_j\hbar\boldsymbol{I}_j$.

It is possible to estimate the order of magnitude of the local field due to the nucleus-nucleus dipolar interaction as follows [11]:

$$H_{\mathrm{Loc}} \sim \frac{\mu}{r^3} \sim 1 \div 10 \text{ Gauss}$$

where $r$ is the distance between nearest neighbors nuclei (we assume $r \sim 2 \div 1$ Å) and $\mu$ is the nuclear magneton i. e. $\mu_{\mathrm{N}} = 0,5\cdot 10^{-23}$ erg Gauss$^{-1}$. This field may either add or be opposite to the applied field $\boldsymbol{H}_0$. This results in a spread of the resonance condition over a range of $\sim 1 \div 10$ Gauss. The evaluation of the line shape and the line width in presence of nuclear dipolar interaction is based on the theory of the second and higher moments developed mostly by Van Vleck [12]. We limit ourselves to recall that the contribution to the second moment and consequently to the line width is different for like moments and unlike moments. In fact in the case of unlike moments the nuclear dipolar contribution is smaller since only the secular terms of the nuclear dipolar Hamiltonian do contribute. The secular terms can be viewed as a local magnetic field generated at a given nuclear site by the sorrounding nuclei [12]. Since the effect of this interaction is small and it affects only the width of the NMR lines it will be desregarded in the following.

The third term describes the hyperfine interaction, namely the coupling between the nuclear magnetic moment and the electronic magnetic moments. This term is the subject of sections 2.5.2 and 2.5.3.

The fourth term accounts for the interaction between the nuclear quadrupole moment (non-zero if $I > 1/2$) and the electric field gradient due to a non spherical charge distribution sorrounding the nucleus. In the present work this term will not be considered since we are dealing mostly with $^{19}$F nucleus with spin $I = 1/2$ and in the $^{53}$Cr-NMR measurements ($I = 3/2$) the quadrupole interactions are small compared to the magnetic ones.

### 2.5.2 Classical nucleus-electron dipolar interaction

The third term on the right handside of equation 2.25 accounts for the hyperfine interaction namely the coupling between the nuclear magnetic moment $\boldsymbol{\mu}_{\mathrm{n}} = \gamma_{\mathrm{n}}\hbar\boldsymbol{I} = g_{\mathrm{n}}\boldsymbol{\mu}_{\mathrm{N}}$ and the electronic magnetic moment $\boldsymbol{\mu}_{\mathrm{e}} = -\gamma_{\mathrm{e}}\hbar\boldsymbol{S} = -g\mu_{\mathrm{B}}\boldsymbol{S}$. In these expressions $g_{\mathrm{n}}$ is the nuclear Landé factor, $\boldsymbol{\mu}_{\mathrm{N}}$ is the nuclear magneton, $g$ is the electronic Landé factor and $\mu_{\mathrm{B}}$ is the Bohr magneton.

The contribution to the hyperfine field at the nucleus due to the electrons belonging to far away magnetic ions can be derived by means of the classical expression of the magnetic dipolar interaction [11]. This coupling is evaluated within the point dipole approximation assuming that the electronic moment is located at the nuclear position of the ion it belongs to:

$$\frac{\boldsymbol{\mu}_{\mathrm{e}} \cdot \boldsymbol{\mu}_{\mathrm{n}}}{r^3} - \frac{3(\boldsymbol{\mu}_{\mathrm{e}} \cdot \boldsymbol{r})(\boldsymbol{\mu}_{\mathrm{n}} \cdot \boldsymbol{r})}{r^5} \tag{2.27}$$

where $\boldsymbol{r}$ is the distance between the moments. This equation is analogous to equation 2.26 describing the classical dipolar interaction between the nuclei.

Since the two dipole moments are different, only the secular terms of the dipolar Hamiltonian contribute, analogous to the case of unlike nuclear moments discussed in section 2.5.1. This interaction can therefore be described as a local magnetic field generated at the nuclear site by the thermal average of the electronic moment $\langle\mu_{\mathrm{e}}\rangle$ i. e.:

$$H_{\mathrm{Loc}} = \langle\mu_{\mathrm{e}}\rangle \frac{1 - 3\cos^2\theta}{r^3} \tag{2.28}$$

where $\theta$ is the angle between the vector $\boldsymbol{r}$ and the quantization axis along the external magnetic field [6].

### 2.5.3 Direct and transferred hyperfine interactions

If the nuclear and electronic magnetic moments are close to each other, namely they belong to the same atom or to different atoms whose electronic wavefunctions have a non-zero overlap, the point dipole approximation doesn't hold. The hyperfine interaction term must therefore be averaged over the electronic wavefunction. This hyperfine term is named *direct hyperfine interaction* in the case of magnetic moments belonging to the same atom and *transferred hyperfine interaction* in the case of magnetic moments belonging to different atoms.

[6] In the paramagnetic case the electronic magnetic moment $\boldsymbol{\mu}_{\mathrm{e}}$ is directed along the applied field. If the electronic system is not paramagnetic, the angle between the vector $\boldsymbol{r}$ and $\boldsymbol{\mu}_{\mathrm{e}}$ must be considered according to equation 2.27.

Let us consider the nuclear Hamiltonian 2.25 and let us assume that the nuclear dipolar term 2.26, the hyperfine dipolar coupling 2.27 and the quadrupole interaction term can be desregarded. We obtain the following expression:

$$\mathcal{H} = -\gamma_{\rm n}\hbar \sum_{i}^{x,y,z} I_i H_i + \sum_{i}^{x,y,z}\sum_{j=1}^{N} A_i^j I_i \langle S_i\rangle^j. \tag{2.29}$$

The first term on the right handside describes the Zeeman interaction between the nuclear magnetic moment and the external field components $(H_x, H_y, H_z)$ while the second term accounts for the hyperfine field due to the nearby electronic magnetic moments labeled by the index $j = 1, ..., N$. $A_i^j$ is the hyperfine constant describing the interaction between the nuclear spin and the $j^{\rm th}$ electronic moment along the $i$ axis. $\langle S_i\rangle^j$ is the thermal average in the $i^{\rm th}$ direction of the $j^{\rm th}$ electronic spin. A few examples of common expressions for this expectation value of are given in the following.

If the electronic spin system is in the paramagnetic state the expectation value $\langle S_i\rangle$ is [7]:

$$\langle S_i\rangle = -\frac{\chi H_i}{N g \mu_{\rm B}}$$

where $\chi$ is the static and uniform magnetic electronic susceptibility. Viceversa in the antiferromagnetic phase and zero applied field the following expression holds:

$$\langle S(T)\rangle \propto S\,\frac{M(T)}{M(0)}$$

where $S$ is the electronic spin value and $M(T)$ is the sublattice magnetization at the temperature $T$. In the molecular field theory $\frac{M(T)}{M(0)}$ is the normalized Brillouin function: its value is unity at $T = 0$ K and approaches zero at the transition temperature $T_{\rm N}$.

We consider now the explicit expression assumed by the hyperfine constant $A$ in equation 2.29 in different cases. Examples of the hyperfine interactions are illustrated referring to the $^{53}$Cr and $^{19}$F atoms since these are the nuclei studied in the experimental section of this work.

Let us examine first the hyperfine field produced at the nuclear site by the atom's own electrons, that is the *direct hyperfine interaction*. The coupling constant of an electron described by the atomic wavefunction $\psi$ is [8,9]:

$$A_\psi = \frac{2}{5} g\mu_{\rm B}\gamma_{\rm n}\hbar\langle\frac{1}{\boldsymbol{r}^3}\rangle_\psi \tag{2.30}$$

where $\langle\frac{1}{\boldsymbol{r}^3}\rangle_\psi$ is the expectation value of the operator $\frac{1}{\boldsymbol{r}^3}$ in the electronic state $\psi$.

It is worthwhile stressing that equation 2.30 doesn't hold for $s$ electronic wavefunctions. In fact the non-zero probability of finding the electron at the nuclear position $\boldsymbol{r} = 0$ gives rise to a diverging expectation value $\langle\frac{1}{\boldsymbol{r}^3}\rangle$. This difficulty has been overcome by E. Fermi [25] by a renormalization procedure leading to the following expression for the direct *contact* hyperfine constant:

$$A_s = \frac{8}{3}\pi g\mu_{\rm B}\gamma_{\rm n}\hbar|\psi(0)|_s^2 \tag{2.31}$$

where $|\psi(0)|_s^2$ is the normalized probability of finding an $s$ electron at the nucleus.

[7] The assumption of no magnetic anisotropy has been made.

[8] This coupling constant is expressed in erg in both equation 2.29 and 2.30.

[9] In equation 2.30 the factor 2/5 is characteristic of $p$-type wavefunctions. This equation doesn't include any anisotropic term due to the fact that an average over the wavefunctions $p_x$, $p_y$ and $p_z$ has been performed.

The expressions 2.30 and 2.31 can be utilized to calculate the direct hyperfine field at the nucleus of a magnetic ion as is the case of the field at the $^{53}$Cr nuclear site in the $Cr^{3+}$ ion whose electronic configuration is: $[Cr^{3+}] = [Ar]3d^3$. Since in the $Cr^{3+}$ ion the magnetic electrons are described by $3d$ wavefunctions the term $\frac{1}{r^3}$ in equation 2.30 must be averaged over the $3d$ electronic functions yielding a non zero value. On the other hand equation 2.31 yields zero for the $3d$ functions. However the $3d$ magnetic electrons can polarize the $3s$ wavefunctions of the core electrons that would otherwise be paired yielding a zero spin moment. This spin polarization effect results in a large hyperfine contact field named "core polarization" [19], [20]. This dominanant contribution adds to the smaller term from equation 2.30.

The calculation of the core polarization hyperfine field has been done for most $3d$ ions but only approximate solutions can be found [19], [20]. A qualitative explanation of this effect is the following. The magnetic $3d$ electrons couple antiferromagnetically to the core $3s$ electrons. This results in a higher probability for the $3s$ electrons to be antiparallel to the $3d$ electrons. Consequently, equation 2.31 yields a very large and negative contact term. For a single unpaired $3d$ electron the core polarization hyperfine field has been theoretically estimated to be $A_{\rm cp} = -12,5$ Tesla [20] (see Appendix A.1). $Cr^{3+}$ core polarization field has been determined experimentally by means of NMR measurements in $Cr_7Cd$ [21]: the value $A_{\rm cp} = -12,38 \pm 0,23$ Tesla/Bohr magneton has been obtained. The core polarization field is opposite to the $3d$ electronic magnetic moment direction yielding a negative $A_{\rm cp}$ value. Further details about this experimental work [21] will be given in section 4.1.

We consider now the case of the hyperfine field at a nucleus that is *not* belonging to the magnetic ion. If the total electronic spin $S$ of the atom is zero, the direct hyperfine field vanishes (see equation 2.29). The local field at the nuclear site might therefore be determined by a dominant contribution from the *transferred hyperfine interaction*. This coupling occurs when the atom to which the nuclear species of interest belongs binds to a magnetic atom. The overlap between the electronic wavefunctions involved in the bond partially polarizes the formerly $S = 0$ electronic shells yielding a non-zero hperfine field at the nucleus.

For the sake of clarity, let us consider the fluoride anion $F^-$ whose electronic configuration is:

$$[F^-] = [He]2s^2 2p^6.$$

The hyperfine fields $H_{2p}(F^-)$ and $H_{2s}(F^-)$ vanish due to the closed shells value $S = 0$. However, if the $F^-$ ion binds to a magnetic ion $X^{z+}$, the fluoride electronic structure is polarized since the bonding is not purely ionic. This produces a non-zero $F^-$ electronic spin expectation value giving rise to a transferred hyperfine field at the $^{19}$F nuclear site.

It is possible to write the $i^{th}$ component of the transferred hyperfine constant in the general form [24]:

$$A_i = A_t + A_\sigma(3\cos^2\theta_{i,\sigma} - 1) + A_\pi(3\cos^2\theta_{i,\pi} - 1) \tag{2.32}$$

where $i = x, y, z$. $A_t$ accounts for the isotropic contribution due to the $s$-electron polarization. The anisotropic terms $A_\sigma(3\cos^2\theta_{i,\sigma} - 1)$ and $A_\pi(3\cos^2\theta_{i,\pi} - 1)$ describe the contribution due to $p_\sigma$ bonds and $p_\pi$ bonds. $A_\sigma$ is the transferred hyperfine constant relating to the $p_\sigma$ bonds while $\theta_{i,\sigma}$ is the angle between the directional $p_\sigma$ bonds and the $i$ axis. Analogous definitions hold for $A_\pi$ and $\theta_{i,\pi}$.

The isotropic hyperfine constant $A_t$ in equation 2.32 is of the form of equation 2.31. However, since the $s$ character of the bonding $F^-$ - $X^{z+}$ wavefunction is small the transferred hyperfine constant $A_t$ is

only a fraction of the one in the free $F^-$ ion $A_s$ given by equation 2.31 whose calculated value is given by equation A.3 in Appendix A. Thus the experimental determination of the transferred hyperfine constant $A_t$ allows one to measure the fraction of $s$ character of the bonding wavefunction. The same argument holds for the anisotropic transferred hyperfine constants $A_\sigma$ and $A_\pi$ which depend on the fraction of $p$ character in the bonding wavefunction.

The anisotropic contribution to the transferred hyperfine field is often much smaller than the isotropic term as pointed out by R. G. Shulman and K. Knox in their NMR study of the transferred hyperfine field at the $^{19}F$ nuclear site in $KMnF_3$ [16] and by R. G. Shulman and V. Jaccarino in their work on $MnF_2$ [17]. In these compounds the isotropic term turns out to be almost two orders of magnitude larger than the anisotropic transferred hyperfine field at the $^{19}F$ nucleus. For this reason the present study focuses on the isotropic contribution to the transferred hyperfine constant.

The interested reader can find further information abut the direct and transferred hyperfine constants in the $^{19}F$ atom as well as a brief description of the studies of the antiferromagnetic compounds $KMnF_3$ and $MnF_2$ carried on during the 1950's and 1960's by R. G. Shulman, V. Jaccarino, K. Knox and P. Heller in appendix A. The values of the hyperfine coupling contants and of the percentage of $s$ covalent character in the $^{19}F$ - $Mn^{2+}$ bonding determined by those works can be compared to the corresponding values relating to the $^{19}F$ - $Cr^{3+}$ bonding estimated in the present thesis.

## 2.6 Experimental details referring to our measurements

We give in this paragraph a brief description of the experimental set-up and of the experimental methods utilized in the present study.

### 2.6.1 NMR spectrometer

Two experimental set-ups have been utilized in the present work [10]. The main difference between the two equipments is the temperature range of operation. One set-up (set-up 1) includes a Helium bath cryostat and operates down to 1,5 K. The second apparatus (set-up 2) includes a $^3He$ - $^4He$ dilution refrigerator and can achieve temperatures as low as 50 mK. The two low temperature set-ups are shown in figure 2.6 (a) and 2.7 (b): the interested reader can find more information about the cooling systems in section 2.6.3.

The static magnetic field is generated in both instruments by a 9 Tesla high resolution superconducting magnet (Oxford Instruments). The superconducting magnet essentially consists of a Cu/Nb-Ti coil: Niobium-Titanium (Nb-Ti) is a superconducting alloy whose critical temperature is $\sim 9,2$ K while the Copper matrix is required to provide stability and protection to the wire and to the coil. The superconducting coil is thermally insulated by means of an outer chamber containig liquid Nitrogen and an inner chamber containing liquid Helium. The intensity of the magnetic field generated by the superconducting coil can be varied by changing the intensity of the electrical current circulating in the coil. This is achieved by warming up a small section of the superconducting wire by means of a heater. As the heated region is warmed up over the critical temperature a phase transition to the

[10] The experimental measurements that are part of the present work have been performed at Ames Laboratory, Department of Physics and Astronomy, Iowa State University, Ames, IA.

non-superconducting state occurs in the small heated region and electric contacts for current injection are produced.

The NMR specrometers are essentially the same in the two experimental set-ups. The components of the equipment forming the NMR spectrometers are shown in figure 2.5 and 2.7 (a). They include:

- AC power
- Frequency synthesizer: 10 - 500 MHz
- Pulse generator: produces radiofrequency pulses whose length is $\sim \mu$s
- Pulse amplifier: 10 - 500 MHz, generally 400 Watt
- Phase inverter
- Receiver: 10 - 500 MHz (Thamway company) and receiver attenuator (up to 70 dB)
- Oscilloscope, whose function is to display the real and the imaginary part of the received signal.

Figure 2.5 also shows:

- Pumping system connected to the bath cryostat
- Superconducting magnet power supply (Oxford IPS)
- Helium depth indicator: measures the resistivity change of a superconducting rod dipped in the Helium tank as the liquid Helium level varies
- Temperature controller: measures the sample space temperature by means of a Chromel-Au/Fe thermocouple
- Multimeters: measure the magnetic field value and the Helium tank temperature.

Figure 2.6 (c) and 2.7 (c) show the NMR probe in set-up 1 and in set-up 2 respectively. The NMR probe is essentially a $RLC$ resonant circuit whose function is to irradiate the sample with the required radiofrequency pulses and to collect the signal generated by the sample's magnetization. $R$ is the overall resistance of the circuit, $L$ is the inductance of the coil sorrounding the sample and $C$ is the capacitance of the circuit. This capacitance is due to the co-axial cable intrinsic capacitance and to additional capacitors that can be added with the purpose of tuning the probe at the Larmor frequency. The NMR probe main features are the following. The NMR probe resonance frequency is $1/\sqrt{LC}$ and must have the proper value for the NMR experiment. Impedance matching between the output amplifier and the probe (50 $\Omega$) is required in order to reduce the reflected wave amplitude. A high $Q$-factor, where $Q = R\sqrt{\frac{C}{L}}$ is required in order to maximize the power reaching the coil and the signal to noise ratio [10]. However very high $Q$- factors can produce discharges and noise enhancement related to mechanical vibrations (ringing). The NMR coil shape is usually adapted to the sample's shape: in fact the signal to noise ratio is proportional to the filling factor, namely the fraction of the volume of the coil that is occupied by the sample [10].

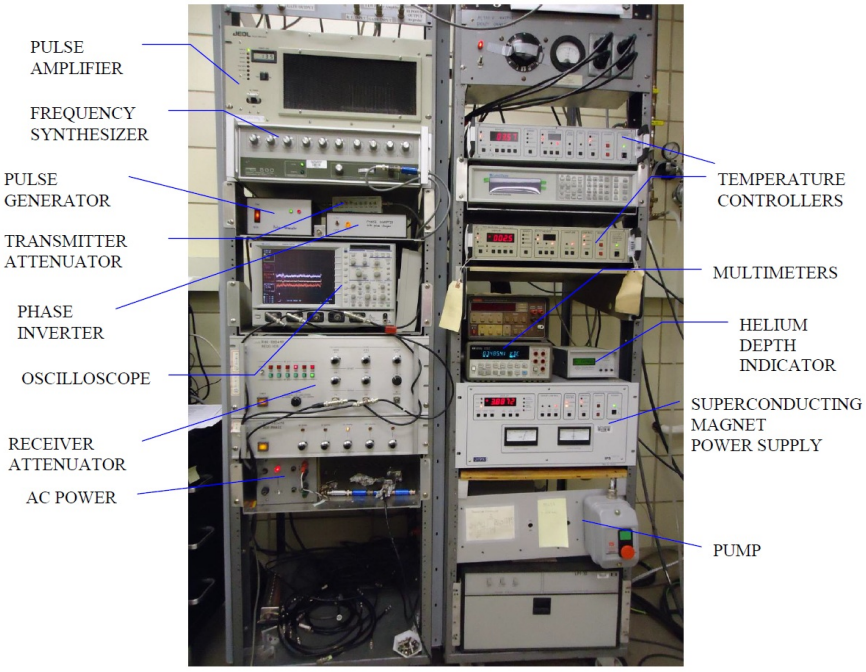


Figure 2.5: 9 Tesla superconducting magnet NMR station, part of set-up 1.

### 2.6.2 Experimental methods

From the discussion developed in section 2.4.3 it follows that NMR spectra can be collected by using the FT method. The basic principles of this technique are briefly explained in the following. Both the radiofrequency and the applied field are kept fixed. The FT of the second half of the time domain echo signal that follows a $\frac{\pi}{2} - \pi$ sequence yields the NMR spectrum. This last statement is true if the whole line can be irradiated by a single pulse [11].

In the experimental part of the present work only a few spectra have been collected by using the FT method. Since most spectra are broad and structured the whole NMR line could not be irradiated by means of a single RF pulse and we resorted to the following ingenious method.

The radiofrequency $\nu_0 = \frac{\omega_0}{2\pi}$ is kept fixed while the applied field is swept over a range including the bare resonance Larmor value given by equation 2.9:

$$H_0 = \frac{2\pi}{\gamma}\nu_0.$$

The spectrum $y$-value is given (at any field value) by the integral of the spin-echo signal that follows the Hahn sequence of pulses:

$$\frac{\pi}{2} - \tau - \pi - \tau - \text{ECHO}$$

described in section 2.4.2. Of course the spin-echo intensity is affected by the $T_2$ value that may change as the field is being swept. The comparison between the signal intensity of different spectral regions might therefore be invalidated by this $T_2$ change.

It is worthwhile mentioning some experimental details of this data collection procedure that are relevant to the spectral resolution. As already stated, the spectra have been measured by sweeping

[11] The pulse length $\tau_P$ should be so short that the frequency range $\tau_P^{-1}$ includes the whole spectral line.

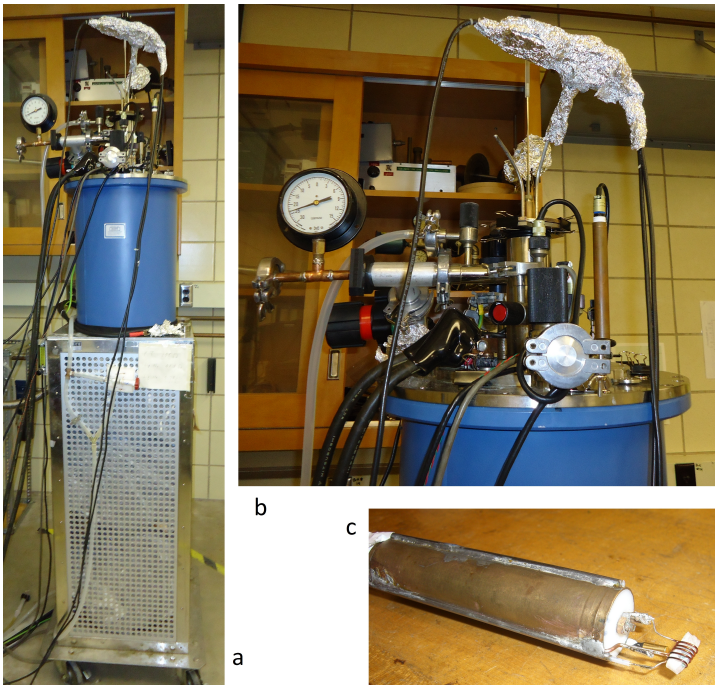


Figure 2.6: Set-up 1: bath cryostat (a), (b) and NMR probe (c).

the magnetic field: this sweep is operated in a continuous way by injecting an electrical current in the superconducting magnet through high temperature contacts. Pulse sequences are repeated over and over during the sweep with a delay time named repetition time $t_{\mathrm{Rep}}$. Every spectral point is the average value of a set number $N_{\mathrm{Avg}}$ of acquisitions. We stress that each acquisition corresponds to a pulse sequence and sequences are repeated with a delay equal to the repetition time. Thus each point determination takes $t_{\mathrm{Rep}} \cdot N_{\mathrm{Avg}}$ seconds. The sets of $N_{\mathrm{Avg}}$ acquisitions relating to two successive spectral points differ only by one value. It is required that the magnetic field change during one point determination is small compared to the width of the spectral structures of interest. Otherwise these features are not resolved.

For the sake of illustration typical values of the experimental parameters are given in the following. Most $^{19}$F-NMR spectra of $Cr_7Ni$ have been collected by using $t_{\mathrm{Rep}} = 0,2$ s, $N_{\mathrm{Avg}} = 4$ and a field sweep rate of 0,1 Tesla/min. The field change during one point determination turns out to be $\sim 10^{-3}$ Tesla, to be compared to the spectral structures FWHM $\sim$ 0,05 Tesla. $^{53}$Cr-NMR spectra of $Cr_7Ni$ have been measured by using $t_{\mathrm{Rep}} = 0,1$ s, $N_{\mathrm{Avg}} = 64$ and a field sweep rate of 0,2 Tesla/min. During one point determination the magnetic field varies by 0,02 Tesla, a suitable value compared to $\sim$ 1 Tesla broad NMR line. Both the FT method and a very slow field sweep acquisition have been adopted in order to collect the $Cr_8$ sharp singlet spectral line at very low magnetic fields. The experimental values of the latter method are $t_{\mathrm{Rep}} = 0,5$ s, $N_{\mathrm{Avg}} = 16$ and a field sweep rate of 0,001 Tesla/min. The field change during one point determination turns out to be $\sim 10^{-4}$ Tesla: the same order of magnitude of the peak's FWHM.

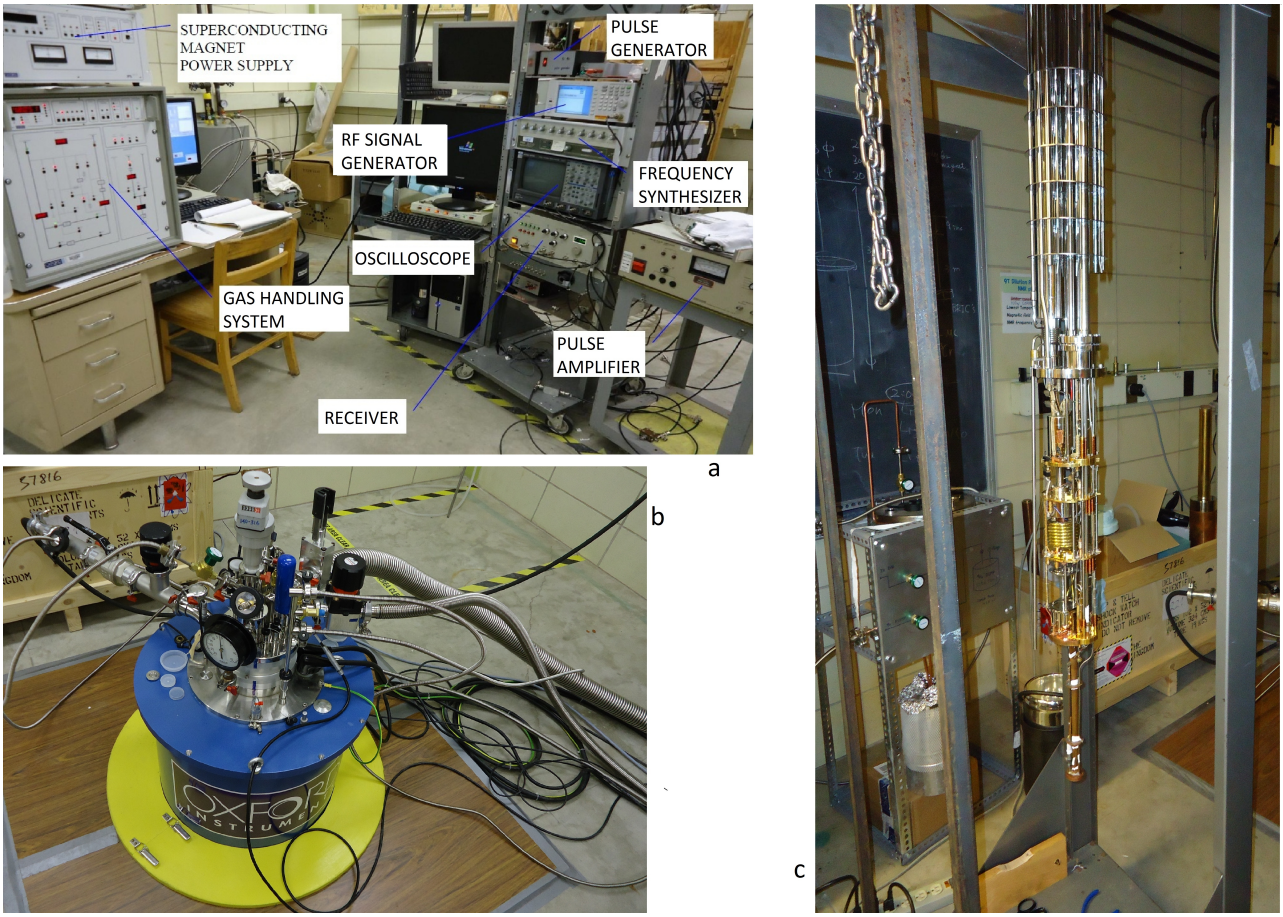


Figure 2.7: Set-up 2: NMR spectrometer and dilution refrigerator gas handling front panel (a), dilution refrigerator (b), dilution refrigerator NMR probe (c).

### 2.6.3 Low temperature apparatus

The NMR measurements reported in the experimental section of the present work have been performed at very low temperatures: 1,6 K (set-up 1) and 100 mK (set-up 2). Low temperatures are required in order to study the sample's ground state, whose population depends on the temperature according to the Boltzmann factor. As pointed out in the recent article by H. Amiri *et al.* [26] the magnetic behaviour of AFM rings changes dramatically by increasing the temperature above the AFM coupling constant value $J/k_B \sim 30 \div 40$K. The low temperature correlated spin dynamic turns into a high temperature paramagnetic behaviour characterized by magnetic ions' local spins fluctuating almost independently from each other. Low temperatures are therefore required in order to probe the collective behaviour of the ground state spin system, that is the purpose of the present thesis.

The NMR spectra presented in this thesis have been collected at 1,6 K. This temperature has been achieved by using the bath cryostat shown in figure 2.6 (a), (b) and and the pumping system in figure 2.5. The liquid Helium temperature at atmospheric pressure is 4,2 K. Lower temperatures can be obtained by pumping the He vapour away from the liquid surface in the He bath. The lowest temperature achieved by this technique is approximatively 1,5 K.

Measurements at temperatures as low as 100 mK have been performed by using a KelvinoxIGH

dilution refrigerator (Oxford Instruments)[12]. The temperature is measured by means of a resistance thermometer constituted by a $RuO_2$ chip sensor. Careful calibration of this sensor has been performed in the temperature range 40 mK - 4,2 K. In this temperature interval the resistance curve is decreasing with increasing temperature. A schematic diagram of the Kelvinox dilution cryostat is sketched in figure 2.8 and some pictures of the experimental apparatus are shown in figure 2.7.

The principle of operation of the dilution cryostat was first proposed by H. London in 1951 but the first working instruments were built and commercialized only in the 1960's. Since then the performances of these systems have improved and better understanding of the underlying physical processes has been achieved. Such principles of operation are briefly described in the following [27].

When a mixture of the two Helium isotopes is cooled below the critical temperature of 0,86 K (tri-critical point) phase separation occurs. The mixture separates into a lighter $^3$He-rich phase, named 'concentrated phase' (dark blue color in figure 2.8) and a heavier $^3$He-poor phase, named 'dilute phase' (light blue color in figure 2.8). The percentage of $^3$He in this latter $^4$He-rich phase is about $6 \div 7\,\%$. The enthalpy of $^3$He in the two phases is different: it is therefore possible to obtain cooling by *evaporating* the $^3$He from the $^3$He-rich (concentrated) phase into the $^3$He-poor (dilute) phase.

The properties of the two phases are derived by means of a quantum mechanical treatment. It turns out that the concentrated phase of the mixture can be regarded as 'liquid $^3$He' and the dilute phase as '$^3$He gas'. In the dilute $^3$He-poor phase, the $^3$He gas moves through the inert $^4$He liquid without interacting. This gas is formed at the phase boundary in the mixing chamber in a process analogous to the evaporation at a liquid surface. The cooling obtained by this is used to cool the sample down.

When the refrigerator is started the $^3$He -$^4$He mixture is cooled down to approximately 1,2 K and condensed by means of the 1 K pot. Phase separation is achieved by reducing the vapour pressure of the liquid in the *still* using the external pumping system so that the temperature is reduced to below the tri-critical point.

In a continuously operating system the $^3$He must be extracted from the dilute phase in order to prevent it from saturating and must be returned to the concentrated phase. The $^3$He is pumped away from the liquid surface in the *still*, typically mantained at a temperature of $0,6 \div 0,7$ K. At this temperature $^3$He evaporates preferentially as its vapour pressure is about 1000 times higher than that of $^4$He.

The concentration of the $^3$He in the dilute phase in the *still* is therefore lower than it is in the mixing chamber producing an osmotic pressure difference that drives an $^3$He flow to the still. The room temperature pumping system is used to remove the $^3$He from the still. The gas is then passed through filters and cold traps and returned to the cryostat, where it is pre-cooled in the main Helium bath and condensed on the 1 K pot.

The KelvinoxIGH gas handling system allows circulation and safe handling of the $^3$He -$^4$He mixture and auxiliary pumping operations. It can be operated manually from the front panel shown in figure 2.7 (a).

[12]The lowest temperature that this instrument can reach is actually 50 mK but the superconducting magnet field sweep and the RF pulses applied to the sample produce a small temperature increase.

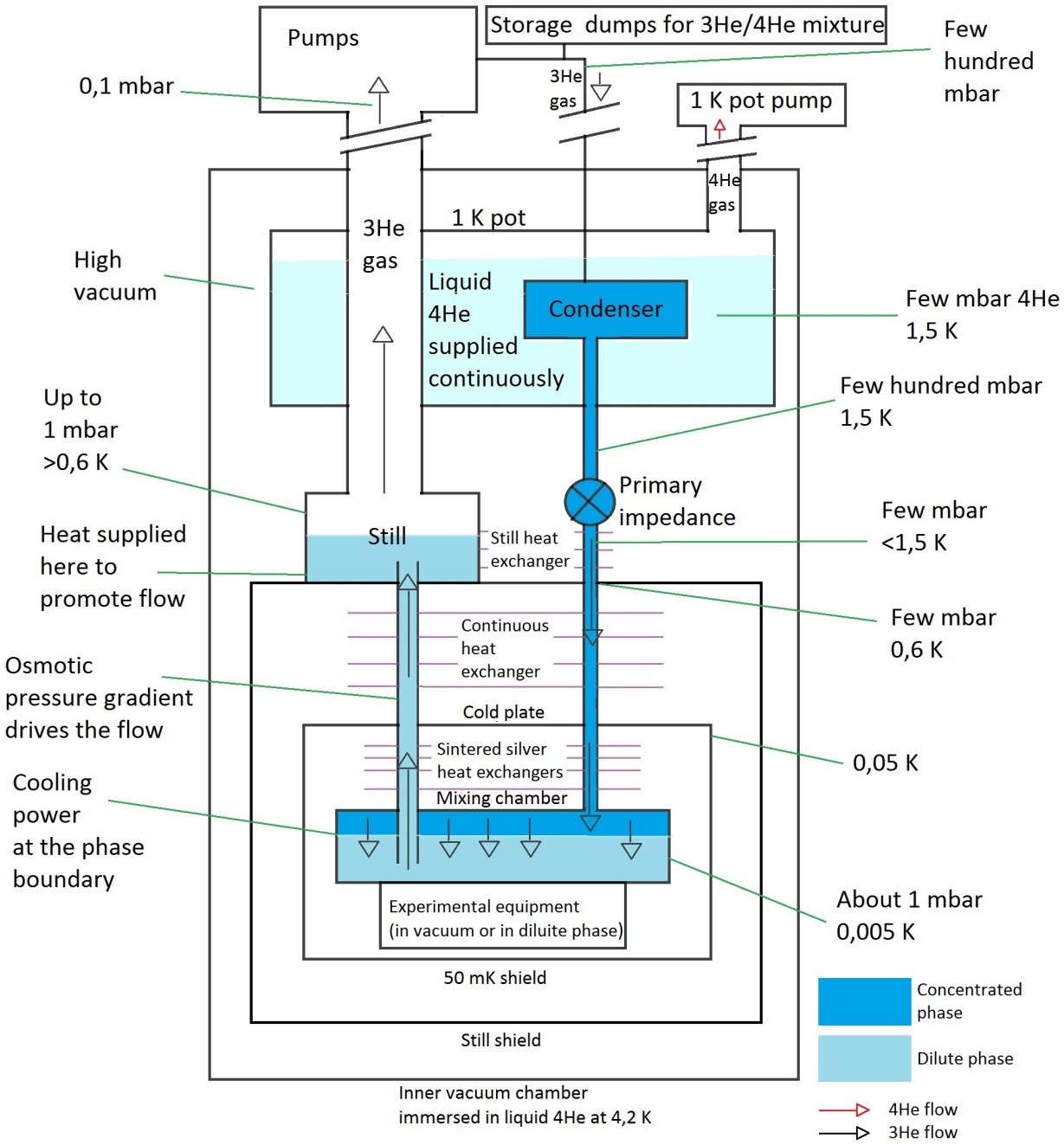


Figure 2.8: Schematic diagram of a KelvinoxIGH dilution refrigerator (Oxford Instruments) [27]

# Chapter 3

# $Cr_8$

As part of the present work, $^{19}$F-NMR measurements have been performed at Ames Laboratory [1] on $Cr_8$ single crystals. NMR spectra have been collected at $T \sim 1,6$ K by means of the experimental equipment labeled "set-up 1" in section 2.6. The crystal orientation has been determined by means of a microscope and by using schematic sketches such as the one shown in figure 3.1, representing the orientation of the crystallographic axes with respect to the crystal's macroscopic shape. As observed in section 1.2.1, the $a$-axis is perpendicular to the molecular ring.

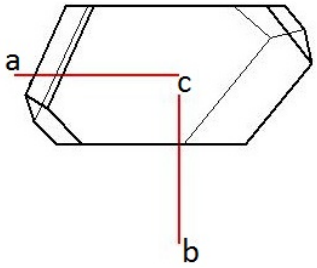


Figure 3.1: Orientation of the crystalligraphic axes with respect to the macroscopic crystal shape in $Cr_8$.

This chapter describes the present's work $^{19}$F-NMR experiments on $Cr_8$ single crystals. The first section illustrates the ground state measurements reproducing the previous experiments by E. Micotti *et al.* (2006) [7] and in complete agreement with the results summarized in paragraph 1.2.1. The second section deals with the excited state spectra, leading to open questions concerning the nature of the mixing of magnetic states in $Cr_8$.

## 3.1 Ground state NMR measurements

Ground state spectra can be measured in $Cr_8$ only at Larmor fields much lower than the level crossing field of $\sim 7$ Tesla due to the finite temperature of operation. It has been observed in section 1.2.1 with reference to figure 1.4 that as the applied field approaches the level crossing threshold the energy separation between the ground state $|0,0\rangle$ and the excited state $|1,-1\rangle$ decreases so that this latter

[1] Department of Physics and Astronomy, Ames Laboratory, Iowa State University, Ames, IA.

state is more easily thermally populated. Very low magnetic fields are therefore required at non-zero temperature in order to have a negligible excited state population.

In the present work ground state spectra have been measured at $T = 1,6$ K with external magnetic fields of 1,87 Tesla and 2,34 Tesla applied along the $a$-axis. Figure 3.2 shows the spectra collected by means of the field-sweep method. As the NMR line is narrow, also the FT technique described in section 2.6.2 could be employed. Figure 3.3 shows the real and the imaginary part of the FT of the second half of the echo signal yielding the absorption and dispersion frequency domain curves respectively.

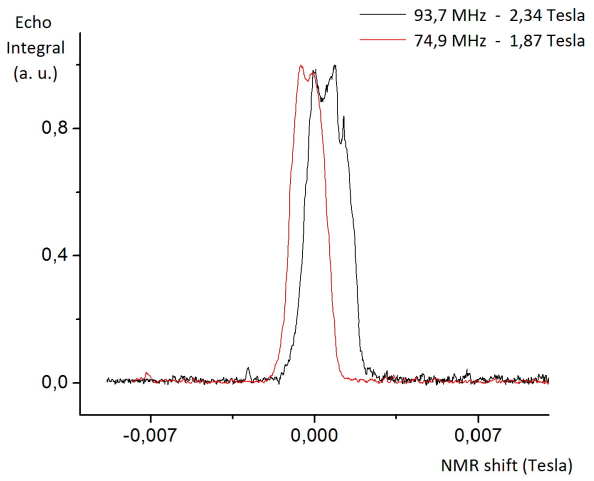


Figure 3.2: $^{19}$F-NMR spectra of $Cr_8$ single crystal at $T = 1,6$ K showing the singlet ground state at low applied magnetic fields. The applied field $H$ is perpendicular to the molecular ring and parallel to the $a$-crystallographic axis.

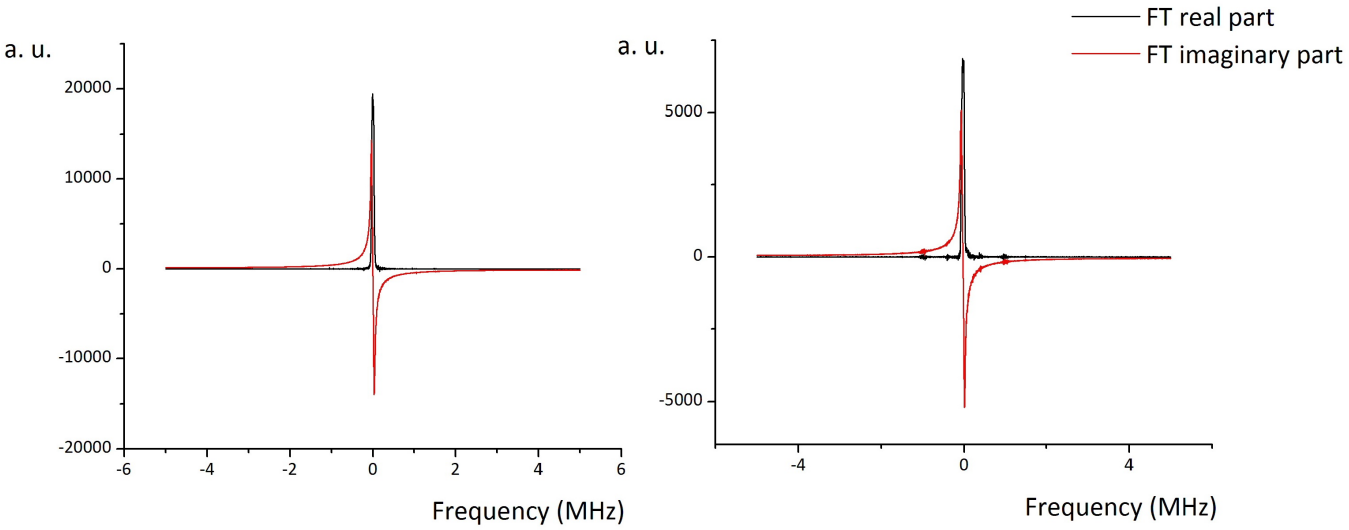


Figure 3.3: Real (black line) and imaginary part (red line) of the FT of the second half of the echo signal. Left: $\nu = 74,95$ MHz and $H = 1,87$ Tesla. Right: $\nu = 93,7$ MHz and $H = 2,34$ Tesla.

These spectra show a narrow and non shifted NMR line as a consequence of the *local* $\langle s \rangle^j = 0$ values leading to a zero hyperfine term in equation 2.29. By contrast, Néel antiferromagnetic compounds such as $KMnF_3$ [16] and $MnF_2$ [18] are characterized by non-zero local moments in the $S = 0$ singlet ground state. Thus their ground state NMR spectra show very large hyperfine shifts and broadening due to the finite value of the sublattice local electronic magnetization.

Careful obseravation of the NMR singlets shown in figure 3.2 reveals some structure of the spectral peak. A slightly shifted signal might be due to the Fluorine nuclei in the Teflon constitutents of the co-axial cable in the NMR probe [2]. Those nuclei experience a magnetic field that is different from the field at the sample because of their different position in the NMR probe.

## 3.2 Structured $Cr_8$ spectra

$^{19}$F-NMR measurements have been performed in $Cr_8$ single crystals at Larmor fields approximatively equal to 4 Tesla, 6 Tesla and 7,8 Tesla. The last value lies above the first critical field value $H_{c1}$. These spectra have been collected by applying the magnetic field perpendicular to the $a$-axis, namely parallel to the molecular ring and by applying the field along the $a$-axis, namely perpendicular to the molecular ring, as shown in figure 3.4.

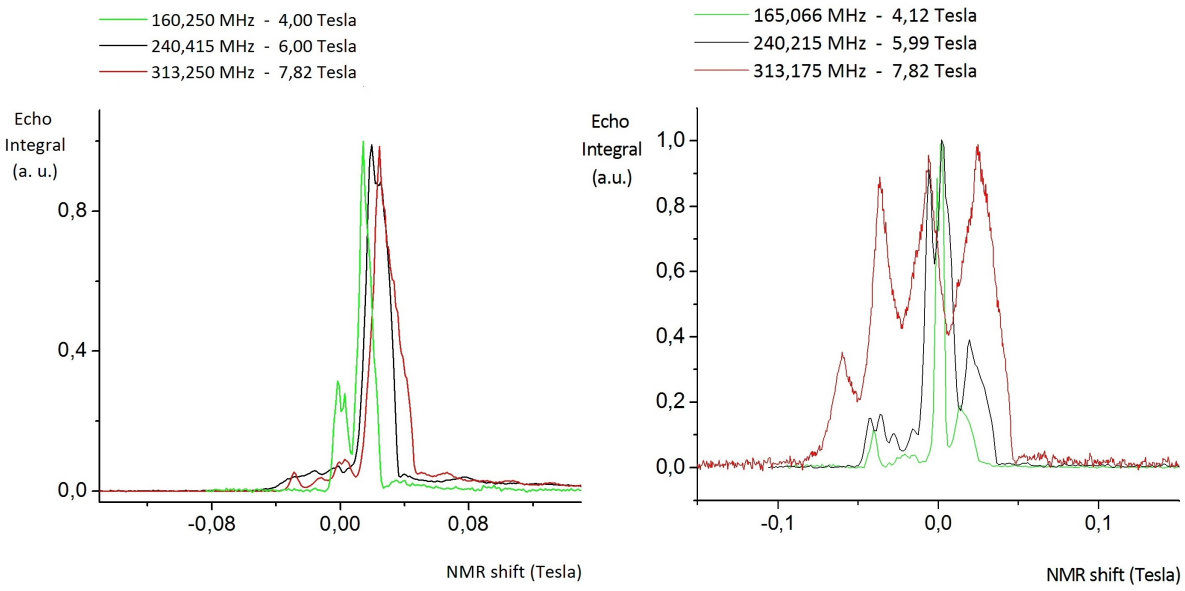


Figure 3.4: $^{19}$F-NMR spectra of a $Cr_8$ single crystal at $T = 1,6$ K. The applied field $H$ is parallel to the molecular ring namely perpendicular to the $a$-axis (left) and perpendicular to the molecular ring namely parallel to the $a$-axis (right). Spectra at Larmor fields of about 4 Tesla, 6 Tesla and 7,8 Tesla have been collected for both magnetic field orientations.

These spectra are broad and structured due to the thermal population of the excited magnetic levels. The most striking feature of these experimental results is their dependence on the field orienta-

[2]The sample has been wrapped with weight paper and put in the copper wire coil, the coil has been wrapped with Parafilm strips. Both the weight paper and the Parafilm strips do not contain Fluorine. Teflon tape has not been used in order to avoid its Fluorine contribution to the NMR signal.

tion, that is their anisotropy. In particular the spectra collected by orienting the field along the $a$-axis show sharp shifted peaks and a structure that broadens with increasing applied magnetic field. These shifted NMR lines are most likely produced by the non-zero hyperfine interaction terms resulting from the finite expectation values of the electronic spin moments.

Nevertheless an interpretation of these experimental results by means of the proposed local moments expectation values shown in figure 1.5 is not possible. This inadequacy of the existing model is illustrated in the following.

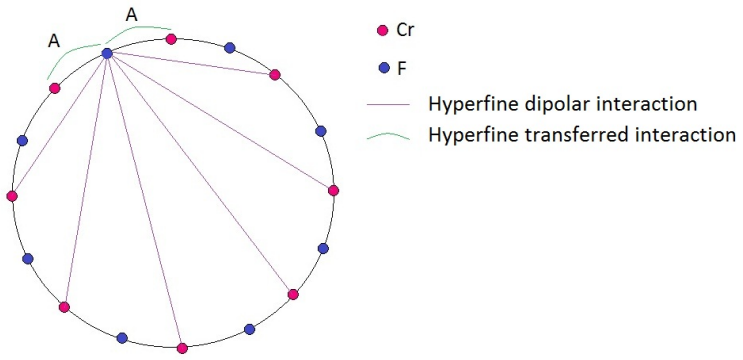


Figure 3.5: Schematic sketch of the intracluster hyperfine interactions between a given $^{19}$F nucleus and the magnetic $Cr^{3+}$ ions. Assumption is made that nearby ions produce a transferred hyperfine field at the nuclear site while far away ions generate a classical dipolar hyperfine field at the $^{19}$F nucleus.

Let us assume that the local spin expectation values are given by the calculated results shown in figure 1.5 referring to the operation temperature $T = 1,5$ K. We consider the simple model schematized in figure 3.5 where distinction is made between the two $Cr^{3+}$ ions neighboring to a given $^{19}$F nucleus and the six remaining far away magnetic ions. We assume that the hyperfine field generated at each $^{19}$F nuclear site by the electronic moments belonging to the far away $Cr^{3+}$ ions can be calculated within the point-dipole approximation by means of the classical equation 2.27. This calculation yields hyperfine fields at the nuclear sites whose order of magnitude is $10^{-5} \div 10^{-3}$ Tesla, to be compared to the $10^{-2} \div 10^{-1}$ Tesla total width of the spectral structures in the measured spectra. This classical contribution to the NMR shifts can therefore be disregarded.

Viceversa, if the assumption is made that the contribution to the hyperfine field at the nuclear site due to the neighboring $Cr^{3+}$ ions can be described by means of an isotropic transferred interaction term (see equation 2.32) one has:

$$\nu = \frac{\gamma}{2\pi}\Big(H + A\sum_j g_j \langle s \rangle^j\Big) \tag{3.1}$$

where the sum extends over the two neighboring $Cr^{3+}$ ions. If one relies on the theoretical result described by figure 1.5 the eight spin moments have the same expectation value $\langle s \rangle = \langle s(H) \rangle$. Equation 3.1 therefore yields:

$$H - \nu\frac{2\pi}{\gamma} = -2Ag\langle s(H) \rangle. \tag{3.2}$$

The left handside of equation 3.2 represents the NMR shift: according to this expression the measured shift varies linerly with the field-dependent local spin expectation value $\langle s(H) \rangle$.

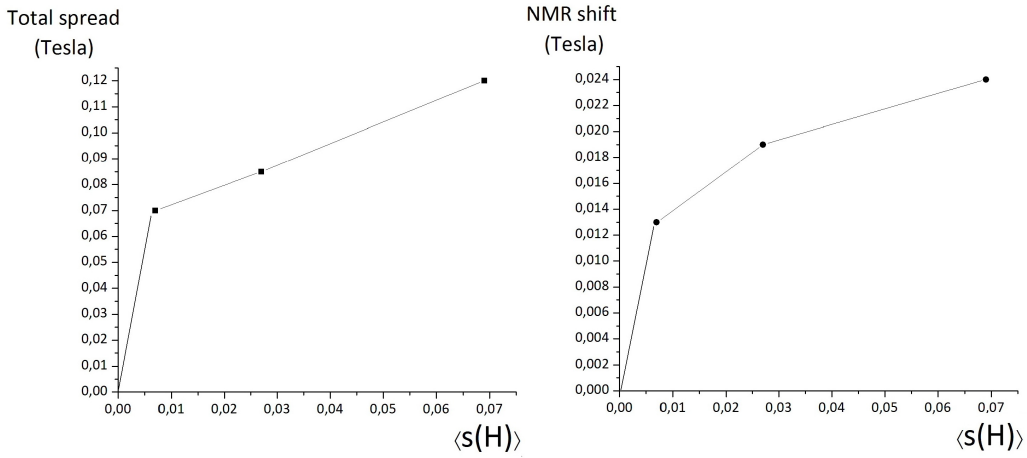


Figure 3.6: Analysis of the experimental results of figure 3.4 (right). Left: Observed spectral total spead as a function of the local spin value $\langle s(H)\rangle$. Right: Observed NMR shift as a function of the local spin value $\langle s(H)\rangle$. In this graph the experimental NMR shift of the most positively shifted peak in spectra 3.4 (right) is considered. The line is a guide to the eye.

The plot of the observed NMR shift versus the local spin value is illustrated in figure 3.6 (right) where a peak with a positive field shift has been chosen in the spectra reported in figure 3.4 (right). The non-linear behaviour shown by the curve reveals the inadequacy of the adopted model. Furthermore, a major feature of these experimental results shown in figure 3.4 is that the spectra are largely affected by the field orientation. This result cannot be explained within the simple model illustrated above since the anisotropic dipolar hyperfine interaction yields a negligible contribution (see above) and in the isotropic expression 3.1 describing the hyperfine transferred interaction the magnitude of the magnetic moments does not show a sufficient dependence on the field orientation to explain the results in figure 3.4.

The anisotropy shown by the experimental results seems to be consistent with the presence of a large anisotropic transferred hyperfine interaction between the $^{19}$F nuclear magnetic moment and the nearby electronic moments [3]. This interaction depends on the direction of the $p_\sigma$ and $p_\pi$ $^{19}$F - $Cr^{3+}$

[3]The resonance frequency of the $^{19}$F nucleus belonging to the fluoride bridging lingand located between the magnetic ions $Cr^{3+}$ site $a$ and $Cr^{3+}$ site $b$ can be expressed (in the case of the magnetic field being applied perpendicular to the molecular ring) by means of equation 2.32 as follows:

$$\nu\frac{2\pi}{\gamma} = H+[A_t+A_\sigma(3\cos^2\theta_\sigma-1)_a+A_\pi(3\cos^2\theta_\pi-1)_a]\cdot g\langle s\rangle_a+[A_t+A_\sigma(3\cos^2\theta_\sigma-1)_b+A_\pi(3\cos^2\theta_\pi-1)_b]\cdot g\langle s\rangle_b \quad (3.3)$$

where the $F^-$ - $Cr^{3+}$ $a$ bond and the $F^-$ - $Cr^{3+}$ $b$ bond can be characterized by different values of the angles $\theta_\sigma$ and $\theta_\pi$ betwen the directional $p_\sigma$ and $p_\pi$ orbitals and the axis of the applied field. If we assume the theoretical electronic moments local expectation values shown in figure 1.5 we get:

$$g\langle s\rangle_a = g\langle s\rangle_b$$

and the NMR shift is:

$$H-\nu\frac{2\pi}{\gamma} = -[2A_t + A_\sigma(3\cos^2\theta_\sigma - 1)_a + A_\pi(3\cos^2\theta_\pi - 1)_a + A_\sigma(3\cos^2\theta_\sigma - 1)_b + A_\pi(3\cos^2\theta_\pi - 1)_b]\cdot g\langle s\rangle. \quad (3.4)$$

Thus the NMR shift turns out to be proportional to the field-dependent local spin expectation value also if the anisotropic transferred hyperfine term is explicitely considered. As discussed in the text, this linear dependence is not shown by the experimental results reported in figure 3.6.

bonds with respect to the external magnetic field (see equation 2.32). The theoretical analysis of the $^{19}$F spectra in terms of anisotropic transferred hyperfine interaction requires a detailed study of the electronic structure of the ring and it is beyond the scope of this thesis. One can only qualitatively observe that also for the case of anisotropic interaction a spectral overall spread proportional to the calculated $\langle s(H) \rangle$ densities is expected. Instead, the spread (see figure 3.6 left) behaves similarly to the NMR shift (see figure 3.6 right). Thus it appears that the determination of the $\langle s(H) \rangle$ spin densities is not a settled issue.

# Chapter 4

# Cr7Cd

The present chapter focuses on the investigation of the magnetic properties of $Cr_7Cd$ heterometallic ring by means of Nuclear Magnetic Resonance. The first section briefly illustrates one of the most striking experimental results of the last few years concerning the magnetic properties of AFM rings: the model independent determination of the core polarization constant $A_{cp}$ and of the local spin expectation values of the $Cr^{3+}$ magnetic ions in $Cr_7Cd$ by means of $^{53}$Cr-NMR by Micotti *et al.* [21] in 2006. In the second section of this chapter an estimate of the $Cr^{3+}$ - $^{19}$F transferred hyperfine constant by means of $^{19}$F-NMR measurements is proposed. This yields useful information about the percentage of $p$ covalent character of the $Cr^{3+}$ - $F^-$ bond.

## 4.1 $^{53}$Cr-NMR

The hyperfine constant value $A_{cp}$ and the local spin distribution of the $Cr^{3+}$ magnetic ions in $Cr_7Cd$ have been experimentally determined by E. Micotti, Y. Furukawa, K. Kumagai, S. Carretta, A. Lascialfari, F. Borsa, G. A. Timco and R. E. P. Winpenny by means of $^{53}$Cr-NMR in a work published in 2006 [21]. These determinations are relevant to the analysis and discussion of the experimental results of the present work. The value of the hyperfine constant $A_{cp}$ of the $Cr^{3+}$ magnetic ions in $Cr_7Cd$ is utilized in section 5.1 in the interpretation of $^{53}$Cr-NMR spectra in $Cr_7Ni$. Also, the experimental determination of the local spin moments in $Cr_7Cd$ is in good agreement with the theoretically predicted values enabling us to use these latter calculated values in section 4.2 in the analysis of the $^{19}$F-NMR spectra of $Cr_7Cd$. The present section summarizes how these important results have been obtained.

$^{53}$Cr-NMR spectra in $Cr_7Cd$ have been measured by means of a pulsed NMR spectrometer at $T = 1,5$ K. The magnetic field has been applied along the $z$ axis perpendicular to the molecular ring. The spectra have been collected point by point by integrating the Hahn echo while sweeping the external field at the fixed Larmor frequency $\nu_L$ according to the procedure described in section 2.6. Due to its low natural abundance (9,54%) and to the small gyromagnetic ratio ($\frac{\gamma}{2\pi} = 2,406$ MHz/Tesla) the $^{53}$Cr-NMR signal is very difficult to be detected [1]. Nevertheless very weak $^{53}$Cr-NMR signals have been observed at low temperature ($T = 1,5$ K) and high magnetic fields ($H \sim 6 \div 8$ Tesla).

[1] The signal to noise ratio turns out to be proportional to the nuclear gyromagnetic ratio $\gamma$ [10].

The observed $^{53}$Cr-NMR signals obey to the following equation:

$$\nu_{\mathrm{L}} = \frac{\gamma}{2\pi}(H + g\langle s\rangle A_{\mathrm{cp}}) \tag{4.1}$$

describing the resonance frequency $\nu_{\mathrm{L}}$ of each $^{53}$Cr nucleus. In this equation $g$ is the electronic Landé factor, $\langle s\rangle$ is the electronic spin expectation value [2] of the $Cr^{3+}$ magnetic ion and $A_{\mathrm{cp}}$ is the hyperfine core polarization constant whose origin is described in section 2.5.3. Due to the simmetry properties of the molecule, we can recognize in $Cr_7Cd$ four inequivalent $Cr^{3+}$ sites, namely Cr 1 - Cr 7, Cr 2 - Cr 6, Cr 3 - Cr 5, Cr 4. The usual labelling is shown in figure 4.1 (right). These sites are expected to have different spin moment expectation values giving rise to different NMR shifts according to equation 4.1. Four NMR signals are therefore expected.

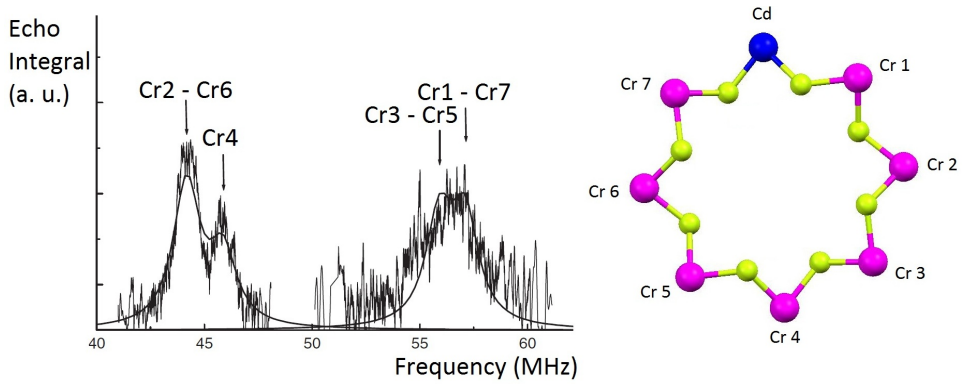


Figure 4.1: $^{53}$Cr-NMR spectrum of a $Cr_7Cd$ single crystal collected at $T = 1,5$ K by applying the magnetic field perpendicular to the molecular ring [21]. The abscissa reports the NMR frequency normalized to zero field (see equation 4.2).

The experimental result is shown in figure 4.1 (left) where the spectral intensity i. e. the echo signal integral is plotted as a function of the NMR frequency normalized to zero field namely:

$$\nu_{\mathrm{L}} - \frac{\gamma}{2\pi}H = \frac{\gamma}{2\pi}g\langle s\rangle A_{\mathrm{cp}} = \frac{\gamma}{2\pi}H_{\mathrm{Int}} \tag{4.2}$$

where the hyperfine field at the nucleus is $H_{\mathrm{Int}} = g\langle s\rangle A_{\mathrm{cp}}$. Figure 4.1 shows that the sites Cr 3 - Cr 5 and Cr 1 - Cr 7 give rise to almost overlapping signals: this is due to very similar spin expectation values. The plot of the resonance frequency $\nu_{\mathrm{L}}$ as a function of the applied field $H$ is shown in figure 4.2 where the experimental results turn out to lie on straight lines as predicted by equation 4.1. The NMR signals could be assigned unambiguously to the different magnetic sites by observing that the intensity of the signal produced by the Cr 4 site is expected to be a half of the other three signal intesities and that, due to the antiferromagnetic ordering, adjacent sites have antiparallel spins resulting in opposite $\nu_{\mathrm{L}}$ versus $H$ slopes in figure 4.2.

The value of the hyperfine core polarization constant $A_{\mathrm{cp}}$ could be determined independently from the experimental NMR shifts $H^{\mathrm{Exp}}_{\mathrm{Int,i}}$ by means of the following sum rule:

$$A_{\mathrm{cp}} = \frac{2H^{\mathrm{Exp}}_{\mathrm{Int,Cr1-7}} + 2H^{\mathrm{Exp}}_{\mathrm{Int,Cr2-6}} + 2H^{\mathrm{Exp}}_{\mathrm{Int,Cr3-5}} + H^{\mathrm{Exp}}_{\mathrm{Int,Cr4}}}{g\frac{3}{2}} \tag{4.3}$$

[2] The magnetic field is applied along the $z$ axis perpendicular to the molecular ring and in this configuration only the component of the electronic magnetic moment directed along the applied field is non zero.

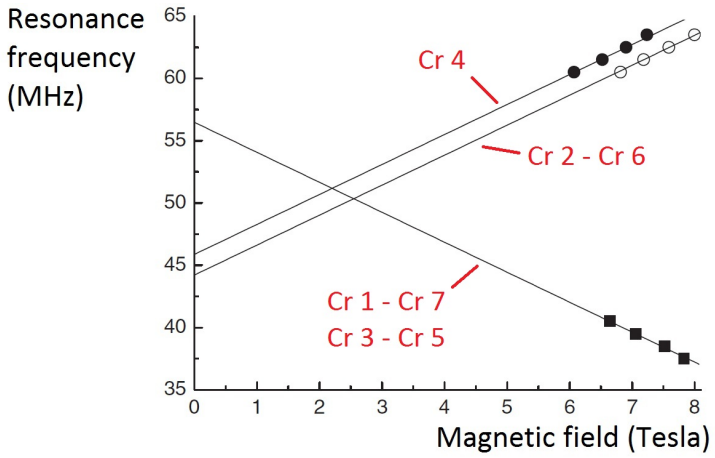


Figure 4.2: $^{53}$Cr-NMR frequency as a function of the applied field in a $Cr_7Cd$ single crystal at $T = 1,5$ K [21]. The magnetic field is perpendicular to the molecular ring.

where $\frac{3}{2}$ is the ground state total spin value and $g = 1,98$ is the electronic Landé factor. Equation 4.3 yields:

$$A_{\rm cp} = -12,38 \pm 0,23 \,\text{Tesla} \tag{4.4}$$

to be compared to the calculated value $A_{\rm cp} = -12,5$ Tesla [20] (see Appendix A.1).

The electronic spin moment local expectation values have been calculated by observing that:

$$\langle s_z^i \rangle = \frac{H_{\rm Int,i}^{\rm Exp}}{g A_{\rm cp}}. \tag{4.5}$$

These experimentally determined values are in good agreement with the theoretical prediction shown in figure 1.14 (left) in section 1.2.2.

## 4.2 $^{19}$F-NMR

$^{19}$F-NMR measurements have been perfomed on a $Cr_7Cd$ single crystal at $T = 1,5$ K. Field-sweep spectra have been measured at the fixed Larmor frequency $\nu_{\rm L} = 280,14$ MHz corresponding to a Larmor field value of 6,99 Tesla [$\gamma(^{19}\text{F}) = 40,059$ MHz/Tesla]. The spectra have been collected at different $\theta$ values, where $\theta$ is the angle between the applied magnetic field and the $c$ axis (or $z$ axis) perpendicular to the molecular ring [3].

Figure 4.3 shows the experimental results at different values of $\theta$. The echo integral is recorded according to the procedure described in section 2.6 and is plotted as a function of the NMR field shift, where the zero value corresponds to the $^{19}$F Larmor field. The large and broad signal with negative shift is produced by the $^1$H resonance at 6,58 Tesla due to $\gamma(^1\text{H}) = 42,5756$ MHz/Tesla. The large and narrow non shifted signal is due to the Teflon tape (Polytetrafluoroethilene, whose chemical formula is shown in figure 4.4) $^{19}$F resonance [4].

[3] It is worthwhile observing that while in $Cr_8$ the $a$-axis is the axis perpendicular to the molecular ring (see figure 1.2 and 3.1) in the heterometallic rings $Cr_7Ni$ and $Cr_7Cd$ the axis perpendicular to the molecular ring is labelled with

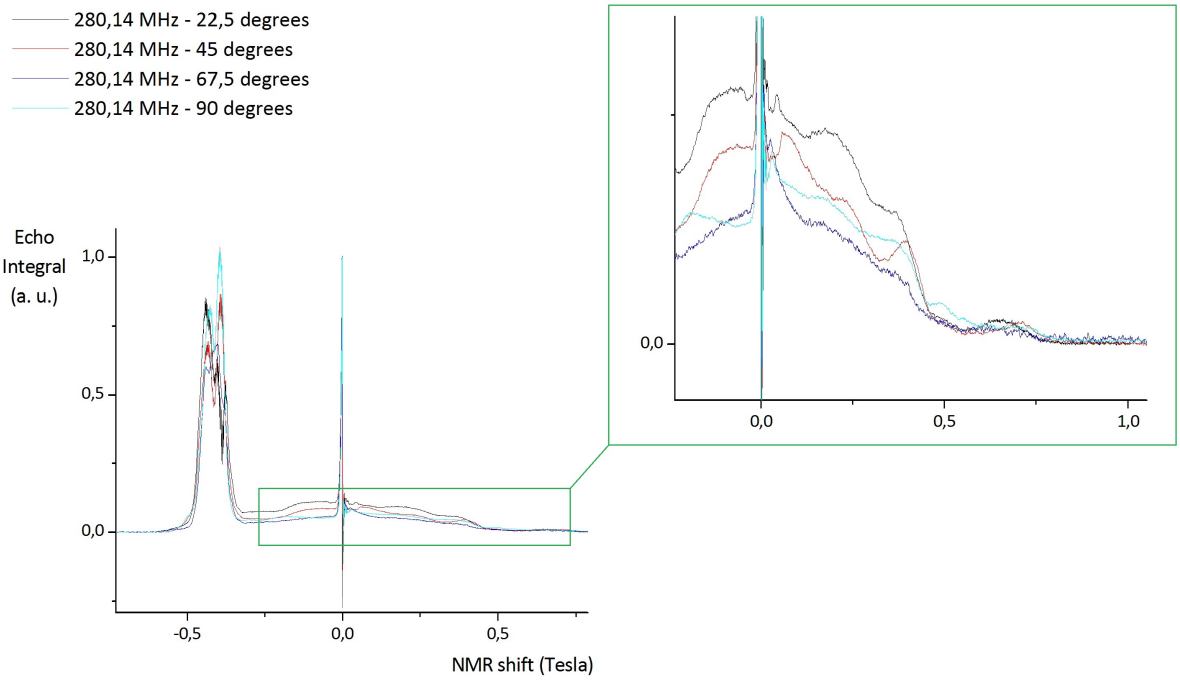


Figure 4.3: $^{19}$F-NMR spectra of a $Cr_7Cd$ single crystal at $T = 1,5$ K and at different orientations of the applied magnetic field. The legend reports the values expressed in degrees of the angle $\theta$ i. e. the angle between the applied magnetic field and the $c$-axis perpendicular to the molecular ring. The large and broad signal with negative shift is due to the $^1$H resonance. The $^{19}$F-NMR signal has been zoomed in and is shown in the insert.

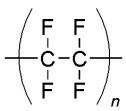


Figure 4.4: Teflon (Polytetrafluoroethilene) chemical formula.

The sample's $^{19}$F-NMR spectra are shown in the insert of figure 4.3. These spectra present some dependence on the direction of the applied field due to the anisotropic terms of the hyperfine hamiltonian namely the classical electron-nucleus dipolar interaction 2.27 that is inherently anisotropic and the anisotropic contribution to the transferred hyperfine coupling (see equation 2.32). The $^{19}$F-NMR spectrum is composed of a slightly shifted broad structure and of a positively shifted peak whose position depends on the applied field direction. The NMR shift of this peak is easily identified in the case $\theta = 22,5$ degrees and $\theta = 45$ degrees as shown in figure 4.5. This signal has a $0,66 \pm 0,01$ Tesla NMR shift in the case $\theta = 22,5$ degrees and a $0,71 \pm 0,01$ Tesla shift in the case $\theta = 45$ degrees. A

$c$ (see figure 1.9 and 1.11).

[4]These spectra have been collected in 2006 on fresh samples. The large non shifted signal is due to the $^{19}$F nuclei in the Teflon tape i. e. Polytetrafluoroethilene tape wrapping the sample. New measurements on the same $Cr_7Cd$ samples have been performed as part of this thesis experimental work at Ames Laboratory in 2011. In these new measurements we wrapped the sample with weight paper and the copper wire coil with Parafilm strips in order to avoid the Teflon contribution to the $^{19}$F-NMR signal. However these new spectra turned out to be not reliable probably due to alterations of the five years old samples and have therefore been discarded.

simple interpretative model is proposed in the following.

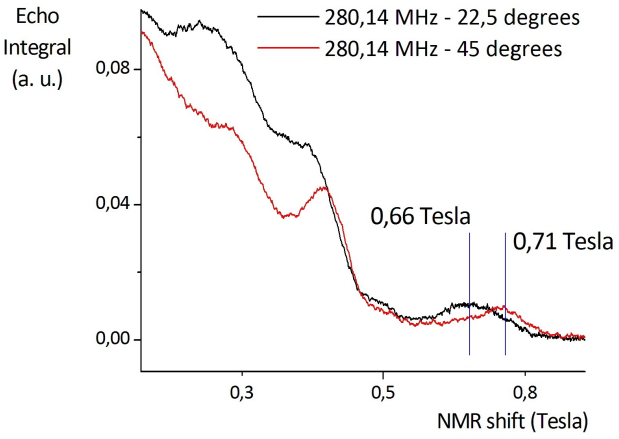


Figure 4.5: Position of the shifted peaks in the 22,5 degrees and 45 degrees spectra shown in figure 4.3.

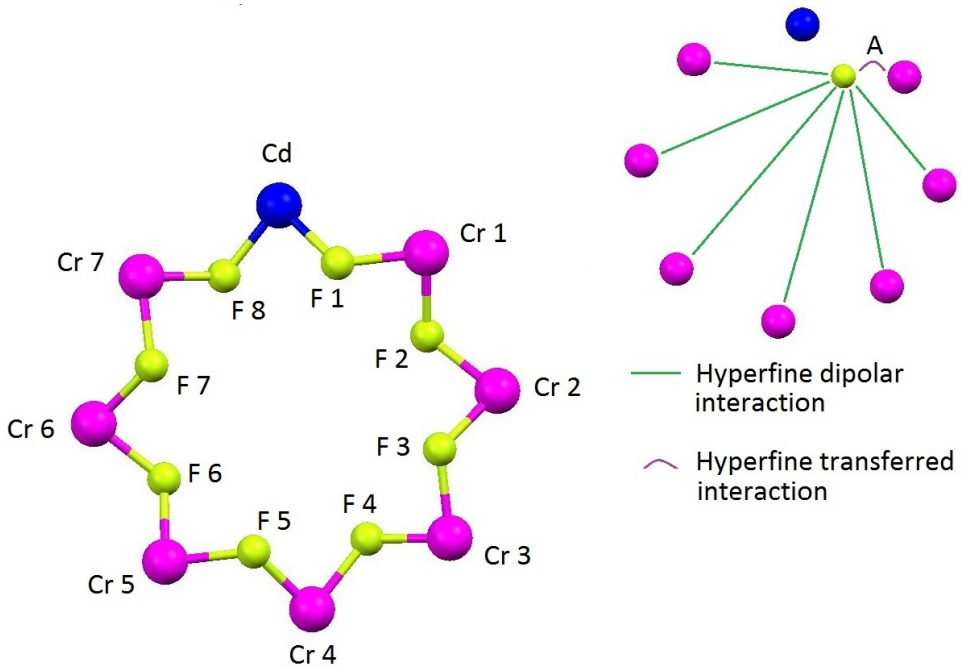


Figure 4.6: Labelling of the $^{19}$F nuclear sites and of $Cr^{3+}$ magnetic ions in $Cr_7Cd$ molecular ring (left). Schematic diagram of the interactions giving rise to the hyperfine field at a given $^{19}$F nuclear site (right).

By analogy with the case of $Cr_8$ discussed in section 3.2 we assume that the hyperfine field produced by the $Cr^{3+}$ magnetic ions at a given $^{19}$F nuclear site consists essentially of two terms as shown schematically in figure 4.6 (right). The far away $Cr^{3+}$ ions produce a classical dipolar hyperfine field at the $^{19}$F nucleus. This field can be calculated within the point-dipole approximation by means of equation 2.27 yielding hyperfine fields at the nuclear sites whose order of magnitude is $10^{-3} \div 10^{-2}$ Tesla. This contribution can therefore be neglected. Viceversa we assume that the contribution to the hyperfine field at the nuclear site due to the neighboring $Cr^{3+}$ ions can be described by means

of a transferred hyperfine interaction term described by equation 2.32. The anisotropic terms in equation 2.32 are proportional to the transferred hyperfine anisotropic constants $A_\sigma$ and $A_\pi$ due to the dipolar interaction averaged over the $p_\sigma$ and $p_\pi$ wavefunctions involved in the $Cr^{3+}$ - $F^-$ bond and are responsible for the angular dependence of the spectra in figure 4.3. The separate determination of the constants $A_t$, $A_\sigma$ and $A_\pi$ from the spectra is a difficult problem and we will not try it in the present work.

Assumption is made that the slightly shifted structure is due to the $^{19}F$ nuclear sites far away from the $Cd^{2+}$ ion namely F 2, F 3, F 4, F 5, F 6 and F 7 according to the usual labelling shown in figure 4.6 (left). In fact these fluoride ions are bridging ligands located approximatively half-way between two antiparallel $Cr^{3+}$ magnetic moments. The vectorial sum of the hyperfine fields produced by these moments at the $^{19}F$ nucleus results in a small local field yielding a small NMR shift. On the other hand the $^{19}F$ nuclei neighboring to the $Cd^{2+}$ non magnetic ion, namely F 1 and F 8, experience the hyperfine field produced by one $Cr^{3+}$ magnetic moment namely Cr 1 and Cr 7 respectively. We thus assign to these $^{19}F$ nuclei the most shifted peak whose position varies approximatively in the range $0,66 \pm 0,01$ Tesla $\div$ $0,71 \pm 0,01$ Tesla with varying $\theta$.

We thus propose that F 1 and F 8 NMR shift can be described by the equation:

$$(H - \nu\frac{2\pi}{\gamma})_{\mathrm{F1,F8}} = -Ag\langle s\rangle_{\mathrm{Cr1,Cr7}} \tag{4.6}$$

where $g = 1,98$ is the electronic Landé factor. $A$ is the transferred $^{19}F$ - $Cr^{3+}$ hyperfine constant relating to the site neighboring to the $Cd^{2+}$ ion given by equation 2.32. It is worthwhile stressing that according to equation 2.32 this hyperfine constant includes both the isotropic contribution $A_t$ and the anisotropic terms $A_\sigma$ and $A_\pi$.

$\langle s\rangle_{\mathrm{Cr1,Cr7}}$ is the component of the spin local expectation value at sites 1 and 7 directed along the applied field. As observed in section 1.2.2 when the magnetic field is applied perpendicular to the molecular ring the electronic magnetic moments are aligned along this applied field: their expectation values have been predicted theoretically at $T = 1,5$ K and are shown in figure 1.14. These calculated values are in excellent agreement with the experimental ones as pointed out in section 4.1. The theoretical value of the Cr 1 and Cr 7 magnetic moment expressed in Bohr magnetons is $g\langle s\rangle_{\mathrm{Cr1,Cr7}} = 2,14$. This value refers to the case $\theta = 0$. Nevertheless we assume that we can use this value in the interpretation of the spectra even if the magnetic field is not directed along the $c$ crystallographic axis [5].

Equation 4.6 yields the following estimate of the transferred $^{19}F$ - $Cr^{3+}$ hyperfine constant [29]:

$$A = -0,308 \pm 0,005 \text{ Tesla} \div -0,332 \pm 0,005 \text{ Tesla}. \tag{4.7}$$

These results represent the transferred hyperfine field at the $^{19}F$ nuclear site per Bohr magneton in the case $\theta = 22,5$ degrees and $\theta = 45$ degrees respectively. As stated above, these values refer to the overall transferred hyperfine constant according to equation 2.32. Somehow surprisingly the results in equation 4.7 are negative values. This result cannot be explained in the hypothesis of a transferred hyperfine coupling (equation 2.32) consisting of a dominant isotropic term and of negligible anisotropic contributions, as in the case of antiferromagnetic $KMnF_3$ and $MnF_2$ described in Appendix A. The

[5] Figure 1.14 reports the values relating to $\theta = 0$ and those relating to $\theta = \pi/2$ showing only a slight difference between them. The final result of this section estimates does not significantly change if the $\theta = \pi/2$ values are used.

negative sign could be due to a transferred core polarization interaction in which the magnetic electrons produce an hyperfine field at the $^{19}$F nucleus via the polarization of the $s$ core electrons of the $F^-$ ion. In addition to this, a negative anisotropic term could dominate over the positive isotropic contribution in equation 2.32 yielding a negative value of the overall constant. The anisotropic term can reasonably be negative due to the angle dependent factors.

According to this latter interpretation it is possible to estimate the order of magnitude of the percentage $f_p$ of $p$ covalent character of the $F^-$ - $Cr^{3+}$ bond in $Cr_7Cd$. By analogy with the procedure illustrated in Appendix A.2 and in Appendix A.3 referring to $KMnF_3$ and $MnF_2$ respectively, and by assuming the modulus of the intermediate value in equation 4.7 namely $A = 0,320 \pm 0,005$ Tesla per Bohr magneton as a rough estimate of the order of magnitude of the anisotropic transferred component we get[6]:

$$f_p = \frac{A \cdot g\langle s\rangle_{\mathrm{Cr1,Cr7}}}{16,5 \text{ Tesla}} \sim 4,2\ \% \tag{4.8}$$

where $g\langle s\rangle_{\mathrm{Cr1,Cr7}} = 2,14$ is the Cr 1 and Cr 7 magnetic moment expressed in Bohr magnetons. In equation 4.8 the term $A \cdot g\langle s\rangle_{\mathrm{Cr1,Cr7}}$ represents the anisotropic transferred hyperfine field produced by the neighbouring $Cr^{3+}$ electronic spin at the $^{19}$F nuclear site while the denominator is the hyperfine direct field at the $^{19}$F nucleus due to a single unpaired $2p$ electron according to equation A.2.

It is worthwhile stressing that this last result represents a very rough estimate due to the fact that the experimental result 4.7 includes both the isotropic and the anisotropic contributions and that this latter consists of $\sigma$ and $\pi$ angle dependent terms. As stated above in order to evaluate the separate $A_t$, $A_\sigma$ and $A_\pi$ contributions one should be able to determine the values of the angles $\theta_\sigma$ and $\theta_\pi$ between the directional $p_\sigma$ and $p_\pi$ bonds and the applied magnetic field direction. This requires the detailed study of the molecular orbitals involved in the $Cr^{3+}$ - $F^-$ coordinative bond and goes beyond the scope of the present work.

[6]No error has been reported in this result as it represents only a rough estimate.

# Chapter 5

# Cr7Ni

The present chapter illustrates the Nuclear Magnetic Resonance measurements that have been performed in the heterometallic $Cr_7Ni$ ring as part of this thesis experimental work. Both the $^{53}$Cr-NMR and the $^{19}$F-NMR have been investigated by means of sophisticated low temperature and high magnetic field facilities at Ames Laboratory [1]. The first section of this chapter describes the $^{53}$Cr-NMR measurements performed in $Cr_7Ni$ single crystals: these results are in good agreement with the theoretically predicted local spin moment distribution shown in figure 1.16. The second section illustrates the $^{19}$F-NMR experiments in $Cr_7Ni$ single crystals. A detailed analysis of these results is described with the purpose of estimating the order of magnitude of the $^{19}$F - $Cr^{3+}$ and $^{19}$F - $Ni^{2+}$ transferred hyperfine constants.

## 5.1 $^{53}$Cr-NMR

As pointed out in section 4.1, $^{53}$Cr-NMR signal is very weak and hard to be detected due to the $^{53}$Cr nucleus low natural abundance (only 9,54%) and small gyromagnetic ratio ($\frac{\gamma}{2\pi}(^{53}\mathrm{Cr}) = 2,406$ MHz/Tesla). Though often unsuccessful, $^{53}$Cr-NMR experimental attempts are worthwhile due to the straightforward information that these measurements can provide concerning the local spin moment distribution of the magnetic $Cr^{3+}$ ions.

$^{53}$Cr-NMR experiments in $Cr_7Ni$ single crystals have been performed at Ames Laboratory by means of the experimental apparatus labelled "set-up 1" described in section 2.6 at the temperature of operation $T = 1,6$ K. Field-sweep spectra have been collected according to the procedure described in section 2.6.2. The sample has been roughly oriented by means of a microscope. A weak broad $^{53}$Cr-NMR signal has been observed.

Figure 5.2 (left) shows some experimental spectra collected by applying the magnetic field perpendicular to the crystallographic *c*-axis namely parallel to the molecular ring. Viceversa figure 5.3 (left) reports some of the spectra that have been collected by applying the magnetic field parallel to the crystallographic *c*-axis i. e. perperpendicular to the molecular ring. In both cases the full width at half maximum (FWHM) of these peaks is approximatively 1 Tesla. These signals can be unambiguously assigned to the $^{53}$Cr-NMR nucleus: in fact as the settled value of the radiofrequency increases by 1

[1] Department of Physics and Astronomy, Ames Laboratory, Iowa State University, Ames, IA.

MHz a $\sim 0,42$ Tesla shift of the NMR signal is observed due to $\frac{\gamma}{2\pi}(^{53}\mathrm{Cr}) = 2,406$ MHz/Tesla, as shown in figure 5.2 and 5.3.

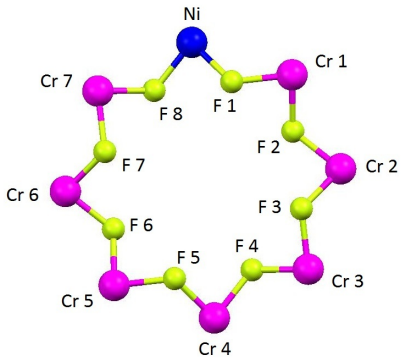


Figure 5.1: $Cr^{3+}$and $F^-$ ions in use labelling in $Cr_7Ni$ heterometallic ring.

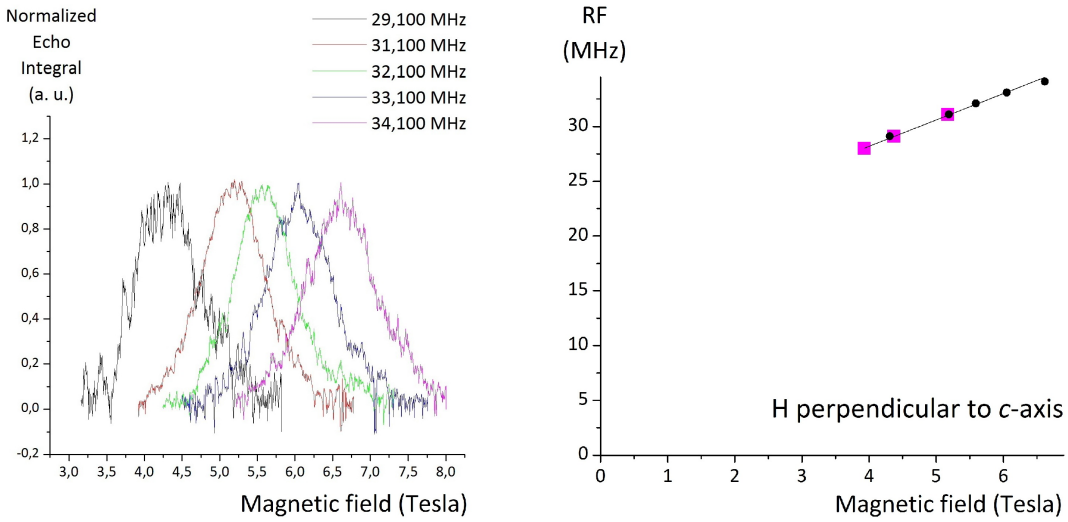


Figure 5.2: Left: $^{53}$Cr-NMR spectra of a $Cr_7Ni$ single crystal at $T = 1.6$ K, the magnetic field is applied perpendicular to the crystallographic $c$-axis namely parallel to the molecular ring. Right: the radiofrequency versus applied field experimental points. Two data sets are shown corresponding to different samples and/or slightly different orientations. The black points correspond to the spectra on the left. The straight line represents the best fit according to equation: $y = C + 2,406 \cdot x$ yielding $C = 18,57 \pm 0,06$ MHz.

The observed $^{53}$Cr-NMR signals in $Cr_7Ni$ can be easily explained based on the following argument. As for the case of $Cr_7Cd$ described in section 4.1, the resonance frequency $\nu_L$ of each $^{53}$Cr nucleus is given by [21]:

$$\nu_L = \frac{\gamma}{2\pi}(g\langle s\rangle A_{cp} \pm H) \tag{5.1}$$

where $H$ is the applied magnetic field and $g\langle s\rangle A_{cp}$ is the hyperfine core polarization field at the $^{53}$Cr nuclear site. $\frac{\gamma}{2\pi}$ refers to the $^{53}$Cr nucleus and equals 2,406 MHz/Tesla. In equation 5.1 $g$ is the $Cr^{3+}$ electronic Landé factor whose value is 1,98. $\langle s\rangle$ is the electronic spin local expectation value of the $Cr^{3+}$ magnetic ion. As pointed out in section 1.2.2, if the magnetic field is applied along the

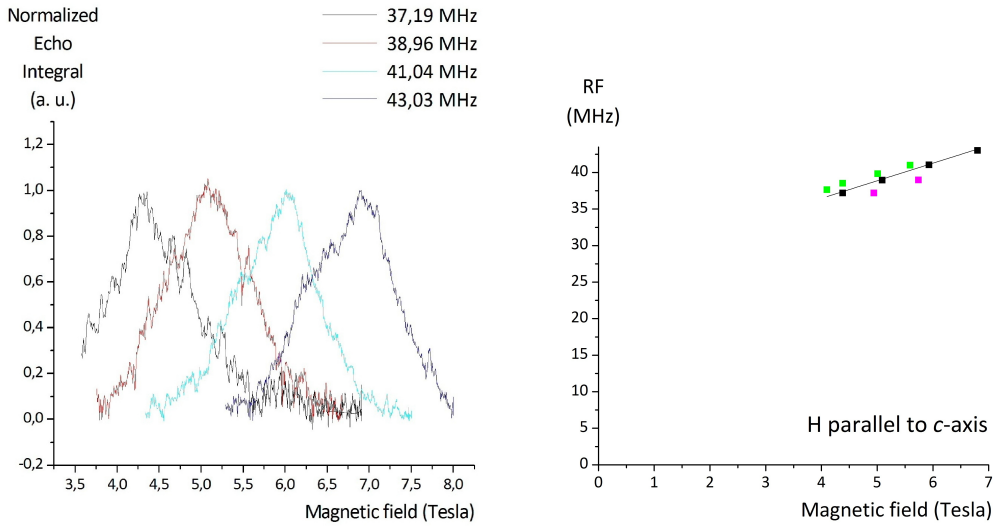


Figure 5.3: Left: $^{53}$Cr-NMR spectra of a $Cr_7Ni$ single crystal at $T = 1.6$ K, the magnetic field is applied parallel to the crystallographic $c$-axis namely perpendicular to the molecular ring. Right: the radiofrequency versus applied field experimental points. Three data sets are shown corresponding to different samples and/or slightly different orientations. The black points correspond to the spectra on the left. The straight line represents the best fit according to equation: $y = C + 2,406 \cdot x$ yielding $C = 26,8 \pm 0,3$ MHz.

crystallographic $c$-axis or perpendicular to this axis the electronic magnetic moments turn out to be parallel to the applied field due to the cylindrical simmetry of the magnetic $Cr_7Ni$ Hamiltonian. The electronic spin local expectation values have been calculated at the temperature of operation $T = 1,5$ K and the theoretical result is shown in figure 1.16 in the case of the magnetic field being perpendicular to the molecular ring (left) and parallel to the molecular ring (right). These figures show that the spin expectation values dependence on the magnetic field can be neglected in the field range of interest 4 - 8 Tesla. The local spin moment theoretical expectation values are summarized in Table 5.1 for both field orientations, where $T = 1,5$ K and $H = 5$ Tesla have been assumed. $A_{cp}$ is the hyperfine core polarization constant of the $Cr^{3+}$ ion whose origin is described in section 2.5.3. It represents the magnetic field per Bohr magneton generated at the $^{53}$Cr nuclear site by the ion's magnetic electrons via the polarization of the core $s$ electrons.

Quadrupole effects of the $^{53}$Cr (I=3/2) NMR can be disregarded since we measure the central line transition (+1/2 $\rightarrow$ -1/2) which is shifted only in second order and by a negligible amount at the magnetic fields of operation.

Equation 5.1 shows that the resonance radiofrequency $\nu_L$ of each $^{53}$Cr nucleus is a linear function of the applied magnetic field $H$. The slope equals $\frac{\gamma}{2\pi}(^{53}\text{Cr}) = +2,406$ MHz/Tesla if the internal field $g\langle s\rangle A_{cp}$ is parallel to the applied field corresponding to a local spin moment opposite to the external field [2]. Viceversa the slope has the negative value $-2,406$ MHz/Tesla if the core polarization field is antiparallel to the applied magnetic field $H$: this happens when the local spin moment is parallel to the applied field.

Figure 5.2 (left) shows some experimental spectra that have been collected by applying the magnetic

[2] $A_{cp}$ has a negative value.

Table 5.1: Electronic magnetic moment theoretical expectation values in $Cr_7Ni$ at $T = 1,5$ K and $H = 5$ Tesla corresponding to figure 1.16. The $g\langle s\rangle$ values represent the magnetic moments expressed in Bohr magnetons. $g = 1,98$ for the $Cr^{3+}$ ions and $g = 2,2$ for the $Ni^{2+}$ ion.

| | $H \perp c$ | $H \parallel c$ |
|---|---|---|
| Cr 1 | 0,88243 | 1,25315 |
| Cr 2 | -0,66861 | -1,07189 |
| Cr 3 | 0,82501 | 1,18954 |
| Cr 4 | -0,66181 | -1,07047 |
| Cr 5 | 0,82501 | 1,18954 |
| Cr 6 | -0,66861 | -1,0719 |
| Cr 7 | 0,88243 | 1,25315 |
| Ni | -0,48818 | -0,79632 |

field perpendicular to the crystallographic $c$-axis together with the plot of the radiofrequency as a function of the applied field experimental points (right). Two data sets are shown corresponding to different samples and/or slightly different orientations. The black points correspond to the spectra on the left. Viceversa figure 5.3 refers to the case of the magnetic field being applied parallel to the crystallographic $c$-axis. The discussion developed above leads to the conclusion that the experimental points in both configurations are due to Cr 2, Cr 4 and Cr 6 equivalent sites [3]. In fact, according to the theoretical values of the electronic spin moments shown in figure 1.16 at $T = 1,5$ K and reported in Table 5.1, Cr 2, Cr 4 and Cr 6 have a negative magnetic moment, yielding a positive core polarization hyperfine field due to $A_{\text{cp}} < 0$. This means that the core polarization field is parallel to the applied field and adds to this latter so that the radiofrequency versus magnetic field plot shows a positive slope.

Figure 5.2 (right) and 5.3 (right) show, together with the experimental points, the best fit curve of the form:

$$y = C + 2,406 \cdot x \tag{5.2}$$

where 2,406 MHz/Tesla is the $\frac{\gamma}{2\pi}$ vale of the $^{53}$Cr nucleus. The values $C = 18,57 \pm 0,06$ MHz and $C = 26,8 \pm 0,3$ MHz are obtained in the case of the magnetic field being perpendicular and parallel to the crystallographic $c$-axis respectively. According to equation 5.1 we assume:

$$C = \frac{\gamma}{2\pi} g\langle s\rangle A_{\text{cp}} \tag{5.3}$$

where Cr 2, Cr 4 and Cr 6 $g\langle s\rangle$ values are $-0,67$ and $-1,07$ in the case of the magnetic field being perpendicular and parallel to the crystallographic $c$-axis respectively (see Table 5.1). As stated above, according to figure 1.16 we can neglect the spin expectation values dependence on the magnetic field

[3] According to the theoretical predictions, Cr 2 and Cr 6 are equivalent while Cr 4 electronic magnetic moment is very close to the one of the Cr 2 - Cr 6 pair but not exactly equal.

in the range of interest 4 - 8 Tesla. Equation 5.3 yields:

$$A_{\rm cp} = -11,52 \pm 0,04 \text{ Tesla}$$

for the case of the magnetic field being applied perpendicular to the $c$-axis and

$$A_{\rm cp} = -10,4 \pm 0,1 \text{ Tesla}$$

for the case of the magnetic field being applied parallel to the crystallographic $c$-axis. This latter value can be compared to the value referring to Cr 2 and Cr 6 sites in $Cr_7Cd$ obtained as follows in the case of the magnetic field being oriented parallel to the $c$-axis i. e. perpendicular to the molecular ring:

$$\frac{H_{\text{Int, } Cr_7Cd}^{\text{Exp, } Cr_{2-6}}}{g\langle s\rangle_{Cr_7Cd}^{\text{Theo, } Cr_{2-6}}} = -11,05 \pm 0,02 \text{ Tesla.} \tag{5.4}$$

In this expression the core polarization constant relating to the Cr 2 and Cr 6 sites in $Cr_7Cd$ is calculated by means of the experimental $^{53}$Cr-NMR shift $H_{\text{Int, } Cr_7Cd}^{\text{Exp, } Cr_{2-6}}$ provided by the measurements described in section 4.1 and reported in reference [21]. The electronic spin expectation value $\langle s\rangle_{Cr_7Cd}^{\text{Theo, } Cr_{2-6}}$ in the denominator of equation 5.4 is the theoretical value shown in figure 1.14 of section 1.2.2. We observe that value given by equation 5.4 in $Cr_7Cd$ is very close to $A_{\rm cp} = -10,4 \pm 0,1$ Tesla determined for $Cr_7Ni$ in the same magnetic field orientation.

As the core polarization constant is inherently isotropic it appears reasonable to consider for $Cr_7Ni$ the average of the values obtained in the two configurations [29]:

$$A_{\rm cp} = -10,96 \pm 0,07 \text{ Tesla.} \tag{5.5}$$

Figure 5.4 shows the radiofrequency versus magnetic field experimental points in the case of the magnetic field being oriented parallel to the molecular ring (left) and in the case of the magnetic field being aligned to the crystallographic $c$-axis (right). The red straight lines show the theoretical predictions obtained by assuming $A_{\rm cp} = -10,96$ Tesla in both configurations and the constant value $g\langle s\rangle = -0,67$ and $g\langle s\rangle = -1,07$ for Cr 2, Cr 4 and Cr 6 in $Cr_7Ni$ in the magnetic field range 4 - 8 Tesla in the case of the magnetic field being oriented parallel and perpendicular to the molecular ring respectively. The black curves represent the theoretical predictions obtained by assuming $A_{\rm cp} = -10,96$ Tesla in both configurations and the local spin expectation values shown in figure 1.16 corresponding to the calculation at $T = 1,5$ K.

Figure 5.5 shows the same experimental points: in this case the theoretical predictions are obtained by assuming the value $A_{\rm cp} = -12,38 \pm 0,23$ Tesla corresponding to the core polarization constant experimentally determined by means of the sum rule 4.3 in $Cr_7Cd$ [21] (see equation 4.4 in section 4.1). By comparing figure 5.4 and 5.5 it appears that the agreement is better for the lower value of the core polarization constant given by equation 5.5. However the value $A_{\rm cp} = -12,38 \pm 0,23$ Tesla should be more reliable since it has been obtained without any assumption about the local spin density $g\langle s\rangle$ [21]. In this scenario the discrepancy between the experimental data and the theoretical predictions in figure 5.5 could be due to the imprecision in the sample orientation [4]. It should also be remarked that the experimental value $A_{\rm cp} = -12,38 \pm 0,23$ Tesla/Bohr magneton in equation 4.4 is in striking

[4] The core polarization constant does not depend on the sample orientation, viceversa the electronic magnetic moments expectation values are affected by the orientation of the sample with respect to the applied magnetic field.

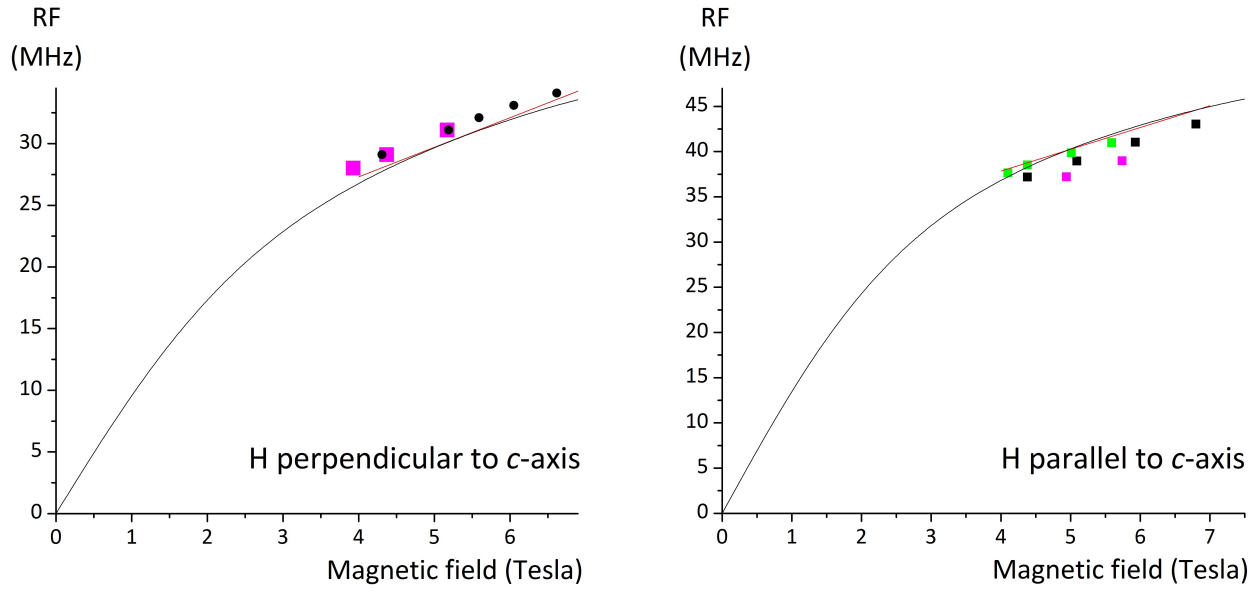


Figure 5.4: $^{53}$Cr-NMR of a $Cr_7Ni$ single crystal at $T = 1.6$ K: radiofrequency versus applied field experimental points. Left: The magnetic field is applied perpendicular to the crystallographic $c$-axis namely parallel to the molecular ring. Right: The magnetic field is applied parallel to the crystallographic $c$-axis namely perpendicular to the molecular ring. The red straight lines show the theoretical predictions obtained by assuming $A_{cp} = -10,96$ Tesla in both configurations and the constant value $g\langle s\rangle = -0,67$ and $g\langle s\rangle = -1,07$ for Cr 2, Cr 4 and Cr 6 in $Cr_7Ni$ in the magnetic field range 4 - 8 Tesla in the case of the magnetic field being oriented parallel and perpendicular to the molecular ring respectively. The black curves represent the theoretical predictions obtained by assuming $A_{cp} = -10,96$ Tesla in both configurations and the local spin expectation values shown in figure 1.16 corresponding to the calculation at $T = 1,5$ K.

agreement with the value $A_{cp} = -12,5$ Tesla/Bohr magneton obtained theoretically for an unpaired $3d$ electron [19], [20] (see Appendix A.1). This agreement indicates that the $3d$ electrons in the $Cr^{3+}$ ion in $Cr_7Ni$ are well localized on the magnetic ion.

Figure 5.6 shows the radiofrequency versus magnetic field theoretical curves for the three inquivalent $^{53}$Cr sites in $Cr_7Ni$ for both field orientations at $T = 1,5$ K. These theoretical predictions are obtained according to equation 5.1 by assuming the calculated values of the local electronic magnetic moments at $T = 1,5$ K shown in figure 1.16 and the value $A_{cp} = -12,38 \pm 0,23$ Tesla experimentally determined for $Cr_7Cd$ (see section 4.1). It is worthwhile observing that only one signal out of the three expected signals has been detected. As stated above, this signal has been assigned to the Cr 2 - Cr 4 and Cr 6 nuclear sites. In the magnetic field range 4 - 8 Tesla the Cr 1 - Cr 7 and Cr 3 - Cr 5 signals are expected to appear at very low frequencies: 16 - 6 MHz in the case of the magnetic field being applied parallel to the molecular ring and 26 - 18 MHz in the case of the field being directed perpendicular to the molecular ring. The electronic instrumentation constituting the NMR spectrometer is not optimized for working at such low frequencies and in these experiments the signal could not be distinguished from the noise.

The observation of the signal at low fields, permitting the use of radiofrequencies as high as required for the instrumentation proper work, appears to be possible at temperatures below 100 mK

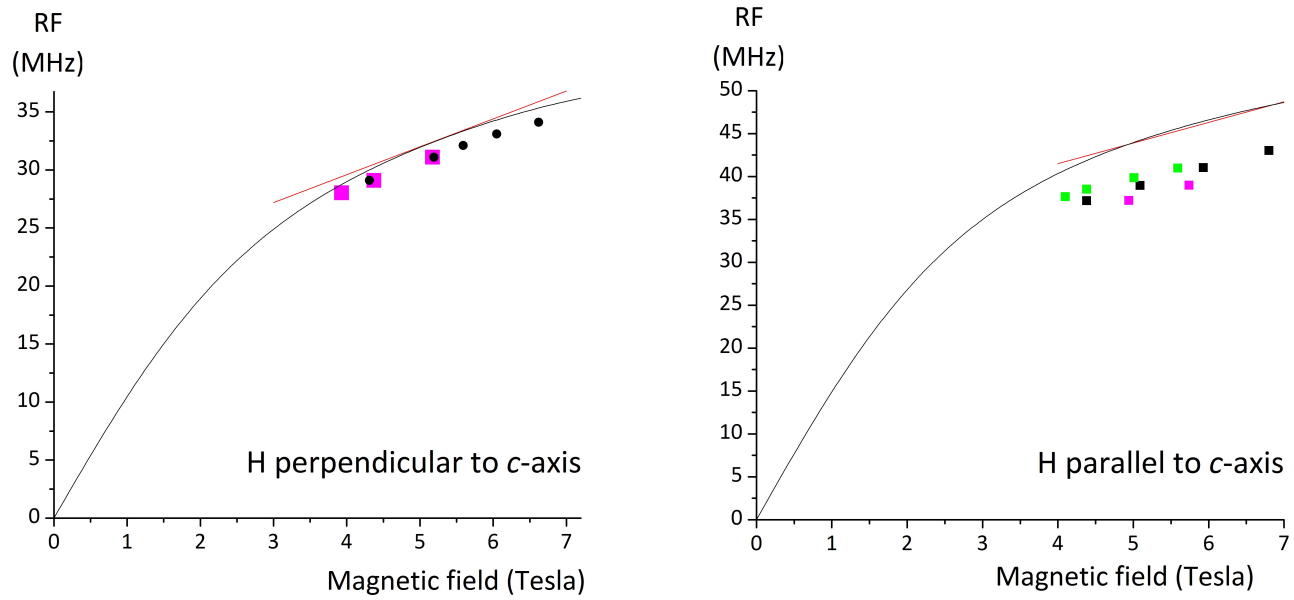


Figure 5.5: $^{53}$Cr-NMR of a $Cr_7Ni$ single crystal at $T = 1.6$ K: radiofrequency versus applied field experimental points. Left: The magnetic field is applied perpendicular to the crystallographic $c$-axis namely parallel to the molecular ring. Right: The magnetic field is applied parallel to the crystallographic $c$-axis namely perpendicular to the molecular ring. The red straight lines show the theoretical predictions obtained by assuming $A_{cp} = -12,38$ Tesla in both configurations and the constant value $g\langle s\rangle = -0,67$ and $g\langle s\rangle = -1,07$ for Cr 2, Cr 4 and Cr 6 in $Cr_7Ni$ in the magnetic field range 4 - 8 Tesla in the case of the magnetic field being oriented parallel and perpendicular to the molecular ring respectively. The black curves represent the theoretical predictions obtained by assuming $A_{cp} = -12,38$ Tesla in both configurations and the local spin expectation values shown in figure 1.16 corresponding to the calculation at $T = 1,5$ K.

as shown in figure 5.7. This figure displays the radiofrequency versus magnetic field theoretical curves for the three inquivalent $^{53}$Cr sites in $Cr_7Ni$ for both field orientations at $T = 0$ K. These theoretical plots are obtained according to equation 5.1 by assuming the calculated values of the local electronic magnetic moments at $T = 0$ K reported in figure 1.15 and the experimentally determined value $A_{cp} = -12,38 \pm 0,23$ Tesla. These curves show that at very low temperatures the Cr 1 - Cr 7 and Cr 3 - Cr 5 radiofrequency versus magnetic field plots increase monotonically with decreasing field. Many attempts at temperatures as low as 100 mK have been done by means of the dilution refrigerator of the experimental equipment labelled "set-up 2" descrbed in section 2.6. However no $^{53}$Cr signal has been detected down to 0,1 K probably due to the dilution refrigerator NMR probe low sensitivity [5].

[5] Cr 2 - Cr 4 - Cr 6 signal could only be detected by means of "set-up 1" and this measurement has been repeated in order to test its reproducibility. No $^{53}$Cr signal has ever been detected by means of "set-up 2" in $Cr_7Ni$.

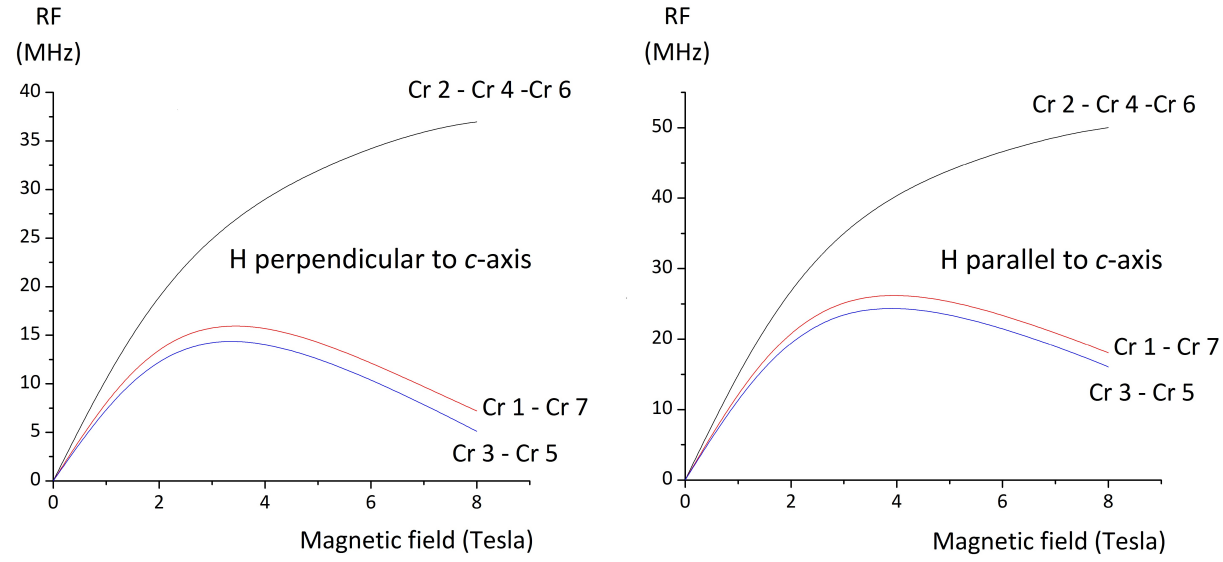


Figure 5.6: $^{53}$Cr-NMR of a $Cr_7Ni$ single crystal at $T = 1.6$ K: theoretical predictions according to equation 5.1 obtained by assuming the calculated values of the local electronic magnetic moments at $T = 1, 5$ K shown in figure 1.16 and the value $A_{cp} = -12, 38$ Tesla experimentally determined for $Cr_7Cd$ (see section 4.1). Left: The magnetic field is applied perpendicular to the crystallographic $c$-axis namely parallel to the molecular ring. Right: The magnetic field is applied parallel to the crystallographic $c$-axis namely perpendicular to the molecular ring.

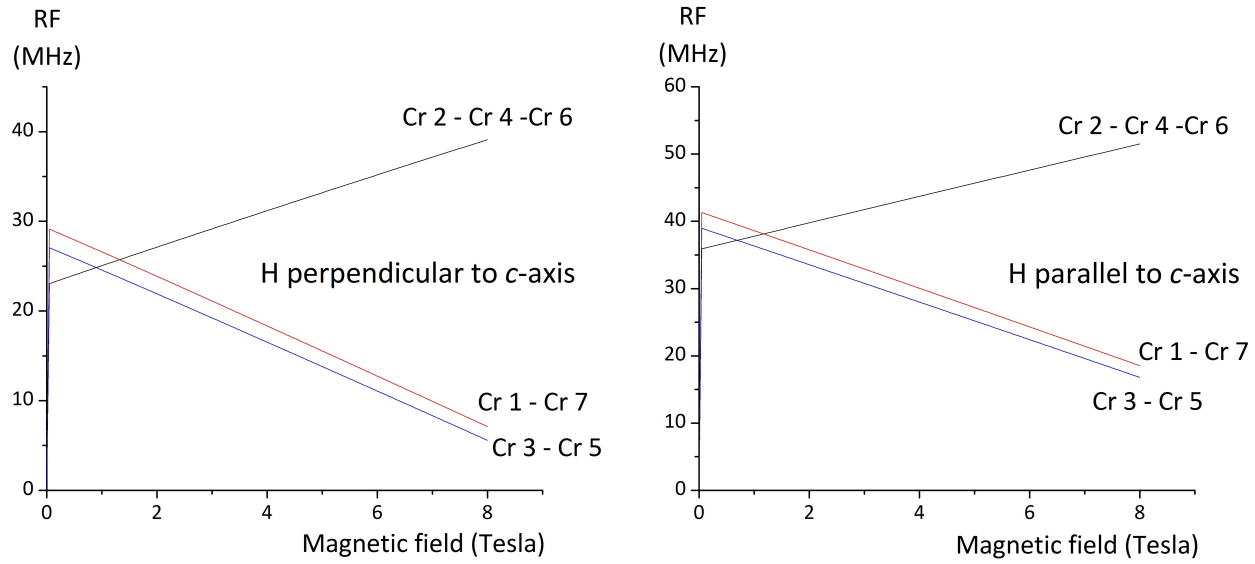


Figure 5.7: $^{53}$Cr-NMR of a $Cr_7Ni$ single crystal at $T = 0$ K: theoretical predictions according to equation 5.1 obtained by assuming the calculated values of the local electronic magnetic moments at $T = 0$ K shown in figure 1.15 and the value $A_{cp} = -12, 38$ Tesla experimentally determined for $Cr_7Cd$ (see section 4.1). Left: The magnetic field is applied perpendicular to the crystallographic $c$-axis namely parallel to the molecular ring. Right: The magnetic field is applied parallel to the crystallographic $c$-axis namely perpendicular to the molecular ring.

## 5.2 $^{19}$F-NMR

As part of the present work, $^{19}$F-NMR measurements in $Cr_7Ni$ single crystals have been performed at Ames Laboratory [6]. The interpretation of the $^{19}$F-NMR spectra in $Cr_7Ni$ is not trivial since the fluoride ions are bridging ligands located approximatively half way between two magnetic ions. Each $^{19}$F signal shift is therefore affected by the isotropic transferred and by the anisotropic transferred hyperfine terms (see equation 2.32) producing complicated spectral structures. Nevertheless $^{19}$F-NMR measurements can provide useful information concerning the order of magnitude of the $^{19}$F - $Cr^{3+}$ and $^{19}$F - $Ni^{2+}$ transferred hyperfine constant, to be compared to the value determined in $Cr_7Cd$ (see section 4.2) relating to the $F^-$ - $Cr^{3+}$ bonds at the sites close to the $Cd^{2+}$ ion and in $KMnF_3$ and $MnF_2$ relating to $F^-$ - $Mn^{2+}$ bonds (see Appendix A).

The present section has the purpose of describing the determination of the value of the $^{19}$F - $Ni^{2+}$ transferred hyperfine constant in $Cr_7Ni$ by means of $^{19}$F-NMR measurements. Also, the experimental determination of the order of magnitude of the $^{19}$F - $Cr^{3+}$ transferred hyperfine constant is described in the third part of this section together with a brief discussion of the factors that make this determination not precise. An attempt of direct fitting the $^{19}$F-NMR spectrum by means of a superposition of Lorentzian curves accounting for non equivalent $^{19}$F nuclear sites and for the Teflon $^{19}$F signal is presented in the last part of the present section.

### 5.2.1 General features

Field-sweep $^{19}$F-NMR spectra have been collected in $Cr_7Ni$ single crystals according to the procedure described in section 2.6.2. The measurements have been performed at $T \sim 1,6$ K by means of the experimental equipment labelled "set-up 1" in section 2.6. Figure 5.8 shows the spectra that have been collected at different radiofrequency values by applying the magnetic field parallel to the crystallographic $c$-axis namely perpendicular to the molecular ring. In each spectrum the large signal with a negative shift is due to the $^1$H resonance [$\gamma(^1\text{H}) = 42,5756$ MHz/Tesla]. The large and narrow non shifted signal is due to the Teflon (Polytetrafluoroethilene) tape present in the co-axial cable. The sample's $^{19}$F-NMR spectra are shown in the insert of figure 5.8. The $^{19}$F-NMR spectrum is composed of a slightly shifted broad structure and of a positively shifted weak signal. Figure 5.9 refers to the case of the magnetic field being applied perpendicular to the crystallographic $c$-axis namely parallel to the molecular ring.

$Cr_7Ni$ $^{19}$F-NMR spectra have been studied based on the following argument [7]. Analogous to the $^{19}$F-NMR spectra in $Cr_7Cd$ we observe that each $^{19}$F signal shows an NMR shift due to the intracluster interactions with the magnetic $Ni^{2+}$ and $Cr^{3+}$ ions. As for the case of $Cr_7Cd$ in section 4.2, assumption is made that the hyperfine field produced by the magnetic ions at a given $^{19}$F nuclear site consists essentially of two terms as shown schematically in figure 5.10. The far away magnetic ions produce a classical dipolar hyperfine field at the $^{19}$F nucleus. This term is inherently anisotropic and can be calculated within the point-dipole approximation by means of equation 2.27. The calculation yields hyperfine fields at the nuclear sites whose order of magnitude is $10^{-3} \div 10^{-2}$ Tesla. This is the same order of magnitude obtained in the case of $Cr_7Cd$ in section 4.2. This contribution can be neglected as

[6] Department of Physics and Astronomy, Ames Laboratory, Iowa State University, Ames, IA.

[7] The present discussion refers to the labelling and to the interactions diagram shown in figure 5.10.

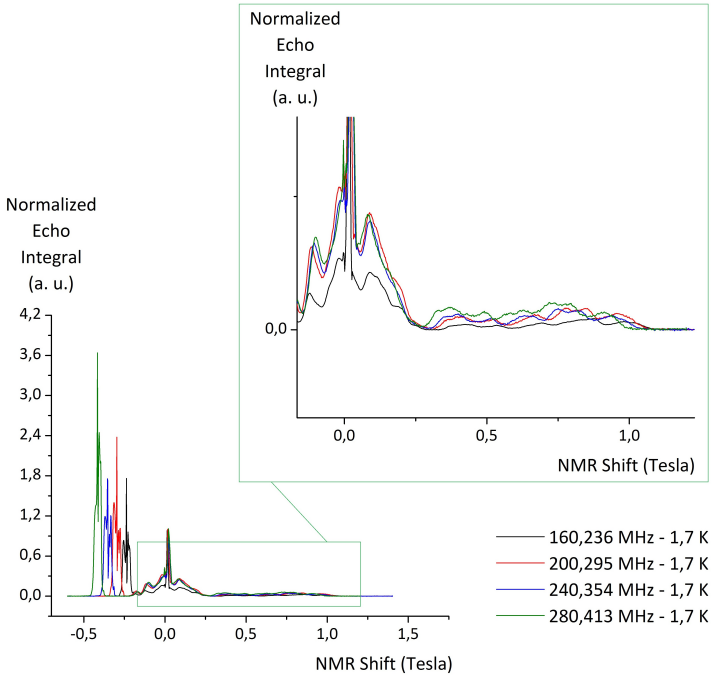


Figure 5.8: $^{19}$F-NMR field sweep spectra in $Cr_7Ni$ at $T = 1,6$ K. The magnetic field is applied parallel to the crystallographic $c$-axis namely perpendicular to the molecular ring. The large signal with a negative shift is due to the $^1$H resonance. The $^{19}$F-NMR signal has been zoomed in and shown in the insert.

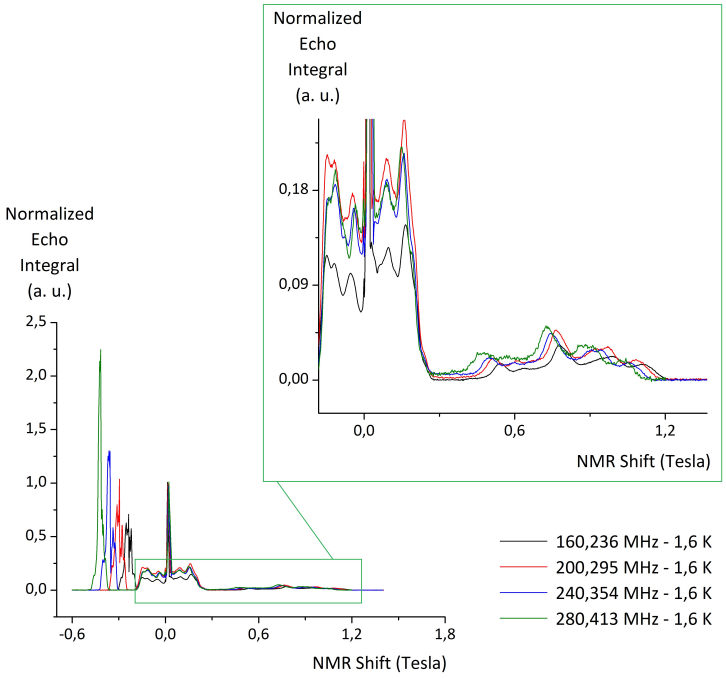


Figure 5.9: $^{19}$F-NMR field sweep spectra in $Cr_7Ni$ at $T = 1,6$ K. The magnetic field is applied perpendicular to the crystallographic $c$-axis namely parallel to the molecular ring. The large signal with a negative shift is due to the $^1$H resonance. The $^{19}$F-NMR signal has been zoomed in and shown in the insert.

the main spectral features show shifts whose order of magnitude is $\sim 10^{-1}$ Tesla. On the other hand we assume that the contribution to the hyperfine field at the $^{19}$F nuclear site due to the neighboring magnetic ions can be described by means of a transferred hyperfine interaction term (see equation 2.32). The anisotropic tranferred terms $A_\sigma$ and $A_\pi$ in equation 2.32 are responsible for the angular dependence of the spectra. However, the separate determination of the constants $A_\iota$, $A_\sigma$ and $A_\pi$ from the spectra is a difficult problem that requires the detailed study of the molecular orbitals involved in the $Cr^{3+}$ - $F^-$ coordinative bond: this goes beyond the scope of this work. The present analysis therefore deals with the overall hyperfine transferred coupling constant given by equation 2.32.

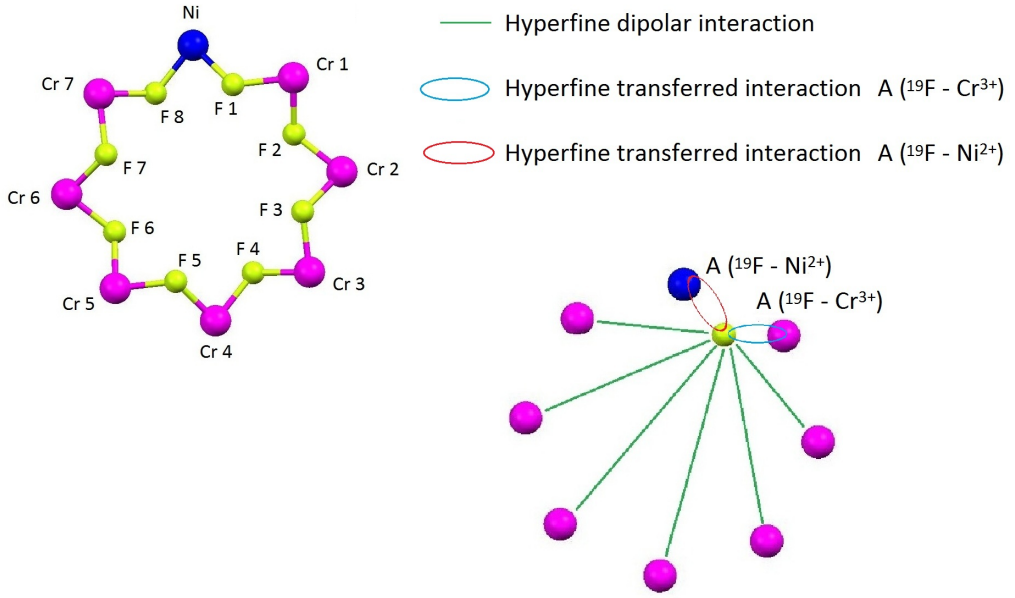


Figure 5.10: Labelling of the $^{19}$F nuclear sites and of $Cr^{3+}$ magnetic ions in $Cr_7Ni$ molecular ring (left). Schematic diagram of the interactions giving rise to the hyperfine field at a given $^{19}$F nuclear site (right).

Assumption is made that the NMR frequency $\nu$ of the $^{19}$F nuclear sites far away from the $Ni^{2+}$ magnetic ion i. e. F 2, F 3, F 4, F 5, F 6 and F 7, according to the usual labelling shown in figure 5.10, can be described by the equation:

$$\nu = \frac{\gamma}{2\pi} H + \frac{\gamma}{2\pi} A_{(^{19}\mathrm{F}-\mathrm{Cr}^{3+})} \sum_i g\langle s\rangle_{\mathrm{Cr},i} \tag{5.6}$$

where $\frac{\gamma}{2\pi}$ is the $^{19}$F gyromagnetic ratio equal to 40,059 MHz/Tesla, $H$ is the applied magnetic field and $A_{(^{19}\mathrm{F}-\mathrm{Cr}^{3+})}$ represents the $^{19}\mathrm{F} - \mathrm{Cr}^{3+}$ transferred hyperfine constant. In equation 5.6 the sum extends over the two $Cr^{3+}$ ions neighbouring to the $^{19}$F nucleus producing the signal. Assumption is made that the two bonds involving a fluoride $F^-$ anion and its neighbouring $Cr^{3+}$ magnetic ions are characterized by the same transferred hyperfine constant, i. e. any difference in the values of the angles $\theta_\sigma$ and $\theta_\pi$ (see equation 2.32) is being neglected. $g\langle s\rangle_{\mathrm{Cr},i}$ is the component directed along the applied field of the $i^{th}$ $Cr^{3+}$ ion electronic magnetic moment expressed in Bohr magnetons. As mentioned in section 1.2.2, due to the simmetry of the magnetic Hamiltonian, if the magnetic field is applied perpendicular or parallel to the molecular ring, the local spin magnetic moments are directed along the applied field. As stated above, equation 5.6 holds for the $^{19}$F nuclear sites far away from the

$Ni^{2+}$ magnetic ion. These fluoride ions are bridging ligands located approximatively half-way between two antiparallel $Cr^{3+}$ magnetic moments. The vectorial sum of the hyperfine fields produced by these moments at the $^{19}F$ nucleus results in a small local field yielding a small NMR shift. We therefore conclude that the slightly shifted structure of the $^{19}F$ spectra can be assigned to these nuclear sites.

Viceversa the $^{19}F$ nuclei neighboring to the $Ni^{2+}$ magnetic ion, namely F 1 and F 8, show a resonance frequency described by:

$$\nu = \frac{\gamma}{2\pi}H + \frac{\gamma}{2\pi}A_{(^{19}\mathrm{F}-\mathrm{Cr}^{3+})}g\langle s\rangle_{\mathrm{Cr}_{1,7}} + \frac{\gamma}{2\pi}A_{(^{19}\mathrm{F}-\mathrm{Ni}^{2+})}g\langle s\rangle_{\mathrm{Ni}} \tag{5.7}$$

where $g = 1,98$ for $Cr^{3+}$ and 2,2 for $Ni^{2+}$ is the electronic Landé factor, $A_{(^{19}\mathrm{F}-\mathrm{Cr}^{3+})}$ is the transferred $^{19}F$ - $Cr^{3+}$ hyperfine constant relating to the site neighboring to the $Ni^{2+}$ ion and $\langle s\rangle_{\mathrm{Cr}_{1,7}}$ is the component of the electronic spin local expectation value at sites 1 and 7 aligned to the applied field. Analogous definitions hold for $A_{(^{19}\mathrm{F}-\mathrm{Ni}^{2+})}$ and $\langle s\rangle_{\mathrm{Ni}}$.

It is worthwhile observing that according to Table 5.1 $Cr^{3+}_{1,7}$ and $Ni^{2+}$ magnetic moments are antiparallel and their moduli are appreciably different. We thus assign to the $^{19}F$ nuclei neighboring to the $Ni^{2+}$ ion i. e. F1 and F8 the most shifted NMR signal. Based on this assumption it is possible to determine the value of the $^{19}F$ - $Ni^{2+}$ transferred hyperfine constant once the $A_{(^{19}\mathrm{F}-\mathrm{Cr}^{3+})}$ value is known. The following section illustrates the procedure leading to the $A_{(^{19}\mathrm{F}-\mathrm{Ni}^{2+})}$ determination.

### 5.2.2 Experimental determination of the $^{19}F$ - $Ni^{2+}$ transferred hyperfine constant

The purpose of the present section is to describe the determination of the $A_{(^{19}\mathrm{F}-\mathrm{Ni}^{2+})}$ transferred hyperfine constant. It is worthwhile stressing that equation 5.7 describing the F 1 and F 8 NMR frequency can be used in order to determine the $A_{(^{19}\mathrm{F}-\mathrm{Ni}^{2+})}$ value once the magnetic moments $g\langle s\rangle$ and the $A_{(^{19}\mathrm{F}-\mathrm{Cr}^{3+})}$ value are known and by assuming that F 1 and F 8 resonance results in the most shifted spectral feature observed in the experiments.

Assumption is made that the intermediate value $A = -0,320 \pm 0,005$ Tesla determined in section 4.2 in $Cr_7Cd$ (see equation 4.7) can be used in equation 5.7 to describe the F 1 - Cr 1 and F 8 - Cr 7 transferred hyperfine interaction in $Cr_7Ni$ (see figure 5.10). It is worthwhile observing that the value $A = -0,320 \pm 0,005$ Tesla refers in $Cr_7Cd$ to the $^{19}F$ sites that are close to the $Cd^{2+}$ ion. Equation 5.7 describing the F 1 and F8 sites resonance frequency can be rewritten as follows:

$$\nu = 40,059\ \mathrm{MHz/Tesla} \cdot H + C \tag{5.8}$$

where:

$$C = 40,059\ \mathrm{MHz/Tesla} \cdot [(-0,320 \pm 0,005)\ \mathrm{Tesla} \cdot g\langle s\rangle_{\mathrm{Cr}_{1,7}} + A_{(^{19}\mathrm{F}-\mathrm{Ni}^{2+})} \cdot g\langle s\rangle_{\mathrm{Ni}}]. \tag{5.9}$$

Equations 5.8 and 5.9 provide the F 1 and F 8 nuclear sites NMR frequency dependence on the applied field. The radiofrequency shows a linear dependence on the magnetic field and the intercept $C$ value yields the hyperfine constant $A_{(^{19}\mathrm{F}-\mathrm{Ni}^{2+})}$ value, once the magnetic moments $g\langle s\rangle_{\mathrm{Cr}_{1,7}}$ and $g\langle s\rangle_{\mathrm{Ni}}$ are known. Figure 5.11 (left) shows the $^{19}F$-NMR field sweep spectra at different radiofrequency values (the same spectra are shown in figure 5.8) in the case of the magnetic field being applied parallel to the crystallographic $c$-axis. The shifted signal assigned to F 1 and F 8 nuclear sites is identified by means

of a vertical line in each spectrum. It is worthwhile observing that even if F 1 and F 8 are (almost) equivalent nuclear sites, the shifted signal assigned to these nuclei shows a complicated structure. In this scenario assumption is made that the experimentally observed structure is due to some degree of mosaicity of the sample i. e. the sample consists of regions showing different orientations of the crystallographic axes with respect to an external frame of reference. Figure 5.11 (right) displayes the radiofrequency versus applied field plot referring to the shifted signal together with the best fit curve according to equation 5.8. Figure 5.12 refers to the case of the magnetic field being applied perpendicular to the crystallographic $c$-axis.

The fitting procedure by means of a function of the type in equation 5.8 yields $C = -32,1 \pm 1,5$ MHz and $C = -30,1 \pm 0,4$ MHz in the case of the magnetic field applied parallel and perpendicular to the crystallographic $c$-axis respectively. Equation 5.9 yields :

$$A_{(^{19}\mathrm{F}-\mathrm{Ni}^{2+})} \sim 0,5 \text{ Tesla} \tag{5.10}$$

in the case of the field being applied parallel to the crystallographic $c$-axis and:

$$A_{(^{19}\mathrm{F}-\mathrm{Ni}^{2+})} \sim 0,96 \text{ Tesla} \tag{5.11}$$

in the case of the magnetic field being applied perpendicular to the crystallographic $c$-axis. These results have been obtained by assuming the values of the electronic magnetic moments reported in Table 5.1. These values dependence on the magnetic field has been neglected: in fact according to figure 1.16 in section 1.2.2, the electronic spin moments dependence on the magnetic field is very small in the range of operation 4 - 8 Tesla.

It is worthwhile stressing that the values reported in equation 5.10 and 5.11 are estimates of the overall $^{19}$F - $Ni^{2+}$ hyperfine transferred term. This results are not accurate due to the fact that the value assumed for the $^{19}$F - $Cr^{3+}$ hyperfine transferred term namely the value $A = -0,320 \pm 0,005$ Tesla obtained in $Cr_7Cd$ does not refer to the same sample orientation. Also, the values reported in equation 5.10 and 5.11 include both the isotropic and the anisotropic transferred hyperfine terms. As observed above, the separate determination of the isotropic and anisotropic $\sigma$ and $\pi$ contribution requires the detailed knowledge of the angles $\theta_\sigma$ and $\theta_\pi$ between the directional $p_\sigma$ and $p_\pi$ bonds and the applied magnetic field direction for each $^{19}$F site (see equation 2.32) and goes beyond the scope of the present work.

### 5.2.3 Experimental determination of the $^{19}$F - $Cr^{3+}$ transferred hyperfine constant

In section 5.2.1 we pointed out that the NMR shift in $Cr_7Ni$ $^{19}$F-NMR spectra is essentially due to the transferred hyperfine field produced by the neighboring magnetic ions at the $^{19}$F nuclear sites. Viceversa the classical dipolar hyperfine contribution can be neglected. Based on these assumptions the NMR frequency of the $^{19}$F nuclei has been derived. Equation 5.6 holds for the $^{19}$F nuclei that are far away from the $Ni^{2+}$ ion producing the slightly shifted broad spectral structure observed in the experiments. On the other hand equation 5.7 describes the resonance frequency of the $^{19}$F nuclear sites neighboring to the $Ni^{2+}$ ion namely F 1 and F 8, producing the shifted weak signal. The detailed analysis of this latter signal has been carried on in section 5.2.2 and the variation range of the $^{19}$F

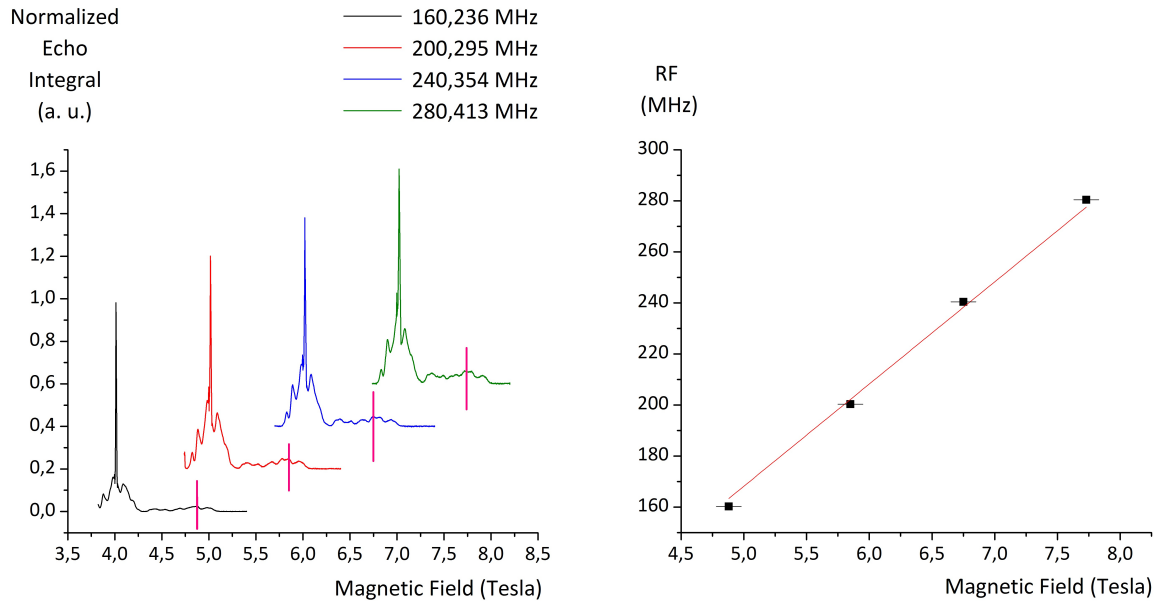


Figure 5.11: Left: $^{19}$F-NMR field sweep spectra of a $Cr_7Ni$ single crystal at $T = 1{,}6$ K at different radiofrequency values. The magnetic field is applied parallel to the crystallographic $c$-axis namely perpendicular to the molecular ring. The shifted signal assigned to F 1 and F 8 nuclear sites is identified by means of a vertical line in each spectrum. Right: the radiofrequency versus applied field plot referring to the shifted signal identified in the spectra on the left. The best fit line according to the equation $y = C + 40,059 \cdot x$ is also shown. The fitting procedure yields $C = -32,1 \pm 1,5$ MHz.

- $Ni^{2+}$ transferred hyperfine constant value has been determined. The present section illustrates the analogous analysis of the slightly shifted structure yielding useful information about the $^{19}$F - $Cr^{3+}$ transferred hyperfine constant order of magnitude.

Equation 5.6 describing the resonance frequency of the $^{19}$F nuclear sites that are far away from the $Ni^{2+}$ ion namely F 2, F 3, F 4, F 5, F 6, F 7 is here rewritten for convenience:

$$\nu = \frac{\gamma}{2\pi} H + \frac{\gamma}{2\pi} A_{(^{19}\mathrm{F}-\mathrm{Cr}^{3+})} \sum_i g\langle s\rangle_{\mathrm{Cr},i}. \tag{5.12}$$

This equation shows that the NMR frequency of these $^{19}$F nuclei shows a linear dependence on the applied field according to:

$$\nu = 40,059 \text{ MHz/Tesla} \cdot H + C \tag{5.13}$$

where:

$$C = 40,059 \text{ MHz/Tesla} \cdot A_{(^{19}\mathrm{F}-\mathrm{Cr}^{3+})} \sum_i g\langle s\rangle_{\mathrm{Cr},i}. \tag{5.14}$$

As observed above since the fluoride anions far away from $Ni^{2+}$ are bridging ligands located approximatively half way between two antiparallel $Cr^{3+}$ magnetic moments, the resulting $^{19}$F-NMR shift is small and the slightly shifted structure can be assigned to these six $^{19}$F nuclear sites. However this structure consists of many partially overlapping peaks and the unambiguous assignment of each peak to any of the $^{19}$F nuclei listed above appears not to be possible.

Figure 5.13 shows the $Cr_7Ni$ $^{19}$F-NMR field sweep spectra collected at different radiofrequency values by applying the magnetic field parallel to the crystallographic $c$-axis. Five slightly shifted

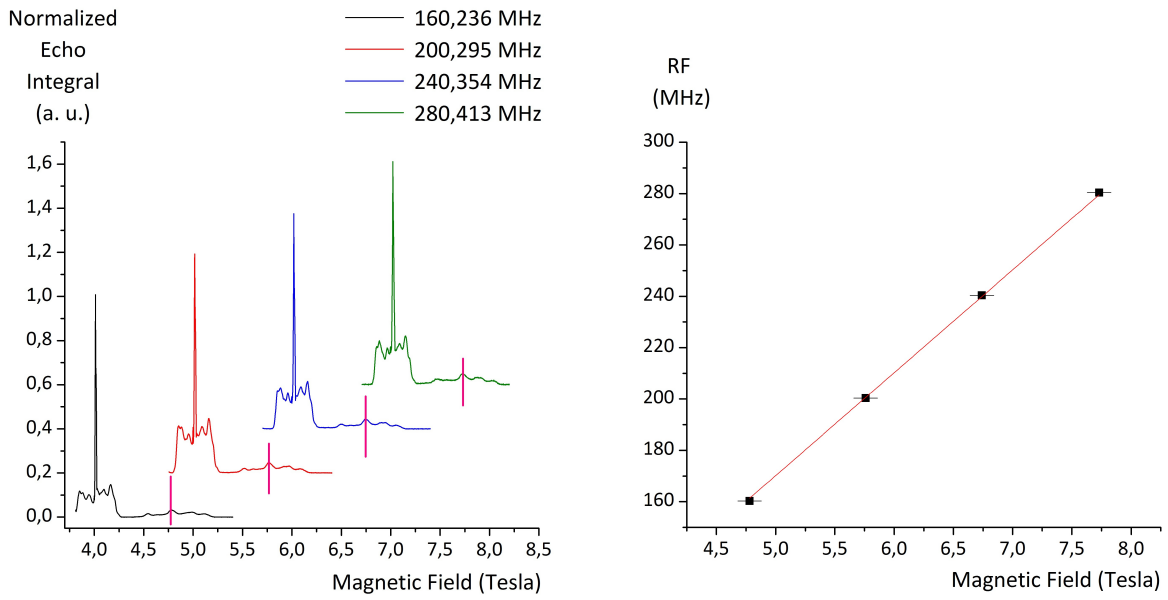


Figure 5.12: Left: $^{19}$F-NMR field sweep spectra of a $Cr_7Ni$ single crystal at $T = 1{,}6$ K at different radiofrequency values. The magnetic field is applied perpendicular to the crystallographic $c$-axis namely parallel to the molecular ring. The shifted signal assigned to F 1 and F 8 nuclear sites is identified by means of a vertical line in each spectrum. Right: the radiofrequency versus applied field plot referring to the shifted signal identified in the spectra on the left. The best fit line according to the equation $y = C + 40,059 \cdot x$ is also shown. The fitting procedure yields $C = -30,1 \pm 0,4$ MHz.

peaks have been identified. It seems reasonable that a sixth signal exist, superimposed to one of the identified peaks or to the Taflon tape $^{19}$F signal. These peaks show an NMR shift whose order of magnitude is $10^{-1}$ Tesla. Figure 5.15 shows the radiofrequency versus applied field plots referring to the five slightly shifted peaks identified in figure 5.13. The best fit lines according to the expression $y = C + 40,059 \cdot x$ (equation 5.13) are also shown. The fitting procedure yields the $C$ values reported in Figure 5.15 and in Table 5.2 representing the NMR shift of non equivalent $^{19}$F nuclear sites, according to equation 5.13 and 5.14.

The term $\sum_i g\langle s\rangle_{\mathrm{Cr},i}$ in equation 5.14, where the sum extends over the two $Cr^{3+}$ ions neighboring to the $^{19}$F nucleus producing the signal, can be calculated by means of the values reported in Table 5.1 in the case of the magnetic field being applied parallel to the $c$-axis. This term equals $0,12 \div 0,18$ depending on which bridging $^{19}$F site we are considering: as stated above, the unambiguous assignment of each NMR shift to any of the $^{19}$F sites far away from the $Ni^{2+}$ ion is not possible. The range of variation $\sum_i g\langle s\rangle_{\mathrm{Cr},i} = 0,12 \div 0,18$ produces peaks showing different shifts. Furthermore it is worthwhile stressing that the large variation range of the $C$ values and the fact that both positive and negative $C$ values have been obtained suggests that the anisotropic transferred terms in equation 2.32 largely affect the NMR shift. The anisotropic contribution to the transferred constant is given by the following expression (see equation 2.32):

$$A_\sigma(3\cos^2\theta_\sigma - 1) + A_\pi(3\cos^2\theta_\pi - 1)$$

where $\theta_\sigma$ is the angle between the directional $p_\sigma$ bonds and the applied magnetic field direction while

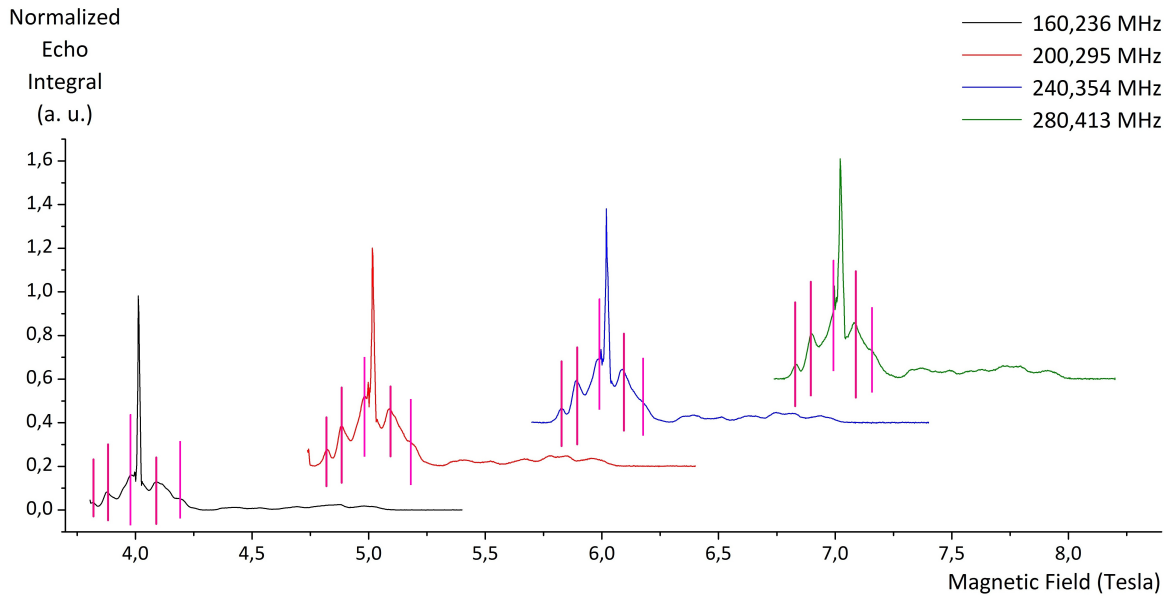


Figure 5.13: $^{19}$F-NMR field sweep spectra of a $Cr_7Ni$ single crystal at $T = 1{,}6$ K at different radiofrequency values. The magnetic field is applied parallel to the crystallographic $c$-axis namely perpendicular to the molecular ring. Five peaks composing the slightly shifted structure have been identified by means of vertical lines in each spectrum.

$\theta_\pi$ is the angle between the directional $p_\pi$ bonds and the applied field direction. Figure 5.14 suggests that the six $^{19}$F sites far away from the $Ni^{2+}$ ion can give rise to different anisotropic terms thus resulting in different NMR shifts.

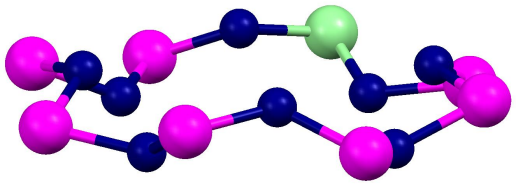

Figure 5.14: $Cr_7Ni$ molecular ring. Blue: Fluorine, Magenta: Chromium, Green: Nickel. Carbonium, Oxygen and Hydrogen atoms are not shown.

The separate determination of the isotropic $A_t$ and anisotropic $A_\sigma$ and $A_\pi$ contributions to the transferred hyperfine coupling is a difficult issue that goes beyond the purpose of the present work. Nevertheless a naive estimate of the overall transferred constant, including the isotropic and the anisotropic contributions can be performed by considering each $C$ value separately. For example, if we assume that $\sum_i g\langle s\rangle_{\mathrm{Cr},i}$ equals to the intermediate value 0,15, the results reported in Table 5.2 are obtained. These values have the same order of magnitude of the results in $KMnF_3$ and $MnF_2$ [8] described in Appendix A. It is worthwhile stressing that the values reported in Table 5.2 represent

[8] In these compounds the separate determination of the isotropic component has been performed.

Table 5.2: The $C$ values reported in figure 5.15 and expressed in MHz and the corresponding $^{19}$F - $Cr^{3+}$ overall transferred hyperfine constants expressed in Tesla per Bohr magneton.

| $C$ | $A$ |
|---|---|
| $+7,1 \pm 0,1$ | $+1,18 \pm 0,02$ |
| $+4,5 \pm 0,2$ | $+0,75 \pm 0,03$ |
| $+0,7 \pm 0,1$ | $+0,12 \pm 0,02$ |
| $-3,5 \pm 0,1$ | $-0,58 \pm 0,02$ |
| $-7,1 \pm 0,3$ | $-1,18 \pm 0,02$ |

the overall transfered constant according to equation 2.32, here rewritten for convenience:

$$A_t + A_\sigma(3\cos^2\theta_\sigma - 1) + A_\pi(3\cos^2\theta_\pi - 1). \tag{5.15}$$

As for the case of the $^{19}$F - $Ni^{2+}$ transferred hyperfine interaction we observe that in order to evaluate the separate $A_t$, $A_\sigma$ and $A_\pi$ contributions one should be able to determine the values of the angles $\theta_\sigma$ and $\theta_\pi$ between the directional $p_\sigma$ and $p_\pi$ bonds and the applied magnetic field direction for each $^{19}$F site. This requires the detailed study of the molecular orbitals involved in the $Cr^{3+}$ - $F^-$ coordinative bond and goes beyond the scope of the present work.

### 5.2.4 Attempt of direct fitting a $^{19}$F-NMR spectrum in $Cr_7Ni$

A large number of attempts of direct fitting the well-resolved $^{19}$F-NMR $Cr_7Ni$ spectra shown in section 5.2.1, 5.2.2 and 5.2.3 has been done. Most attempts have been performed by means of fitting curves consisting of the sum of eight Gaussian peaks accounting for the sample $^{19}$F sites signals and one Gaussian curve accounting for the Teflon tape $^{19}$F signal but no convergence has been obtained. Analogous attempts have been tried by using Lorentzian shaped peaks. Also, attempts by means of fitting curves consisting of four Gaussian or Lorentzian curves and one peak accounting for the Teflon tape $^{19}$F signal have been done. None of these procedures has succeded.

Somehow better fitting results have been obtained by using the poorly resolved spectrum shown in the insert of figure 5.16. This spectrum has been fitted by means of the following expression:

$$y = \frac{2A_{\mathrm{T}}}{\pi}\frac{w_{\mathrm{T}}}{4(x - x_{c,\mathrm{T}})^2 + w_{\mathrm{T}}^2} + \sum_{i=1}^{3}\frac{2A_i}{\pi}\frac{w_i}{4(x - x_{c,i})^2 + w_i^2} \tag{5.16}$$

namely the superposition of a Lorentzian peak accounting for the Teflon tape $^{19}$F signal and of three Lorentzian curves accounting for the sample's $^{19}$F signals. The fitting parameters $A$, $w$ and $x_c$ represent the integral, the full width at half maximum (FWHM) and the center of each Lorentzian distribution. Figure 5.16 shows the spectrum (black) and the fitting curve (red).

The fitting parameters are listed in Table 5.3: the centers of the distributions have been set as fixed parameters according to the NMR shifts observed in the spectrum. Viceversa the areas and the widths have been determined by the fitting procedure. It is worthwhile observing that due to the poor

resolution of this spectrum, extremely high FWHM values have ben obtained. Also, the integrals of the Lorentzian peaks are approximatively in the ratio 4:2:1 while the ratio 4:2:2 is expected based on the fact that the peak's area is proportional to the number of nuclei producing the signal and that each molecular wheel contains eight $^{19}$F nuclear sites. However it is worthwhile observing that the procedure of comparing the integrals of different peaks in order to determine the number of nuclei producing the signals is not completely reliable in the case of field sweep spectra. In fact the $T_2$ relaxation time affecting the value of the echo integral and the spectral intensity can change as the field is being swept.

Table 5.3: Fit parameters of equation 5.16 corresponding to the fitting red curve shown in figure 5.16.

| | $A$ | $w$ | $x_c$ |
|---|---|---|---|
| Teflon | 0,01065 | 0,00937 | 0,01677 |
| | 0,05178 | 0,13403 | -0,01 |
| | 0,02794 | 0,12151 | 0,1 |
| | 0,0127 | 0,18829 | 0,81 |

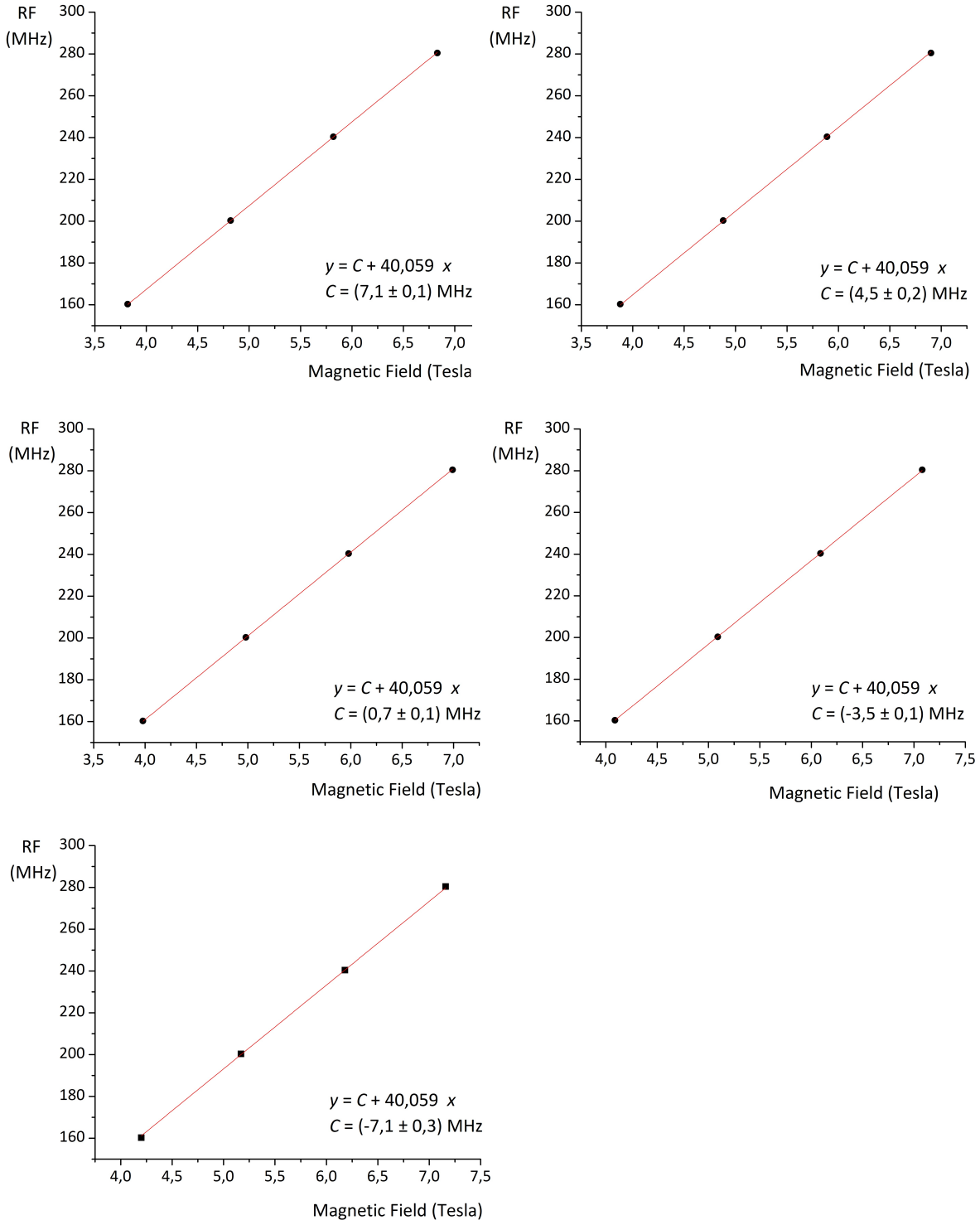


Figure 5.15: The radiofrequency versus applied field plots referring to the five slightly shifted peaks identified in the spectra in figure 5.13 The best fit lines according to the equation $y = C + 40,059 \cdot x$ are also shown.

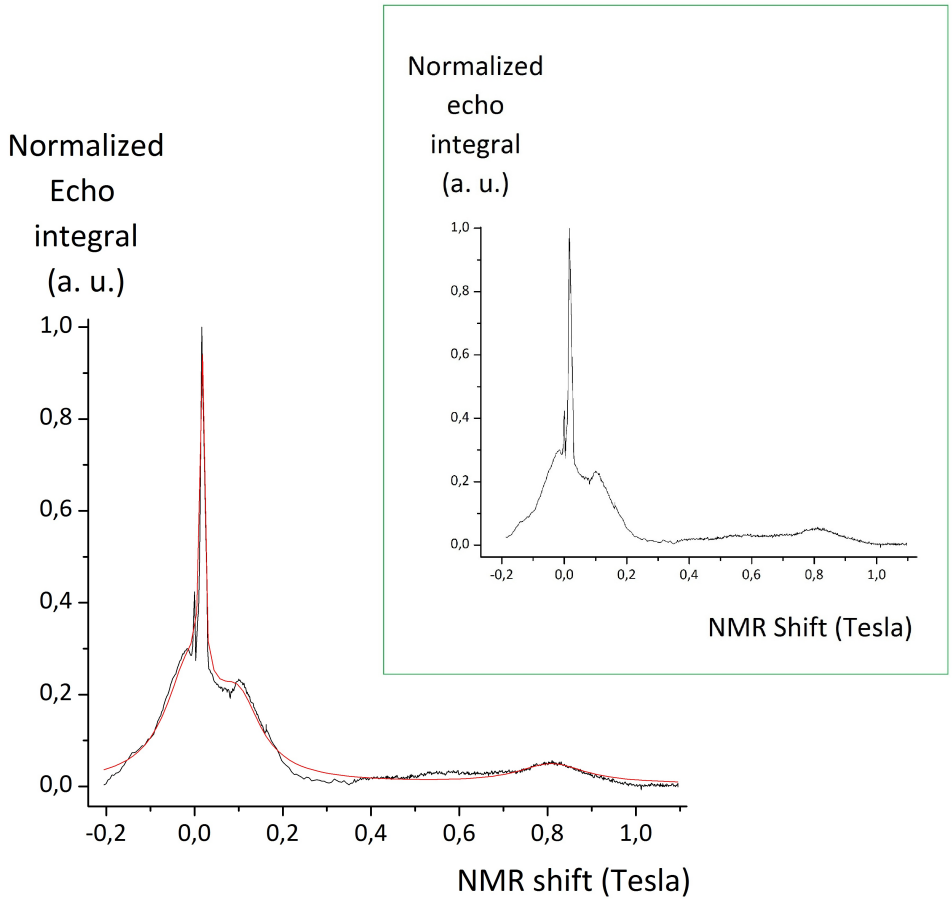


Figure 5.16: $^{19}$F-NMR spectrum of a $Cr_7Ni$ single crystal. The field sweep spectrum has been collected at $T$ = 1.6 K at the fixed Larmor frequency of 200,295 MHz corresponding to a 5 Tesla Larmor field. The magnetic field is applied parallel to the crystallographic $c$-axis namely perpendicular to the molecular ring. The red line is the result of the Lorentzian fit in equation 5.16.

# Chapter 6

# Discussion and conclusions

The purpose of the present section is to summarize and discuss the results of this thesis experimental work. Both $^{53}$Cr-NMR and $^{19}$F-NMR measurements have been performed in different antiferromagnetic molecular rings. While the first provide a straightforward information on the local electronic spin distribution thanks to the direct core polarization field affecting the $^{53}$Cr-NMR shift, the latter are more difficult to interpretate due to the transferred nature of the hyperfine fields at the $^{19}$F sites located approximatively half way between two magnetic ions.

The $^{53}$Cr-NMR spectrum has been measured at $T = 1,5$ K in $Cr_7Ni$ in the $S = 1/2$ ground state. Due to the poor S/N ratio only one signal has been observed: this signal has been assigned to three equivalent $^{53}$Cr nuclei in the ring namely site 2, 4 and 6. The $^{53}$Cr-NMR frequency dependence on the magnetic field is found to be in good agreement with the predictions obtained by assuming the staggered local spin density calculated theoretically and shown in figure 1.16 and a core polarization field $A_{\rm cp} = -10,96$ Tesla close to the value $A_{\rm cp} = -12,32$ Tesla found previously in $Cr_7Cd$ [21]. Attempts of detecting the $^{53}$Cr-NMR signals at temperatures as low as 0,1 K by means of a $^3$He - $^4$He dilution refrigerator didn't succeed due to the NMR probe low sensitivity.

$^{19}$F-NMR spectra have been collected in $Cr_8$ in the ground state yielding direct evidence of the molecular type singlet ground state i.e. the total spin value $S = 0$ is due to local spin expectation values $\langle s_i \rangle = 0$ resulting in a single non shifted NMR line. $^{19}$F-NMR spectra have been collected in $Cr_8$ at temperatures and fields at which the excited states are populated resulting in non zero NMR shifts. However the value of the $^{19}$F - $Cr^{3+}$ transferred hyperfine constant could not be determined if assumption is made that the local spin moment expectation values are given by the homogeneous spin distribution calculated theoretically and shown in figure 1.5.

The $^{19}$F-NMR spectra analysis in $Cr_7Cd$ and $Cr_7Ni$ has provided an estimate of the order of magnitude of the overall transferred hyperfine constants relating to the $F^-$ - $Cr^{3+}$ bond and to the $F^-$ - $Ni^{2+}$ bond. The results are reported in Table 6.1 together with the results obtained in the past concerning the $F^-$ - $Mn^{2+}$ transferred hyperfine constant in the antiferromagnetic compounds $KMnF_3$ and $MnF_2$ (the isotropic term is reported, see Appendix A). Somehow surprisingly we obtain a negative value for the $^{19}$F - $Cr^{3+}$ overall transferred hyperfine constant in $Cr_7Cd$ for the $^{19}$F nuclear sites close to the diamagnetic $Cd^{2+}$ ion. This can be explained by assuming a transferred core polarization negative term and/or a dominant negative contribution of the transferred anisotropic terms in equation 2.32.

Table 6.1: Hyperfine transferred field at the $^{19}F$ nucleus expressed in Tesla per Bohr magneton. The overall values including both the isotropic and the anisotropic contributions are reported for $Cr_7Cd$ and $Cr_7Ni$. The variation ranges are due to the different orientations of the sample ($^{19}F$ - $Cr^{3+}$ constant in $Cr_7Cd$ and $^{19}F$ - $Ni^{2+}$ constant in $Cr_7Ni$) or to determinations obtained by means of different peaks ($^{19}F$ - $Cr^{3+}$ constant in $Cr_7Ni$). The isotropic component is reported for $KMnF_3$ and $MnF_2$.

| | | | |
|---|---|---|---|
| $Cr_7Cd$ | $-0,33 \div -0,31$ Tesla | $^{19}F$ - $Cr^{3+}$ | Sites close to $Cd^{2+}$ |
| $Cr_7Ni$ | $+0,5 \div +0,96$ Tesla | $^{19}F$ - $Ni^{2+}$ | |
| $Cr_7Ni$ | $-1,18 \div +1,18$ Tesla | $^{19}F$ - $Cr^{3+}$ | |
| $KMnF_3$ | $+0,61 \pm 0,02$ Tesla | $^{19}F$ - $Mn^{2+}$ | Paramagnetic phase [16] |
| $MnF_2$ | $+0,59 \pm 0,01$ Tesla | $^{19}F$ - $Mn^{2+}$ | Paramagnetic phase [17] |

It is worthwhile observing that the $^{19}F$-NMR measurements in $Cr_8$, $Cr_7Cd$ and $Cr_7Ni$ show a large anisotropic contribution while the anisotropic term turned out to be neglible in the antiferromagnetic compounds $KMnF_3$ and $MnF_2$. However, as pointed out in the text, the separate determination of the $A_t$, $A_\sigma$ and $A_\pi$ contributions to the transferred hyperfine coupling requires the detailed study of the molecular orbitals involved in the $Cr^{3+}$ - $F^-$ coordinative bond. In particular one should be able to determine the values of the angles $\theta_\sigma$ and $\theta_\pi$ between the directional $p_\sigma$ and $p_\pi$ bonds and the applied magnetic field direction for each $^{19}F$ site. This goes beyond the purpose of the present work.

# Appendix A

# Direct and transferred hyperfine fields at the $^{19}$F nucleus

This appendix reports some information available in the literature concerning the hyperfine magnetic fields at the $^{19}$F nuclear site, both direct and transferred hyperfine fields, which are useful for the present work. Also, the theoretically calculated core polarization field in the Chromium atom is reported. The first section reports the theoretical values of the direct hyperfine field produced at the $^{19}$F nuclear site by an hypothetic single unpaired electron belonging to a given atomic orbital. These values can be used to determine the percentage of $2s$ and $2p$ unpaired electron in the $F^-$ ion when this is involved in a bonding once the experimental values of the isotropic and anisotropic transferred hyperfine contants introduced by equation 2.32 are known. Examples of this procedure are illustrated in the following sections of this appendix referring to the important studies about the antiferromagnetic compounds $KMnF_3$ and $MnF_2$ by R. G. Shulman, V. Jaccarino, K. Knox and P. Heller (references [16], [17] and[18]). These experimental determinations can be usefully compared to the results of the present work as shown in table 6.1.

## A.1 Theoretical values of the direct hyperfine constants in the Fluorine and in the Chromium atom

The direct hyperfine constant relating to a single unpaired $2p$ electron at the $^{19}$F nuclear site in the Fluorine atom can be calculated by means of equation 2.30 in section 2.5.3 reported here for convenience [1]:

$$A_{2p} = \frac{2}{5} g \mu_B \gamma_n \hbar \langle \frac{1}{\boldsymbol{r}^3} \rangle_{2p}.$$

We are not considering the presence of any electron other than a single $2p$ electron. The expression is obtained by averaging the nucleus-electron dipoar interaction over the $2p$ wavefunction. The angular dependence of the dipolar interaction is averaged over the $2p_x$, $2p_y$ and $2p_z$ components of the $2p$ wavefunction and thus yields a numerical factor independent of the orientation. In this hypothesis,

[1] This value is expressed in erg.

the theoretical calculation based on atomic wavefunctions yields [2,3]:

$$A_{2p}(\mathrm{F}) = 0,044\,\mathrm{cm}^{-1}. \tag{A.1}$$

The corresponding value of the magnetic field produced at the $^{19}$F nuclear site by a single unpaired $2p$ electron is [17]:

$$H_{2p}(\mathrm{F}) = c\frac{2\pi}{\gamma_\mathrm{n}} A_{2p}(\mathrm{cm}^{-1}) \cdot \frac{1}{2} \sim 16,5 \text{ Tesla}. \tag{A.2}$$

where $\frac{1}{2}$ is the unpaired electron spin [4].

The theoretical value of the direct contact hyperfine constant relating to a single unpaired $2s$ electron in the $^{19}$F atom is given by equation 2.31 in section 2.5.3:

$$A_{2s} = \frac{8}{3}\pi g \mu_\mathrm{B} \gamma_\mathrm{n} \hbar |\psi(0)|^2_{2s}$$

yielding for the atomic wavefunction $s$ [5]:

$$A_{2s}(\mathrm{F}) = 1,57\,\mathrm{cm}^{-1}. \tag{A.3}$$

The corresponding value of the direct contact hyperfine field produced by an unpaired $2s$ electron at the $^{19}$F nuclear site is [17] [6]:

$$H_{2s}(\mathrm{F}) = c\frac{2\pi}{\gamma_\mathrm{n}} A_{2s}(\mathrm{cm}^{-1}) \cdot \frac{1}{2} \sim 588 \text{ Tesla}. \tag{A.4}$$

In the Chromium atom the core polarization hyperfine field at the $^{53}$Cr nucleus due to a single unpaired $3d$ electron via the polarization of the $s$ electrons has been theoretically estimated to be [20]:

$$A_\mathrm{cp} = -12,5 \text{ Tesla/Bohr magneton} \tag{A.5}$$

as described in section 2.5.3.

## A.2 Transferred hyperfine interaction in $KMnF_3$

An interesting study of the effect of the hyperfine interactions on $^{19}$F-NMR spectra can be found in the work by R. G. Shulman and K. Knox in $KMnF_3$ [16]. $^{19}$F-NMR experiments have been performed on $KMnF_3$ single crystals. This compound has been chosen because of the high level of simmetry of its ideal perovskite structure. As shown in figure A.1 each $^{19}$F nucleus is collinear with two $Mn^{2+}$ magnetic ions whose electronic configuration is: $[Mn^{2+}] = [Ar]3d^5$, $s = \frac{5}{2}$. The $F^-$ - $Mn^{2+}$ bond distance is 2,09 Å. $^{19}$F resonance frequency is therefore affected by the hyperfine interaction between the $^{19}$F nuclear magnetic moment $\gamma\hbar\boldsymbol{I}$ and the $Mn^{2+}$ electronic magnetic moment $-\mu_B g\boldsymbol{S}$.

The nuclear Hamiltonian can be written [7]:

$$\mathcal{H} = -\gamma\hbar\boldsymbol{I}\cdot\boldsymbol{H} + \sum_j \boldsymbol{I}\cdot\boldsymbol{A}_j\cdot\boldsymbol{S}_j + \sum_j \gamma\hbar\boldsymbol{I}\cdot\mu_B g\boldsymbol{S}_j \frac{(3\cos^2\theta_j - 1)}{\boldsymbol{r}_j^3}. \tag{A.6}$$

[2] $A(\mathrm{cm}^{-1}) = \frac{A(\mathrm{erg})}{hc}$.

[3] The expectation value $\langle\frac{1}{\boldsymbol{r}^3}\rangle_{2p}$ has been calculated by Barnes and Smith [22].

[4] Reference [17] reports the value $H_{2p}(\mathrm{F}) = 18$ Tesla.

[5] The numerical value of $|\psi(0)|^2_{2s}$ has been evaluated by Hartree [23].

[6] Reference [17] reports the value $H_{2s}(\mathrm{F}) = 610$ Tesla.

[7] The value of the hyperfine coupling constant is expressed in erg in equation A.6: $A(\mathrm{cm}^{-1}) = \frac{A(\mathrm{erg})}{hc}$.

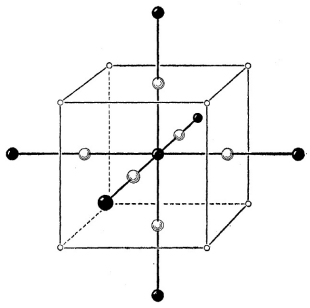

Figure A.1: $KMnF_3$ crystal structure. The white spheres represent $^{19}F$ atoms while the black spheres are the $Mn^{2+}$ magnetic ions [16]. Each fluoride ion is collinear with two $Mn^{2+}$ magnetic ions.

The first term on the right handside of this equation is the energy of the Zeeman interaction between the nuclear magnetic moment $\gamma\hbar\boldsymbol{I}$ and the applied magnetic field $\boldsymbol{H}$. The other terms on the right handside of equation A.6 describe the hyperfine interaction between $^{19}F$ and $Mn^{2+}$. The second term describes the transferred hyperfine interaction and it accounts for both the isotropic and the anisotropic contributions.

The third term is the classical expression of the dipolar interaction between a magnetic moment $\gamma\hbar\boldsymbol{I}$ and the $j$th electronic spin $\boldsymbol{S}_j$. $\boldsymbol{r}_j$ is the distance between these two magnetic moments and $\theta_j$ is the angle between $\boldsymbol{r}_j$ and the applied magnetic field $\boldsymbol{H}$. This interaction is inherently anisotropic. Assuming that the electronic spins are in the paramagnetic state [8], this term turns out to be proportional to the electronic static and homogeneous magnetic susceptibility and to the applied magnetic field.

A simplified expression for the transferred hyperfine interaction described by the second term in equation A.6 is obtained by taking advantage of the crystal symmetry and by considering only the nearest neighbors interactions. This hyperfine term is made up of an isotropic contribution, proportional to the transferred hyperfine constant $A_t$, and of an anisotropic contribution, proportional to $A_\sigma - A_\pi$ (see equation 2.32). The interactions described by $A_\sigma$ are due to unpaired spins in the $F^-$ electronic $p$ orbitals lying along the $Mn^{2+}$ - $F^-$ internuclear axis. An example of this is the superposition of the $Mn^{2+}$ $3d_{z^2}$ orbital and the $F^-$ $2p_z$ orbital. Viceversa, the $A_\pi$ interactions arise from unpaired spins in the $F^-$ electronic $p$ orbitals perpendicular to the internuclear axis. A $\pi$-type superposition is the one between the $Mn^{2+}$ $3d_{xz}$ orbital and the $F^-$ $2p_x$ orbital.

The value of the isotropic transferred hyperfine constant $A_t$ experimentally obtained in this work by R. G. Shulman and K. Knox is [16]:

$$A_t = (16,3 \pm 0,4) \cdot 10^{-4}\ \mathrm{cm}^{-1} \tag{A.7}$$

corresponding to $1,22 \pm 0,03$ Tesla [9]. The anisotropic term $A_\sigma - A_\pi$ is two orders of magnitude smaller.

It is worthwhile oberving that this value of the isotropic hyperfine constant $A_t$ does include the electronic $g$ factor and does *not* include the electronic spin value as shown by equation A.6. On the other hand, the hyperfine constant values determined in the experimental section of the present work do

[8] This holds above the antiferromagnetic ordering temperature, around 88 K.

[9] $A(\mathrm{Tesla}) = A(\mathrm{cm}^{-1})c\frac{2\pi}{\gamma_n}$.

*not* include both the electronic Landé $g$ factor and the spin expectation value (see for example equation 4.6 relating to the analysis of $Cr_7Cd$ $^{19}F$-NMR spetra). This fact must be carefully considered when a comparison between the values is made. The transferred hyperfine field at the $^{19}F$ nucleus per Bohr magneton is obtained by dividing value A.7 by the electronic Landé factor $g = 2$ yielding $0,61 \pm 0,02$ Tesla per Bohr magneton to be compared to the present work's experimental determinations as shown in table 6.1.

The percentage $f_s$ of unpaired spin in the $2s$ $F^-$ orbital in $KMnF_3$ can be derived by means of the following procedure [16]. The $0,61 \pm 0,02$ Tesla hyperfine field per Bohr magneton at the $^{19}F$ nucleus is multiplied by the factor $gS = 2\frac{5}{2}$ representing the electronic magnetic moment expressed in Bohr magnetons yielding the transferred field produced by a $Mn^{2+}$ ion at a $^{19}F$ nuclear site. The approximate value of this transferred hyperfine field is:

$$0,61 \pm 0,02 \text{ Tesla} \cdot 2 \cdot \frac{5}{2} = 3,0 \pm 0,1 \text{ Tesla}.$$

The percentage of $s$ covalent character of the $F^-$ - $Mn^{2+}$ bonding is obtained by dividing this value by the hyperfine field produced by a single unpaired $2s$ electron at the $^{19}F$ nuclear site A.4 yielding:

$$f_s = \frac{3,0 \pm 0,1 \text{ Tesla}}{588 \text{ Tesla}} = 0,52 \pm 0,02 \ \%. \tag{A.8}$$

## A.3 Transferred hyperfine field in $MnF_2$

In $MnF_2$ each $^{19}F$ atom binds three $Mn^{2+}$ ions: these bonds are only partially ionic. Two different types of $^{19}F$ - $Mn^{2+}$ bonds can be identified in $MnF_2$: they are labelled "type I" and "type II" according to the nomenclature in use [17]. These bonds have different lengths: 2,11 Å and 2,14 Å respectively. Also, there are two nonequivalent $^{19}F$ sites, labelled $F_\alpha$ and $F_\beta$ as shown in figure A.2.

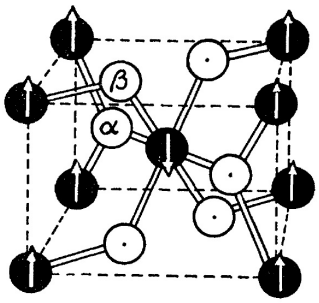


Figure A.2: $MnF_2$ crystal structure in the antiferromagnetic phase. The white spheres represent $F_\alpha$ and $F_\beta$ atoms while the black spheres are the $Mn^{2+}$ magnetic ions [18].

### A.3.1 Antiferromagnetic phase

A study of the transferred hyperfine field at the $^{19}F$ nuclear site in antiferromagnetic compounds is the one carried on by P. Heller [18] in the 1960's by means of $^{19}F$-NMR measurements performed on $MnF_2$ single crystals below the antiferromagnetic transition temperature $T_N = 67,4$ K [28].

The observed NMR frequency is given by:

$$\nu = \frac{\gamma}{2\pi}|\boldsymbol{H}_{\mathrm{Nucl}}| \tag{A.9}$$

where $\gamma$ is the $^{19}$F gyromagnetic ratio. $\boldsymbol{H}_{\mathrm{Nucl}}$ is the magnetic field at the nuclear site:

$$\boldsymbol{H}_{\mathrm{Nucl}\,,\,\alpha} = \boldsymbol{H}_0 + H_{\mathrm{Int}}(T)\hat{\boldsymbol{c}} + \boldsymbol{p}_\alpha(T)\cdot\boldsymbol{H}_0 \tag{A.10}$$

$$\boldsymbol{H}_{\mathrm{Nucl}\,,\,\beta} = \boldsymbol{H}_0 - H_{\mathrm{Int}}(T)\hat{\boldsymbol{c}} + \boldsymbol{p}_\beta(T)\cdot\boldsymbol{H}_0 \tag{A.11}$$

where $\boldsymbol{H}_0$ is a weak external field. $\pm H_{\mathrm{Int}}(T)\hat{\boldsymbol{c}}$ is the local field produced by the spontaneous electronic magnetization of the $Mn^{2+}$ ions sublattices. The third term on the right handside of equations A.10 and A.11 describes the change in the local field $\boldsymbol{H}_{\mathrm{Nucl}}$ due to the polarization of the $Mn^{2+}$ electronic spins in the applied field.

When the applied field is zero, the local field is directed along the $c$ axis:

$$\boldsymbol{H}_{\mathrm{Nucl}\,,\,\alpha} = +H_{\mathrm{Int}}(T)\hat{\boldsymbol{c}} \tag{A.12}$$

$$\boldsymbol{H}_{\mathrm{Nucl}\,,\,\beta} = -H_{\mathrm{Int}}(T)\hat{\boldsymbol{c}}. \tag{A.13}$$

The zero-field observed frequency follows from equation A.9:

$$\nu_0 = \frac{\gamma}{2\pi}H_{\mathrm{Int}}(T). \tag{A.14}$$

At $T = 0$ K the equation:

$$H_{\mathrm{Int}}(T=0) = (2A_z^I - A_z^{II})\,g\,\frac{5}{2} \tag{A.15}$$

holds due to the saturation of the sublattice magnetization. This is to say that at $T = 0$ K the $Mn^{2+}$ spin expectation values in a vanishing applied field are: $< S >_{Mn^{2+}} = \pm\frac{5}{2}$. In equation A.15 $g$ is the electronic Landé factor while $A_z^I$ and $A_z^{II}$ are the transferred hyperfine constants relating to type I and type II $^{19}$F - $Mn^{2+}$ bonds respectively. The hyperfine fields at the two sites $\alpha$ and $\beta$ (equations A.12 and A.13) differ only by the sign and thus yield the same resonance frequency A.14 for $\boldsymbol{H}_0 = \boldsymbol{0}$.

The value of the zero-field $^{19}$F resonance frequency at $T = 0$ K $\nu_{0,0}$ has been determined by fitting the experimental zero field resonance frequency $\nu_{0,T}$ [10] as a function of the temperature [28] according to:

$$\frac{\nu_{0,T}}{\nu_{0,0}} = A(T_{\mathrm{N}} - T)^R \tag{A.16}$$

yielding:

$$\nu_{0,0} = 159,978\ \mathrm{MHz} \quad \Longrightarrow \quad H_{\mathrm{Int}}(T=0) = \frac{\nu_{0,0}}{\frac{\gamma}{2\pi}} \sim 3,99\ \mathrm{Tesla}. \tag{A.17}$$

Assuming $g = 2$ we get:

$$2A_z^I - A_z^{II} = \frac{H_{\mathrm{Int}}(T=0)}{\frac{5}{2}\cdot 2} \sim 0,8\ \mathrm{Tesla}. \tag{A.18}$$

Assumption is made that $A_z^I \sim A_z^{II}$ yielding:

$$A_z \sim 0,8\ \mathrm{Tesla} \tag{A.19}$$

where $A_z$ is the average value of the transferred hyperfine field at the $^{19}$F nucleus per Bohr magneton and here is measured in Tesla instead of $\mathrm{cm}^{-1}$ as usual.

[10] $\nu_{0,T}$ has been collected only for the first 1,8 K below $T_{\mathrm{N}}$.

### A.3.2 Paramagnetic phase

$^{19}$F-NMR measurements in $MnF_2$ crystals in the paramagnetic phase have been performed by R. G. Shulman and V. Jaccarino [17] in 1957. $MnF_2$ can be described by the nuclear Hamiltonian 2.29 here rewritten for convenience:

$$\mathcal{H} = -\gamma_n \hbar \sum_{i}^{x,y,z} I_i H_i + \sum_{i}^{x,y,z} \sum_{j=1}^{3} A_i^j I_i \langle S_i \rangle^j \tag{A.20}$$

where the $j^{th}$ sum extends over the three nearest $Mn^{2+}$ neighbors of each $F^-$. The transferred hyperfine constant is expressed in erg and its components can be written according to the general equation 2.32. The transferred hyperfine constant isotropic component $A_t$ and the anisotropic components $A_\sigma$ and $A_\pi$ introduced in equation 2.32 have been determined by means of the observed $^{19}$F-NMR shifts. In particular the value:

$$A_t = (15,7 \pm 0,3) \cdot 10^{-4}\,\mathrm{cm}^{-1} \tag{A.21}$$

has been determined. The anisotropic terms turn out to be two orders of magnitude smaller. As shown by equation A.20 this value does include the electronic $g$ factor and does *not* include the magnetic ion spin value $\frac{5}{2}$. Thus the hyperfine constant per Bohr magneton is $A_t = (7,85 \pm 0,15) \cdot 10^{-4}\,\mathrm{cm}^{-1}$ corresponding to the hyperine field per Bohr magneton:

$$(7,85 \pm 0,15) \cdot 10^{-4}\,\mathrm{cm}^{-1} c \frac{2\pi}{\gamma_n} = 0,59 \pm 0,01 \text{ Tesla} \tag{A.22}$$

to be compared to the experimental results of the present work as shown in table 6.1.

The percentage $f_s$ of $s$ covalent character of the $F^-$ - $Mn^{2+}$ bonding in $MnF_2$ is given by [11]:

$$f_s = \frac{0,59 \pm 0,01 \text{ Tesla} \cdot 2 \cdot \frac{5}{2}}{588 \text{ Tesla}} = 0,502 \pm 0,008\ \%. \tag{A.23}$$

In equation A.23 the term $0,59 \pm 0,01$ Tesla $\cdot\, 2 \cdot \frac{5}{2}$ represents the hyperfine transferred field produced by a $Mn^{2+}$ 5/2 spin at the $^{19}$F nuclear site while the denominator is the hyperfine direct contact field at the $^{19}$F nucleus due to a single unpaired $2s$ electron given by equation A.4.

We notice that the isotropic contact transferred hyperfine field determined in the paramagnetic phase i. e. $H \sim 0,59 \pm 0,01$ Tesla (equation A.22) is different from the one determined in the low temperature antiferromagnetic phase i. e. $H \sim 0,8$ Tesla (equation A.19). The difference is likely due to the fact that in the study of the paramagnetic phase the different hperfine constants $A_t$, $A_\sigma$ and $A_\pi$ have been determined separately. Therefore the hyperfine field of $0,59 \pm 0,01$ Tesla corresponds to the isotropic transferred contact term only. In the antiferromagnetic phase we have estimated the internal field of $\sim 0,8$ Tesla at $T = 0$ which includes both isotropic transferred, anisotropic transferred and dipolar fields which can thus be higher than $A_t$ only. For this reason we use in Table 6.1 the value $A_t = (7,85 \pm 0,15) \cdot 10^{-4}\,\mathrm{cm}^{-1} = 0,59 \pm 0,01$ Tesla/Bohr magneton.

[11] The value reported in reference [17] is $f_s = 0,48 \pm 0,02\%$

# Appendix B

# Abstracts of JEMS 2012 international conference

### Redistribution of local spin density in $Cr_7Ni$ antiferromagnetic molecular ring from $^{53}Cr$ NMR

C. Casadei [1], E. Garlatti [2], L. Bordonali [1], Y. Furukawa [3], F. Borsa [1,3], A. Lascialfari [4], S. Carretta [5], G. Timco [6], R. Winpenny [6].

*(1) CNISM and Department of Physics A.Volta, Università degli Studi di Pavia, I-27100 Pavia, Italy.*
*(2) Department of Molecular Sciences Applied to Biosystems, Università degli Studi di Milano, I-20134 Milano.*
*(3) Department of Physics / Ames Laboratory, Iowa State University, 50011 Ames, Iowa (USA).*
*(4) Department of Molecular Sciences Applied to Biosystems, Università degli Studi di Milano, and INSTM, I-20134 Milano, Italy.*
*(5) Department of Physics, Università degli Studi di Parma, I-43124 Parma (Italy).*
*(6) The Lewis Magnetism Laboratory, The University of Manchester, M13 9PL Manchester, United Kingdom.*

Antiferromagnetic molecular rings are an ideal playground for investigating magnetism at nanoscale. The homometallic $Cr_8$ ring is formed by eight $Cr^{3+}$ moments ($s = 3/2$) which form at low temperature a total $S = 0$ ground state (GS) with zero expectation value of the local spins. When one $Cr^{3+}$ ion is replaced by a diamagnetic ion (e.g. $Cd^{2+}$) or a different magnetic ion (e.g. $Ni^{2+}$ with $s = 1$) the ground state becomes magnetic and there is a redistribution of the local spin density which can be calculated theoretically. In a previous work we measured the $^{53}$Cr-NMR in $Cr_7Cd$ and determined unambiguously the local spin density in the ring with excellent agreement with the theory (Phys. Rev. Letters 97, 267204 , 2006). In this work we tried to do the same for $Cr_7Ni$. Unfortunately, due to poor S/N ratio, only one $^{53}$Cr was detected down to 100 mK and the $^{61}$Ni signal is too weak. Nevertheless, by using the core polarization field $H_{cp} = -12.3$ Tesla found in $Cr_7Cd$ we could prove that the measured $^{53}$Cr-NMR signal corresponds to sites 2, 4, 6 with the local spin density calculated

| Ion site | $g\langle s\rangle$ | $\langle s\rangle$ |
|---|---|---|
| Cr 1 | 1.25315 | 0.633 |
| Cr 2 | -1.07189 | -0.541 |
| Cr 3 | 1.18954 | 0.601 |
| Cr 4 | -1.07047 | -0.541 |
| Cr 5 | 1.18954 | 0.601 |
| Cr 6 | -1.0719 | -0.541 |
| Cr 7 | 1.25315 | 0.633 |
| Ni | -0.79632 | -0.362 |

theoretically, as can be evinced from the table below. The table gives the calculated spin densities in the $Cr_7Ni$ ring in the GS at $T = 1,5$ K, with the applied field perpendicular to the ring plane. The sum of $\langle s\rangle$ is close to $S = 1/2$ as expected for the GS. The $^{53}$Cr-NMR signal measured at 1.6 K is in good agreement with: resonance frequency = Larmor frequency + $\gamma_{Cr}\ H_{cp} g\langle s\rangle$, with $\gamma_{Cr}$ = gyromagnetic ratio of $^{53}$Cr nucleus, $\langle s\rangle$ values for sites 2,4,6 (see table) and $H_{cp}$ = -12.3 Tesla.

## Magnetic properties and hyperfine interactions in $Cr_8$, $Cr_7Cd$ and $Cr_7Ni$ molecular rings from $^{19}$F-NMR

C. Casadei [1], E. Garlatti [2], L. Bordonali [1], Y. Furukawa [3], F. Borsa [1,3], A. Lascialfari [4], G. Timco [5], R. Winpenny [5].

*(1) CNISM and Department of Physics A. Volta, Università degli Studi di Pavia, I-27100 Pavia, Italy.*
*(2) Department of Molecular Sciences Applied to Biosystems, Università degli Studi di Milano, I-20134 Milano.*
*(3) Department of Physics / Ames Laboratory, Iowa State University, 50011 Ames, Iowa (USA).*
*(4) Department of Molecular Sciences Applied to Biosystems, Università degli Studi di Milano, and INSTM, I-20134 Milano, Italy.*
*(5) The Lewis Magnetism Laboratory, The University of Manchester, M13 9PL Manchester, United Kingdom.*

We present a detailed investigation of the static magnetic properties of molecular homometallic $Cr_8$ antiferromagnetic (AFM) ring and heterometallic $Cr_7Cd$ and $Cr_7Ni$ rings in the low temperature ground state, by $^{19}$F-NMR. The original idea was to utilize the $^{19}$F nucleus as a local probe for the electronic spin densities of the nearby $Cr^{2+}$ and $Ni^{2+}$ spins. However, the fact that the F atom is located midway between two magnetic ions gives rise to $^{19}$F-NMR spectra which have a complicated field dependent structure, due to both isotropic transferred hyperfine contact interactions and anisotropic dipolar and pseudo-dipolar interactions. Therefore the NMR spectra have to be analyzed in connection with the theoretical results concerning the local spin distribution in order to establish the values of the hyperfine interaction constants, not known at present. In $Cr_8$ the ground state is a

singlet with total spin $S = 0$. The $^{19}$F-NMR spectra at 1.6 K and at fields lower than 2 Tesla show a single narrow line, proving that the local spin density in the ground state is zero as expected for a molecular singlet state. When the magnetic field is not negligible with respect to the level crossing field $H_c \sim 7$ Tesla, a structure appears in the $^{19}$F-NMR spectrum which is orientation dependent (in a single crystal), indicating a dominant anisotropic contribution to the hyperfine fields. In $Cr_7Cd$ we could detect in the $^{19}$F-NMR spectrum a shifted line attributed to the F nuclei next to a Cr ion close to the Cd, thus allowing the unambiguous determination of the transferred hyperfine constant F - Cr. A similar analysis was possible on the $^{19}$F-NMR spectra in $Cr_7Ni$. The values of the isotropic hyperfine constants ($A \sim 1$ Tesla) are comparable to the ones known for F - Mn in AFM $KMnF_3$ and $MnF_2$.

# *Acknowledgments*

Thanks are due to Prof. F. Borsa, Dr. Y. Furukawa, Prof. A. Lascialfari, Prof. S. Carretta , E. Garlatti and Prof. G. Timco.

I would like to thank Lollo and my laboratory colleagues Steve and Beas, together with my friends in Ames in particular Eli and Katie.

Un grazie sentito va alla mia famiglia ed a Ste ed a tutti i miei amici in Italia in particolare Dani ed Ange, Fra, Luci, Lalla ed Aldo.

# Bibliography


[1] J. Van Slageren, R. Sessoli, D. Gatteschi, A. A. Smith, M. Helliwell, R. E. P. Winpenny, A. Cornia, A. Barra, A. G. M. Jansen, E. Rentscheler and G. A. Timco, *Chem.-Eur. J.* **8**, No. 1 (2002).

[2] F. K. Larsen, E. J. L. McInnes, H. E. Mkami, J. Overgaard, S. Piligkos, G. Rajaraman, E. Rentscheler, A. A. Smith, G. M. Smith, V. Boote, M. Jennings, G. A. Timco and R. E. P. Winpenny, *Angew. Chem. Int. Ed.* **42**, No. 1 (2003).

[3] M. Affronte, T. Guidi, R. Caciuffo, S. Carretta, G. Amoretti, J. Hinderer, I. Sheikin, A. G. M. Jansen, A. A. Smith, R. E. P. Winpenny, J. Van Slageren and D. Gatteschi, *PRB* **68**, 104403 (2003).

[4] E. Garlatti, private communication.

[5] S. Carretta, J. Van Slageren, T. Guidi, E. Liviotti, C. Mondelli, D. Rovai, A. Cornia, A. L. Dearden, F. Carsughi, M. Affronte, C. D. Frost, R. E. P. Winpenny, D. Gatteschi, G. Amoretti and R. Caciuffo, *PRB* **67**, 094405 (2003).

[6] Y. Furukawa, K. Kiuchi, K. Kumagai, Y. Ajiro, Y. Narumi, M. Iwaki, K. Kindo, A. Bianchi, S. Carretta, G. A. Timco and R. E. P. Winpenny, *PRB* **78**, 092402 (2008).

[7] E. Micotti, Y. Furukawa, K. Kumagai, S. Carretta, A. Lascialfari, F. Borsa, G. A. Timco and R. E. P. Winpenny, *PRL* **97**, 267204 (2006).

[8] S. Carretta *et al.*, *Phys. Rev. B* **67**, 094405 (2003).

[9] E. Liviotti, S. Carretta and G. Amoretti, *J. Chem. Phys.* **117**, 3361 (2002).

[10] T. C. Farrar, E. D. Becker in *Pulse and Fourier Transform NMR: Introduction to Theory and Methods* (Academic Press, 1971).

[11] C. P. Slichter in *Principles of Magnetic Resonance* (Springer-Verlag). Third enlarged and updated edition.

[12] A. Abragam in *Principles of Nuclear Magnetism* (Oxford University Press, New York, 1961).

[13] E. Fukushima, S. B. W. Roeder in *Experimental Pulse NMR: A Nuts and Bolts Approach* (Oxford University Press, 2006).

[14] D. Gatteschi, R. Sessoli, J. Villain in *Molecular Nanomagnets* (Oxford University Press, 2006).

[15] P. Carretta, A. Lascialfari in *NMR-MRI, μSR and Mössbauer Spectroscopies in Molecular Magnets* (Springer-Verlag Italia, 2007).

[16] R. G. Shulman and K. Knox, *Phys. Rev.* **119**, 1 (1960).

[17] R. G. Shulman and V. Jaccarino, *Phys. Rev.* **108**, 1219 (1956); **107**, 1196 (1957).

[18] P. Heller, *Phys. Rev.* **146**, 2 (1966).

[19] A. J. Freeman and R. E. Watson in *Hyperfine Interactions in Magnetic Materials, Magnetism IIA,* edited by G. T. Rado and S. Suhl (Academic, New York, 1967)

[20] G. C. Carter, L. H. Bennet and D. J. Kahan, *Metallic Shifts in NMR,* Progress in Material Science Vol. 20 (Pergamon, New York, 1977)

[21] E. Micotti, Y. Furukawa, K. Kumagai, S. Carretta, A. Lascialfari, F. Borsa, G. A. Timco and R. E. P. Winpenny, *PRL* **97**, 267204 (2006).

[22] R. G. Barnes and W. V. Smith, *Phys. Rev.* **93**, 95 (1954).

[23] D. R. Hartree, *Proc. Roy. Soc.* (London) **151**, 96 (1935).

[24] M. Tinkham, *Proc. Roy. Soc.* (London) **A236**, 535, 549 (1956).

[25] E. Fermi, *Z. Phys.* 60 (1930), 320

[26] H. Amiri, A. Lascialfari, Y. Furukawa, F. Borsa, G. A. Timco and R. E. P. Winpenny, *Phys. Rev. B* **82**, 144421 (2010).

[27] *Kelvinox Dilution Refrigerator and Supercondiucting Magnet System Operator's Handbook.* Oxford Instruments Nanoscience Limited (2006)

[28] P. Heller and G. B. Benedek, *PRL* **8**, 11 (1962).

[29] C. M. Casadei *et al.* unpublished.